APPLICATION OF WAVEFORM

TOMOGRAPHY AT CAMPOS

BASIN FIELD, BRAZIL

by

Mauricio Pedrassi

A thesis submitted to the Faculty and the Board of Trustees of the Colorado School of Mines in partial fulfillment of the requirements for the degree of Master of Science (Geophysics).

Golden, Colorado

Date _____

Signed: _____
Mauricio Pedrassi

Signed: _____
Dr. Thomas L. Davis
Thesis Advisor

Golden, Colorado

Date _____

Signed: _____
Dr. Terence K. Young
Professor and Head
Department of Geophysics

ABSTRACT

Campos Basin field has been continuously characterized inside the Reservoir Character-ization Project (RCP). Past research includes poststack and prestack joint inversions of PP and PS data which increased the reservoir resolution and could predict a porosity map. To further improve characterization of the Campos Basin field, waveform tomography (WT), or full waveform inversion (FWI), is performed for a 2D line from the 2010 ocean bottom cable (OBC) data under a 2D acoustic isotropic medium assumption. The goal is to bring high resolution and accuracy to the P wave velocity model for better quality reservoir imaging.

In order to achieve the best results the application of WT to the 2D dataset required defining the suitable parameters to these data, where the main options in the inversion are the type of objective function, the time domain damping, and the frequency discretization. The waveform inversion has improved the final velocity model, as verified by migrated images showing more continuous and focused horizons at the reservoir depth. The improved seismic image and velocity model are possible inputs, respectively, to a new geological interpretation and to acoustic/elastic attributes inversion.

However, only the background velocity was updated and the inversion failed in enhancing the resolution of the final velocity model. Waveform inversion was also performed on syn-thetic dataset with larger offsets generated for a reliable velocity model of the Campos Basin field. The combination of a larger offset with a waveform inversion strategy that includes amplitude and phase residuals in the objective function proved to be efficient in increasing the resolution of the final velocity model. Synthetic modeling suggests that if a new seismic acquisition program is conducted over the field, it would be highly beneficial for velocity analysis and reservoir characterization to acquire longer offsets.

TABLE OF CONTENTS

LIST OF FIGURES

LIST OF TABLES

ACKNOWLEDGMENTS

A special recognition to my wife, Renata, that has been part of my entire life, for his encouragement, love, patience and support.

Finally, thank you to all my family and friends that were rooting for me throughout these years.

To my family, friends and my wife Renata.

CHAPTER 1

INTRODUCTION

Waveform tomography (WT), or Full Waveform Inversion (FWI), has been the subject of studies and conceptual development over the past 30 years (Virieux and Operto, 2009). Furthermore, research groups and the oil industry around the world have shown the improvement that WT can bring to the velocity model, especially in terms of high resolution in comparison with conventional techniques, such as traveltime tomography (TT) or migration velocity analysis (MVA). These techniques can only build a smoothed version of the velocity model, containing the kinematics of the wavefield, even though they are able to generate a good quality seismic image. WT usually can restore the missing resolution of traveltime tomography. In this sense, WT represents a more advanced approach, that attempts to completely describe the complex interaction of the propagating waves and the earth, in which the phase of the whole waveform is used in the model reconstruction (Pratt, 2013).

Although WT is not a completely developed technique yet, and has several challenges to overcome, such as the computational limits imposed by 3D-elastic modeling and the estimation of anisotropy parameters among others, WT inversions performed under a feasible 2D acoustic isotropic medium assumptions can provide reasonable, high resolution, final velocity models (Sirgue and Pratt, 2004).

Improvements in the final result are highly dependent on a sufficiently accurate initial model, the minimum frequency of the data, the acquisition design (maximum offset) of the survey, and the source signature used to generate the synthetic data. All of these factors contribute to the WT convergence, potentially leading to the correct velocity model. The initial velocity model is usually obtained from TT or from MVA, which contains the background velocity information and can locate the objective function close to the global minimum. Reflection seismic data may not have low enough frequency content and large enough offsets to

provide good parameters for waveform inversion success. The source signature is extracted from data and its accuracy is closely related to the final results, because it is used to generate the synthetic data, which are compared with the observed data.

The Campos Basin field has been part of Reservoir Characterization Project (RCP) research for four years. The field is a deepwater turbidite sandstone, and the data for the project are provided by Petrobras. Past research includes work by Ribeiro (2011), performing PP and PS poststack joint inversion to increase the resolution of the reservoir, enabling delineation of the upper and lower units of the reservoir. Martins (2013) performed PP and PS prestack inversion to predict the porosity volume, thereby obtaining better reservoir characterization by integrating the elastic impedance, shear impedance and porosity. To further improve characterization of the Campos Basin field, the objective of the project now is to apply waveform tomography (waveform inversion) of the seismic data in order to obtain a higher resolution and more accurate P-wave velocity model of the area, focusing at the reservoir depth. The waveform inversion is performed using a 2D acoustic isotropic medium assumption. By improving the velocity model of the area, the updated seismic images will provide new geological interpretation as well as new attribute maps. Likewise, the updated velocity model may be incorporated in acoustic/elastic attribute inversions to better constrain the results.

Waveform Tomography will be performed in the frequency domain (Pratt and Worthington, 1990) using software provided by Prof. Gerhard Pratt (Pratt, 2013). The WT applied in the frequency domain has proven to be efficient, and the advantages will be described further in the document. This thesis will focus first on the waveform inversion of the OBC Campos Basin field, defining the best parametrization and strategy in order to obtain an improved version of the velocity model of the area. Secondly, a crucial parameter of WT, the maximum offset, has significant importance in the inversion results. The maximum offset evaluation is intended to provide the optimum maximum offset for a new survey in the Campos Basin field that would be able to properly measure the diving waves that reach and

travel through the reservoir. First to establish the low wavenumbers (large wavelengths) of the velocity model, and later to recover the high wavenumbers. This study is based on acoustic synthetic data generated with a new 2D design.

1.1 Campos Basin Field

The Campos Basin is the most prolific petroleum basin of Brazil and is responsible for approximately 70% of Brazil's daily oil production. The Campos Basin is located in southeastern Brazil, close to Rio de Janeiro and Espirito Santo States coast and it covers approximately an area of 115.000 km^2 (Figure 1.1). The basin currently has of fifty-eight oil fields, which are found between 50 km and 140 km off the Brazilian coast, occurring in water depths up to 2400 m. These fields produce oil from a variety of reservoirs, but they are mostly siliciclastic turbidites. These turbidites deposits are formed by turbidity currents, which are density currents composed of relatively dilute sediment-water mixtures (Martins, 2013).

Different types of turbidites reservoir can be found in Campos Basin distinguished by properties such as depositional processes, external geometry or grain size. Each reservoir can assume distinct sand-body geometries as individual lobes or channel sandstone bodies. The field of interest is subdivided into an upper zone with great lateral distribution, and a lower zone which is thicker, but more restricted in area (Ribeiro, 2011) (Figure 1.2). Figure 1.3 shows a seismic migrated image with interpreted horizons, from which we can see stratigraphic levels and the main structural features of the reservoir area.

This reservoir was discovered in 1984 and one year later, 1985, the field started the oil production. In order to improve recovery water injection was initiated in 2002. The water depth ranges from 320 m to 780 m. Petrophysical properties are excellent with an average porosity of 27% and average permeability of 2500 mD, and the oil is 29° API at reservoir conditions. Also, the reservoir has good lateral connection, although it is cut by several normal faults.
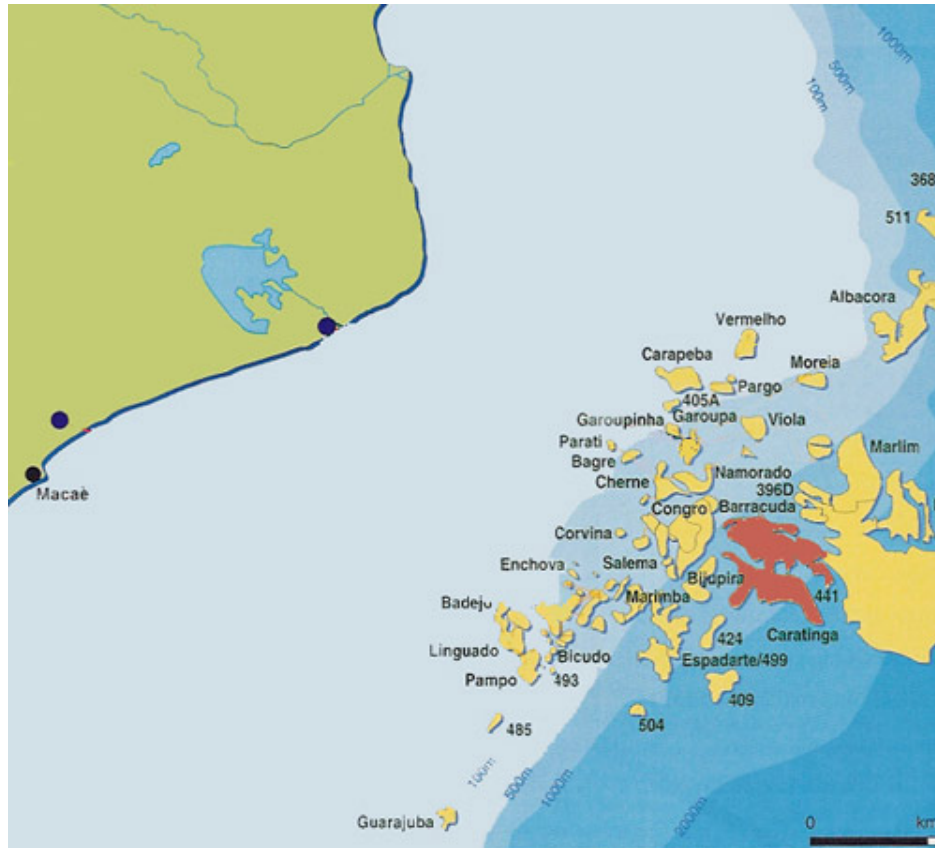
Figure 1.1: Campos Basin location showing several oil fields of the area.
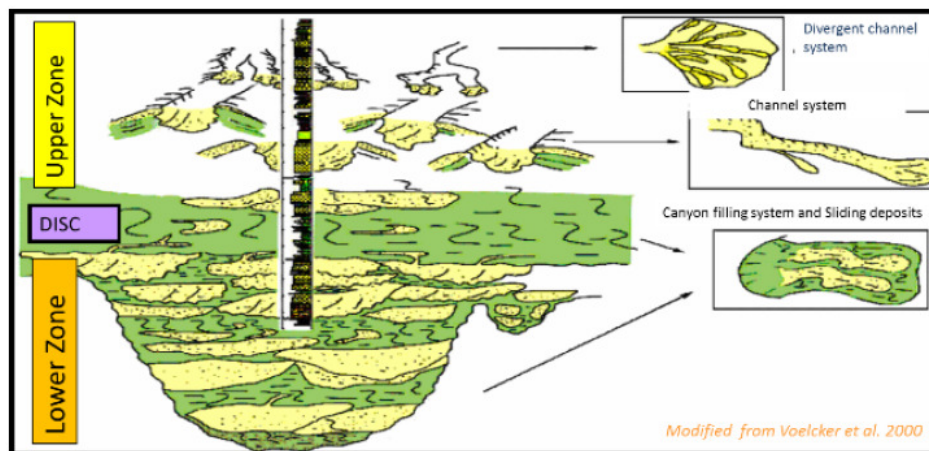
Figure 1.2: Architectural types of the field reservoir. (1) Canyon-filling deposits (massive thick sandstones and deformed shales); (2) Slip deposits (sandstones and deformed shales); (3) Channel system deposits (medium sandstones and deformed shales); (4) Divergent channel deposits (fine to medium massive sandstones with plane-parallel stratification at the top); modified from Martins (2013).

4

A detailed description of the Campos Basin geology can be found in both Martins (2013) and Ribeiro (2011).
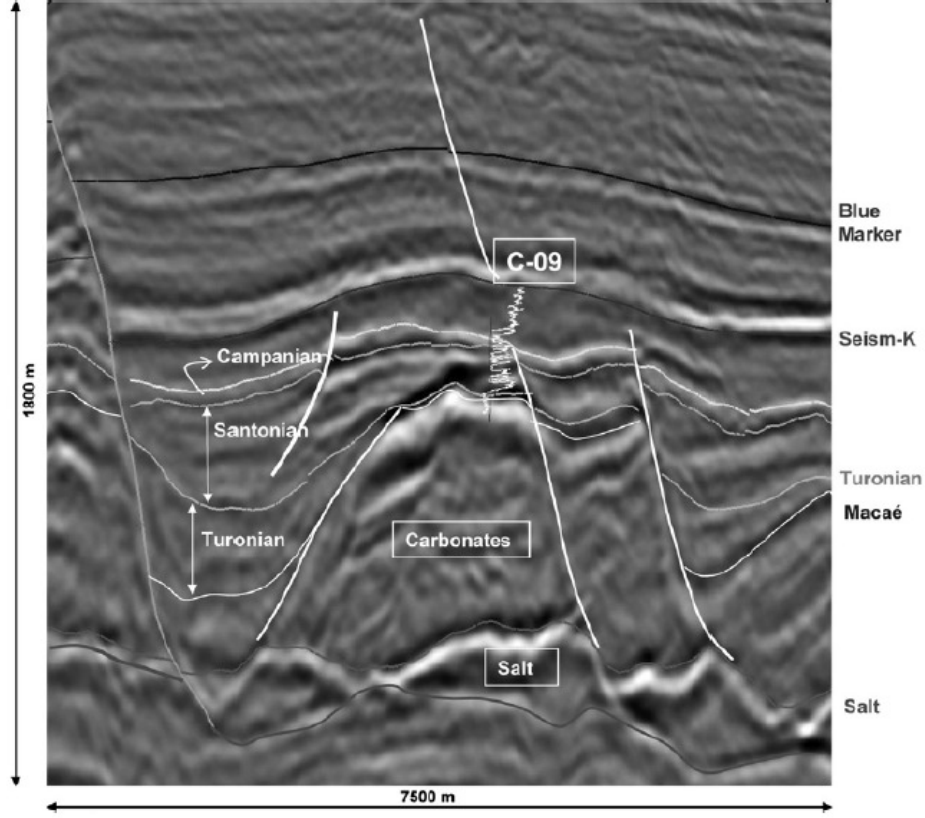
Figure 1.3: Seismic migrated line with interpretation, showing stratigraphic levels and main structural features of the reservoir area.

1.2   Waveform Tomography

Waveform tomography is a type of data matching method which attempts to recover the model parameters that best explain the observed data. In trying to fit the modeled data with the observed data, waveform inversion depends on how accurate the physics of wave propagation inside the earth is simulated. In this project, earth is assumed to be acoustic and isotropic which intrinsically defines the properties that describe the medium: P-wave velocity and density. However, the true nature of the earth is more complex which

includes elasticity and anisotropy among other properties. By ignoring theses complexities which would introduce real dynamic and kinematic effects on the wavefield the acoustic approximation itself is a source of error in the inversion, because it is an inappropriate representation of the physics of the earth. In this sense, waveform inversion assumes that the difference between the modeled and observed data, which is used to improve the model parameters, is attributed to errors in the model parameters (Alkhalifah, 2014). Even though the acoustic isotropic approximation is the simplest earth representation, waveform inversion can still build a more accurate and higher resolution velocity model.

The lack of very low frequency data and poor illumination due to acquisition design are crucial parameters that could influence the waveform inversion success. The source signature, which interacts with the near earth surface, has to be accurately extracted from seismic data in order to be used to generate the modeled data. Poor illumination (maximum offset) is a subject of the thesis.

Following is the mathematical description of the waveform tomography theory in the frequency domain (Pratt, 2013).

1.2.1   Waveform Tomography Theory

Any type of inverse problem is composed by three fundamental parts: the data, the model and some physical relation between them (Aster et al. (2013) and Tarantola (2005)). Figure 1.4 schematically shows the concept of the forward and inverse problem. The forward problem is straightforward where some physical relation is applied to a model parameter in order to obtain measurable quantities. The inverse problem is much more challenging; the reverse action is more difficult since in most cases the inverse operator (g^{-1}) does not exist or cannot be computed.

In seismic, the physical relation which connects the model parameters and the data is given by the wave equation, which in this project is the 2D acoustic isotropic wave equation in the frequency domain (Equation 1.1). The data are the known quantity, the recorded data acquired in the earth's surface, which in this project is from an ocean bottom cable (OBC)

6

seismic survey. The model parameters are the unknown quantities, the ones that inversion processes try to determine. As mentioned before, under the acoustic assumption we are inverting for P-wave velocity and the density is computed based on the Gardner's relation. All the math development is done in the frequency domain and follows Pratt (1999).

$$\nabla^2 u(\mathbf{x}, \omega) + \frac{\omega^2}{c^2(\mathbf{x})} u(\mathbf{x}, \omega) = 0 \tag{1.1}$$

Forward problem

$$g(\mathbf{m}) = \mathbf{d}$$

$$\mathbf{m} = g^{-1}(\mathbf{d})$$
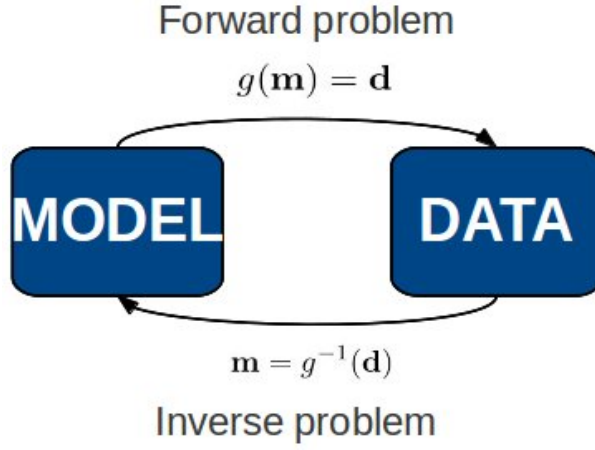
Inverse problem

Figure 1.4: Forward and inverse problem.

Waveform inversion is a highly non linear inverse problem and solved using a linearized least squares inversion by minimizing the objective function ($E(\mathbf{m})$, Equation 1.2), usually called the misfit function. The misfit function is based on the difference between the modeled data (u_i) and observed data (d_i), $\delta d_i = u_i - d_i$. Both observed and modeled data, are complex quantities, with real and imaginary parts, discretized at the receiver locations ($i = 1, 2, ..., n$) according to the acquisition design and they are expressed as vectors $\mathbf{d}$ and $\mathbf{u}$ shown in Equation 1.3. The nonlinearity of the objective function is caused basically by the sinusoidal nature of seismic wavefields and by the complex reflectivity of the Earth.

$$E(\mathbf{m}) = \frac{1}{2} \delta \mathbf{d}^T \delta \mathbf{d} = \frac{1}{2} \sum_{i=1}^{n} \delta d_i^* d_i \tag{1.2}$$

$$\mathbf{d} = \begin{pmatrix} d_1 \\ d_2 \\ . \\ . \\ . \\ d_n \end{pmatrix} \qquad \mathbf{u} = \begin{pmatrix} u_1 \\ u_2 \\ . \\ . \\ . \\ u_n \end{pmatrix} \qquad \mathbf{m} = \begin{pmatrix} m_1 \\ m_2 \\ . \\ . \\ . \\ m_m \end{pmatrix} \qquad (1.3)$$

Waveform inversion searches for the model parameters $\mathbf{m}$ (Equation 1.3) that minimize the real-valued objective function. Instead of a global minimum search, because of the high computation cost of seismic forward modeling, waveform inversion solution is obtained by gradient or local methods. The idea is to follow the opposite direction of the gradient of the function which indicates the steepest descent direction. Using this type of solution an initial velocity model is required and should be accurate enough to generate modeled data within a half cycle of the observed data, which restricts the search to the basin of attraction, close to the global minimum.

$$E(\mathbf{m} + \delta\mathbf{m}) = E(\mathbf{m}) + \delta\mathbf{m}^t \, \nabla_m E(\mathbf{m}) + \frac{1}{2}\delta\mathbf{m}^t \, \mathbf{H} \, \delta\mathbf{m} + O(\|\delta\mathbf{m}\|^3) \qquad (1.4)$$

$$\mathbf{H} \, \delta\mathbf{m} = -\nabla_m E \qquad (1.5)$$

In order to achieve the final solution, the misfit objective function is expanded in a Taylor series up to the quadratic term (Equation 1.4), then the first derivative with respect to each of the model perturbations in $\delta\mathbf{m}$ is computed and finaly set to zero. The complete solution is known as the Newton method and it is given by Equation 1.5, where $\delta\mathbf{m}$ is the model perturbation we are looking for.

Equation 1.5 shows the two terms that form the final solution, the gradient (∇_m) and the Hessian ($\mathbf{H}$) (Equation 1.6). The gradient points to the steepest descent direction of the objective function. The Hessian is the second derivative with respect to each model parameter. The Hessian matrix ($\mathbf{H}$) is very large, with one row and one column for every model parameter, which makes its computation unreasonable depending on the size of the model

parameters, usually large in seismic problems. Also, the Hessian matrix can be singular and cannot be inverted (Pratt, 2013). In order to overcome these disadvantages, a simpler solution, the steepest descent method is obtained by making the Hessian matrix equal to the identity matrix. In the complete solution, the Hessian matrix is a type of filter that modifies the gradient direction to improve convergence properties (Alkhalifah, 2014). In practice the Hessian matrix is ignored, although different types of pre-conditioning are applied to the gradient as an approximation to the Hessian, such as wavenumber filtering that smooths the gradient direction, avoiding the high wavenumber components (Sirgue, 2003).

$$\nabla_m E = \begin{pmatrix} \frac{\partial E}{\partial m_1} \\ \frac{\partial E}{\partial m_2} \\ . \\ . \\ \frac{\partial E}{\partial m_m} \end{pmatrix} \quad , \qquad H_{ij} = \frac{\partial^2 E}{\partial m_i \partial m_j} \quad . \tag{1.6}$$

Equation 1.7 shows that the solution is obtained by iteratively updating the velocity model. Instead of using a line search algorithm which would include several forward modeling steps, the step length α is determined by using the estimate for linear forward problems (Pratt, 2013) given by the Equation 1.8. However, the most important is the gradient computation. The gradient is not calculated explicitly, which would be unachievable for waveform inversion purpose. As shown by Lailly (1983) and Tarantola (1984), the gradient is mathematically equivalent to a Reverse Time Migration (RTM) (Alkhalifah, 2014). It is computed by the multiplication of the original forward propagated wavefield and the backpropagated wavefield with the sources replaced by the data residuals. The final model updating computation, including the step length modeling, takes three forward modeling runs per non-linear iteration.

$$\mathbf{m}^{(k)} = \mathbf{m}^{(k-1)} - \delta\mathbf{m}^{(k-1)}, \qquad \delta\mathbf{m}^{(k-1)} = -\alpha^{(k-1)}\nabla E^{(k-1)} \tag{1.7}$$

$$\alpha = \frac{|\nabla E_m|^2}{|\mathbf{J}\nabla_m E|^2}, \qquad J_{ij} = \frac{\partial u_i}{\partial m_j} \tag{1.8}$$

Therefore, the main objective of the WT is to build a high resolution and more accurate velocity model, which may bring new information to the reservoir characterization process. WT is still challenging and unfriendly with real data as indicated by Ratcliffe et al. (2011) and Alkhalifah (2014) because of the lack of very low frequency content and poor illumination.

CHAPTER 2

CAMPOS BASIN FIELD INVERSIONS: PARAMETRIZATION AND RESULTS

Waveform inversion is a technique which requires interaction between user and data. Several tests were performed in order to understand and optimize the main parameters of the process. Definition of the objective function, time damping parameter (data selection) and the frequency discretization are the main parameters. All of them are discussed in this chapter, which also includes description of the data. Moreover, discussion and analysis of the final results throughout quality control, such as migrated images and common image gathers (CIGs), helped understand the improvements and the failure of the inversion in the real data environment. The update in the background velocity produced better seismic images, although the promise of a high resolution velocity model was not achieved. Possible explanations are discussed.

2.1 Ocean Bottom Cable (OBC) Seismic Data

Waveform inversion is performed for a 2D line extracted from a 3-D, 4-C ocean-bottom-cable survey (OBC), which was conducted in 2010 with the purpose of doing 4D analysis in the reservoir area, using the 2005 OBC survey as baseline. Here, the waveform inversion is performed using only the pressure component of the data. Figure 2.1 schematically shows the OBC type of survey, where several vessels were used for shooting, recording and pulling the cables, to cover the area of interest. As can be seen, the cables lay on the sea floor while the shooting and recording vessels acquire the seismic data. Figure 2.2 shows the porosity map (Martins, 2013) with the main reservoir body delineated and the relative position of the 2D line used for the waveform inversion. The 2D seismic line used in this study crosses the main reservoir area which could allow the waveform inversion to update the velocity model of the reservoir.
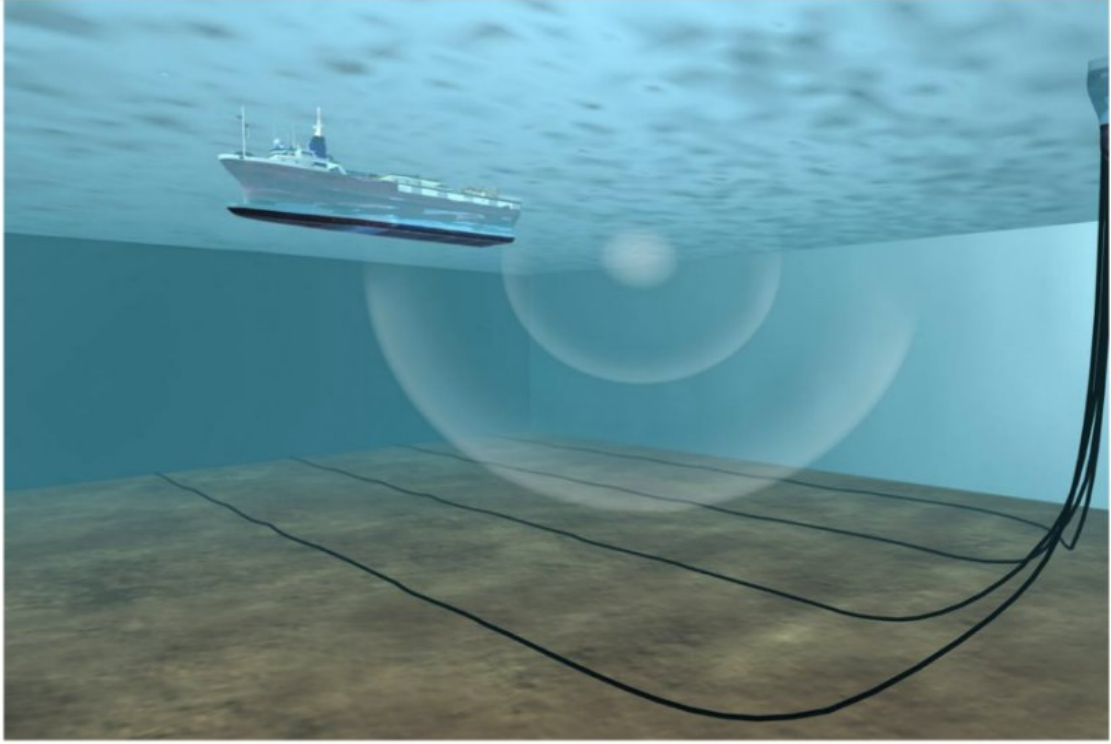
Figure 2.1: Acquisition vessel and ocean bottom cables (PGS Geophysical Acquisition Report, 2005).

The 2D dataset used in the inversion is the acquired field data without any type of pre-processing and delivered by Petrobras. Although, the input data can be noise filtered waveform inversion does not require pre-processed seismic data, which is an advantage to the entire process in terms of time. Noise is always a problem in the inversion process, because it is consider data and the inversion will try to find model parameters that also fits the noise. In this sense, it is useful to apply some filter process, at least to remove random noise from the field data. Physical events that cannot be simulated by the forward modeling are considered noise too, for example, PS converted waves in the acoustic assumption, these ones are removed by the time domain damping selection.

In order to perform the waveform inversion for the entire line, the three separated files were integrated. However, it was impossible to conduct the inversion because the inversion code cannot handle different geometries of the integrated line, where each individual line has
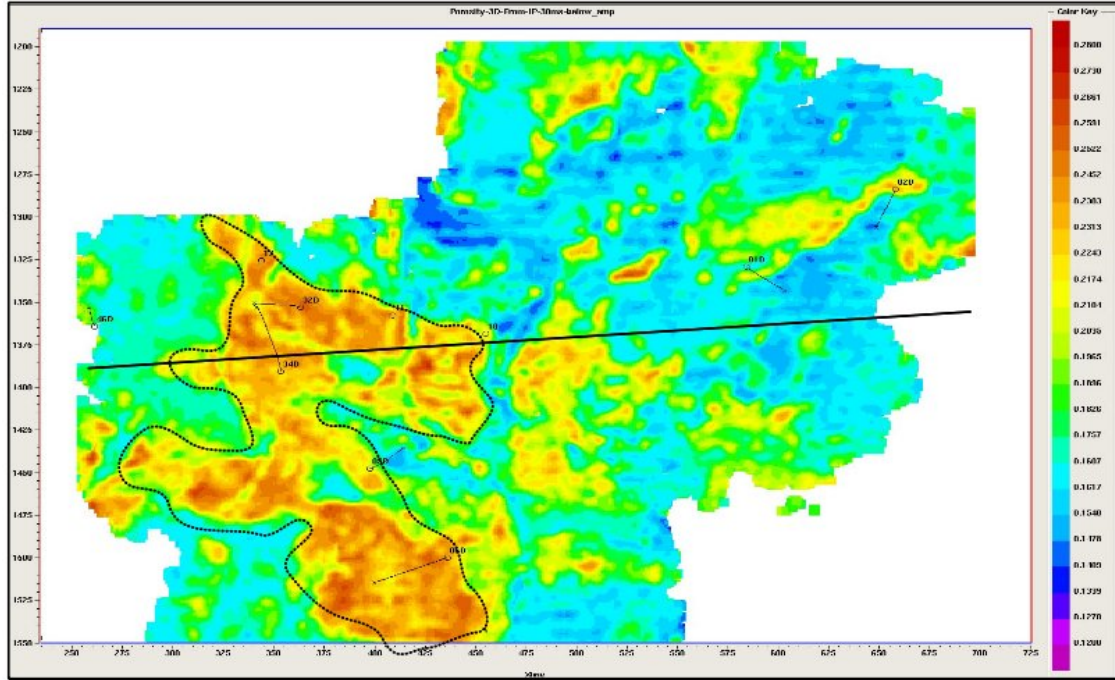
Figure 2.2: Porosity map view with the main reservoir delineated and the relative position of the 2D OBC seismic line (Martins, 2013).

a different set of receivers. Performing three separate inversions instead of an integrated one has limited the results, mainly around the areas were the separated inversions interact with each other. Table 2.1 describe the number of sources, receivers and the first source and first receiver coordinates for each of the three lines, which will be called lines 1, 2, 3.

Table 2.1: Number of sources/receivers and the first coordinate of sources and receivers for the three lines.

	# sources	# receivers	first source coordinate (m)	first receiver coordinate (m)
line 1	272	114	140	3163
line 2	336	113	1510	6415
line 3	347	247	3182	9182

Since the inversion code in limited to 2D geometry, the coordinates of each line were projected onto a 2D coordinate system (Table 2.1). Sources were fired in a flip-flop mode with constant interval of 43.75m and receivers of the ocean bottom cable were 25m equally spaced. Average deviation of approximately 30m from original coordinates were obtained in the new coordinate system. Figure 2.3 shows the 2D geometry of each line, which includes wells, sources, receivers and the initial velocity model coordinates. Line 3 was used for optimizing the inversion parametrization, because it provides the largest maximum offset among the available lines, and it would be able to measure the diving waves that traveled through the reservoir. Line 3 provides a range of maximum offsets between 3.0 km to 12.1 km. Later in this chapter I will discuss the source/receiver domain exchange.

In order to use in the waveform inversion, the field data were bandpass filtered (1Hz to 30Hz) and resampled to 4 ms. A frequency filter was applied because waveform inversion is able to recover a broadband wavenumber content without needing to use the full frequency spectrum of the data. Frequency parametrization is discussed further in this chapter. Figure 2.5 shows examples of shots from the field data and the filtered/resampled data. The image shows that the offset shot configuration changes through the survey, the signal-to-noise ratio (SNR) is pretty high, and it is possible to compare the frequency content of both data. Figure 2.4 shows the amplitude spectrum of the field, the filtered/resampled, and the pre-processed data. The source bubble ringing effect can be recognized in the amplitude spectrum.

In order to quality control (QC) the inversion results, to verify whether the update velocity model from waveform inversion has improved or not compared with the initial velocity model, pre-processed data were also delivered by Petrobras. These pre-processed data can generate better seismic images as well as common image gathers (CIG) without multiples and noise which allow an accurate interpretation of the results. A basic seismic pre-processing sequence was applied to the data which includes denoise, deconvolution, and demultiple. Figure 2.6 and Figure 2.4 show the shots examples of the pre-processed data and its amplitude

spectrum.

2.2 Objective Function

As described in section 1.2.1, the objective function is based on the difference between the modeled and observed data. Since waveform tomography is applied in the frequency domain, the data have amplitude and phase parts, and the objective function can be defined using amplitude and phase together or only amplitude or only phase (Shin et al. (2007), Bednar et al. (2007), and Pyun et al. (2007)). Because of the inherent variation of the amplitude of the data with offset and depth and to avoid dealing with it in the forward modeling code, it is more stable to define a phase only objective function, where the amplitude is ignored. Depending on the frequency content available in the data, the phase inversion can reconstruct a high resolution velocity model (Alkhalifah, 2014). In fact, the objective function here is defined in the logarithmic phase-only residuals (Equation 2.1, Bednar et al. (2007)).

$$E = \frac{1}{2} \sum_j (\delta\theta_j)^2 \quad , \quad \frac{\partial E}{\partial m_k} = Im \left[\sum_j (\delta\theta_j) \frac{1}{u_j} \frac{\partial u_j}{\partial m_k} \right] \tag{2.1}$$

2.3 Transmission Waves Inversion (Diving Waves)

Depending on the velocity gradient, diving waves travel through the earth subsurface bending back towards to the recording surface without reflecting from any sharp subsurface interface. The strategy question is: "Why should we start or focus the inversion only on diving waves?" Figure 2.7 shows a synthetic example of a trace convolved with the sensitivity kernel (Alkhalifah, 2014). Two signatures can be recognized on the image, the diving wave signature (the banana-shaped object) which shows its effective ray path (Woodward, 1992) that directly connects the source and receiver. This diving wave signature also shows the region where the inversion is capable to update the velocity model, the first Fresnel zone. In contrast, the reflection signature (elliptical object - isochrone), which also describes all possible update positions in the model, does not represent the associated ray path and thus makes it difficult to locate the update in the velocity model.
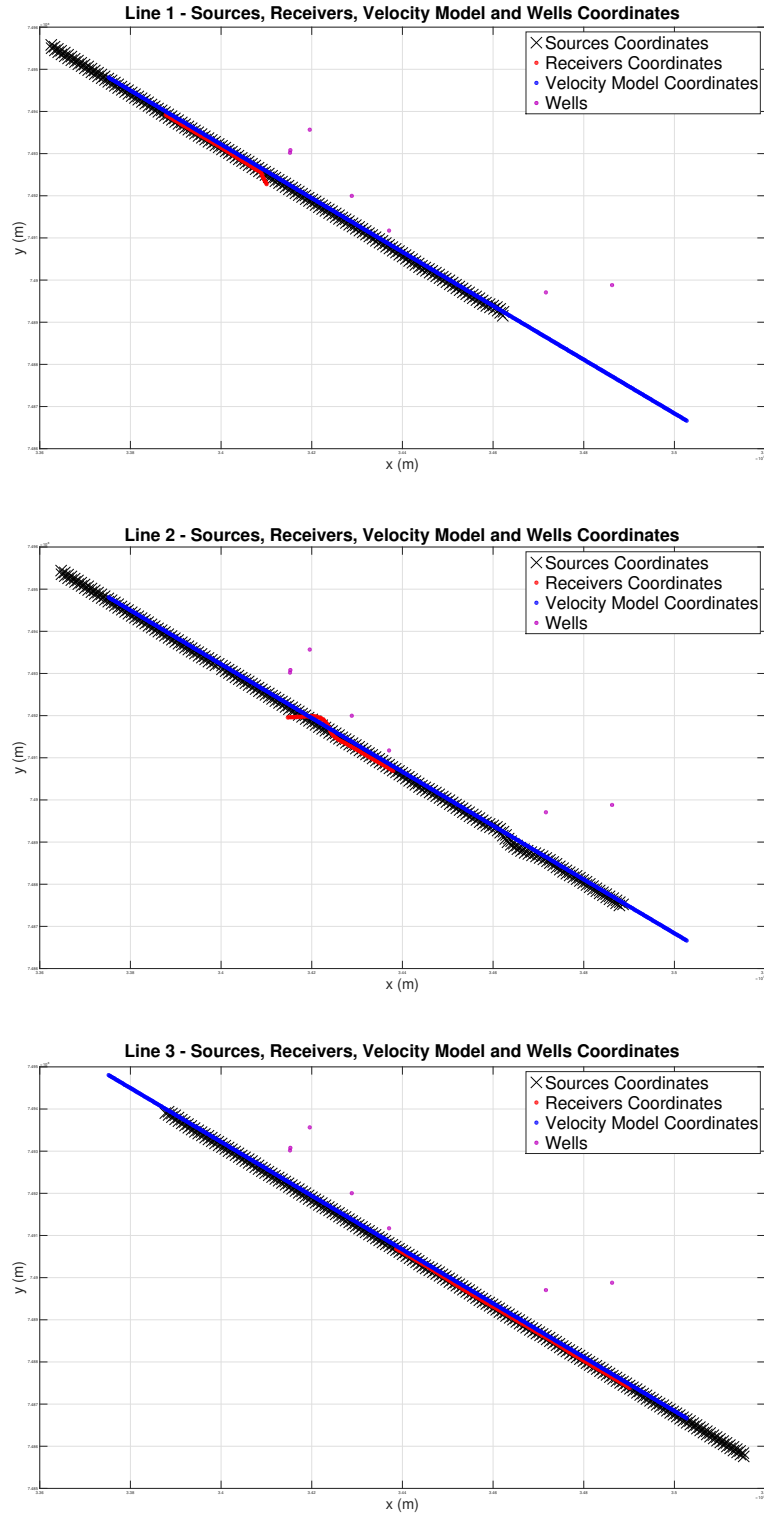
Figure 2.3: Lines 1, 2 and 3 - 2D real geometry map which includes sources, receivers, velocity model and well coordinates.
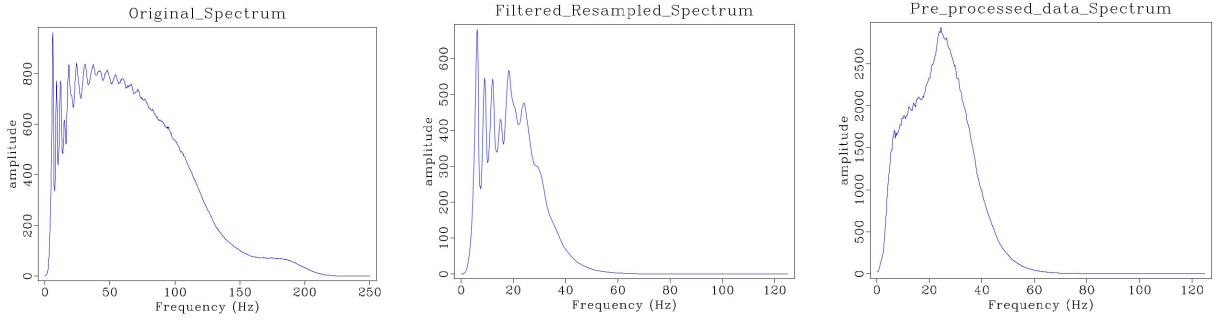
Figure 2.4: Amplitude spectrum of the original data, the filtered/resampled data and the pre-processed data.

The diving wave signature forces to focus the inversion on the diving waves to first update the background velocity model. The background update will be determined by the depth that diving waves can probe, and depends on the frequency content and offsets available in the data. Low frequency and larger offsets provide deeper background updates. In addition, it is not a good strategy to start the inversion including reflections since the initial velocity model is smooth and usually not accurate enough, which makes it difficult to generate reflections at the right times. The reflections can be included later in the inversion.

Large maximum offsets are required to measure diving waves that travel deep in the subsurface. The line 3 dataset has a fixed 6 km cable length which provides a maximum offset range between 3.0 km to 12.1 km. In order to verify whether or not diving waves traveled through the reservoir depth and were effectively measured at the sea floor, a ray tracing modeling and a sensitivity kernel analysis were performed using the initial velocity.

The initial velocity model provided by Petrobras was obtained by migration velocity analysis (MVA) and it is the final version used to migrate the conventional processed data with a Kirchhoff migration algorithm. Figure 2.8 shows the initial velocity model with physical dimensions (x,z) = (18400, 6960)m. The grid size defined to forward modeling the data up to 15 Hz is $(N_x, N_z) = (736, 290)$ with grid interval of $(d_x, d_z) = (25, 24)$m.

trace

field_data_shots

trace

filtered_and_resampled_data_shots
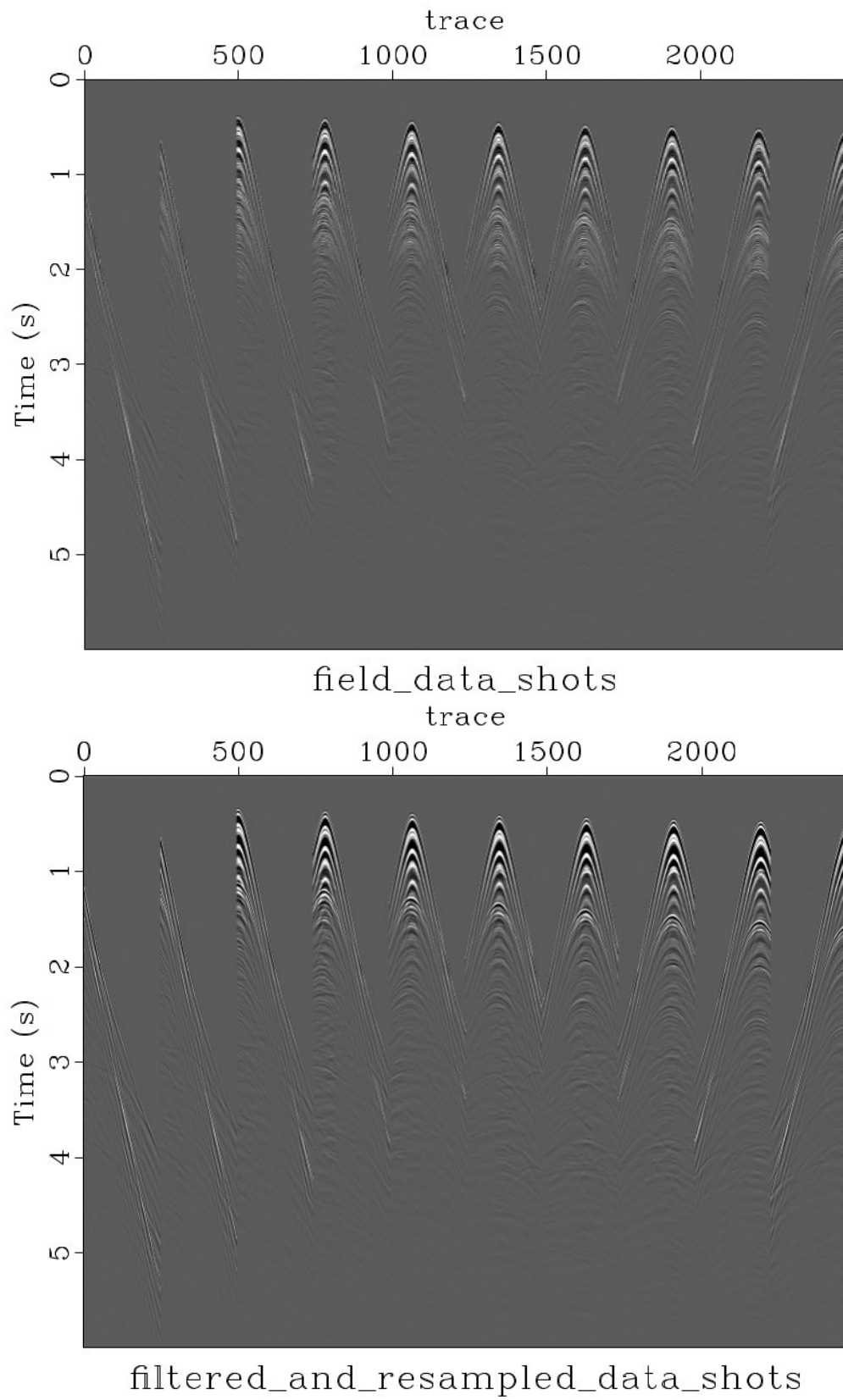
Figure 2.5: Shots examples of the original data and the filtered/resampled data.
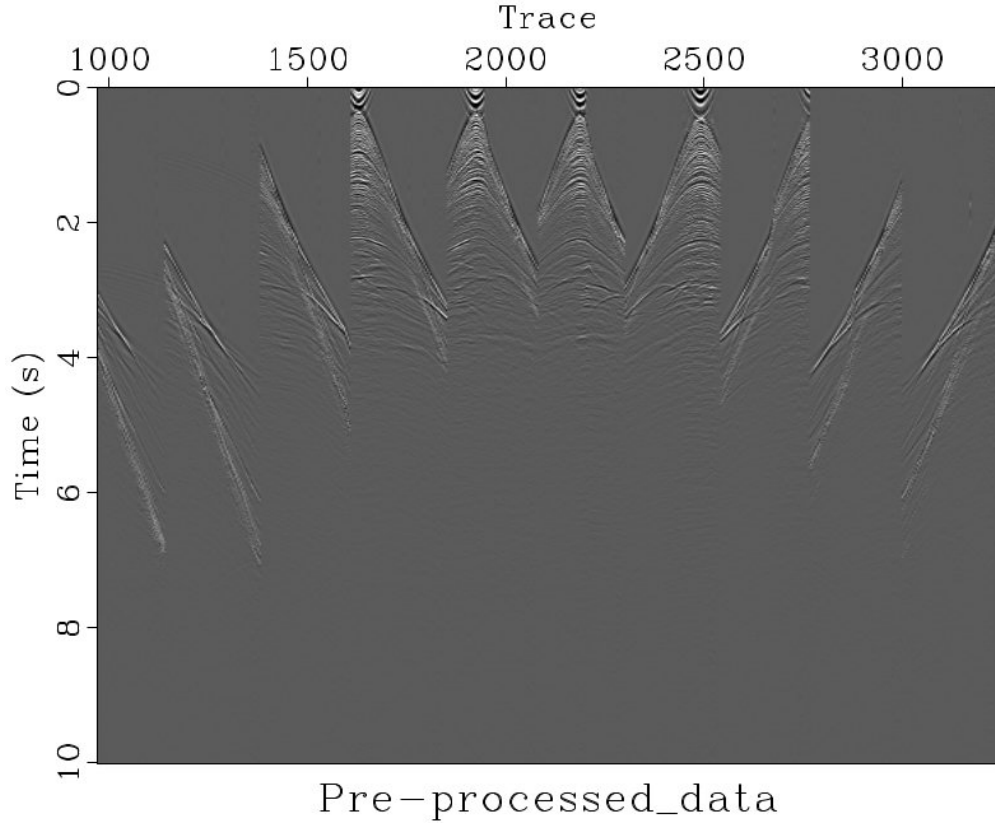
Figure 2.6: Shots examples of the pre-processed data.
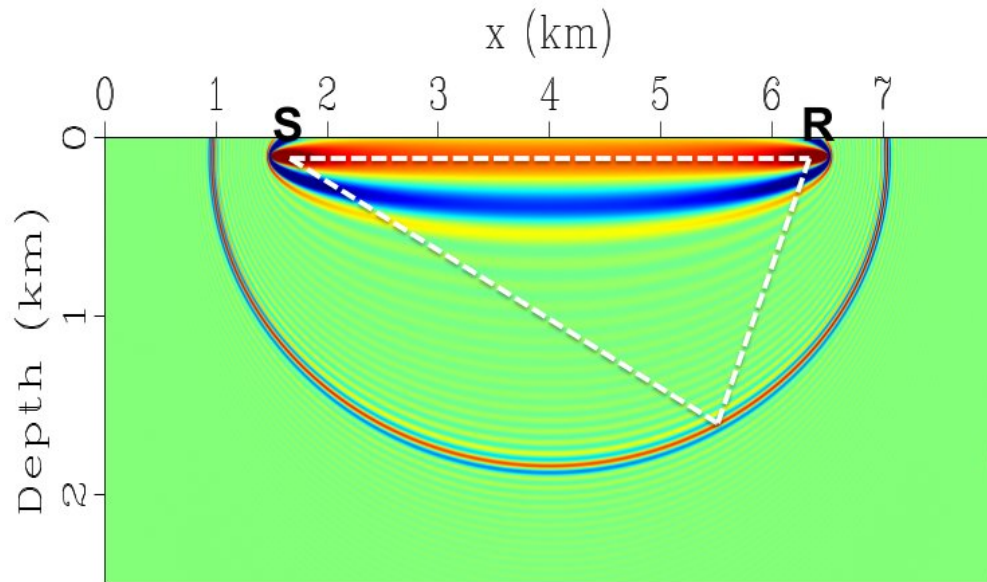
Figure 2.7: Synthetic example of the sensitivity kernel convolved with the synthetic trace. Image shows the diving waves and the reflection signatures (modified from Alkhalifah (2014)).

Figure 2.9 shows the ray tracing modeling for three shots in different positions of the survey. Essentially, the rays show the average behavior of the diving waves, how deep they can travel and the range of offsets that they would be measured by the receivers laid in fixed positions on the sea floor. Therefore, the diving waves will only travel through a fixed area of the model, and reach the reservoir area. The main reservoir is located at depths between 2.5 km to 2.8 km and between 3.0 km to 7.0 km position in the x-direction. Focusing the inversion on diving waves and at the depth of the reservoir, the ray tracing analysis showed that the initial velocity model could be reduced in depth, from 6.96 km to 4.08 km, hence making the waveform inversion faster with an smaller number of model parameters (number of equations). The reduced initial velocity model is shown in the Figure 2.8.
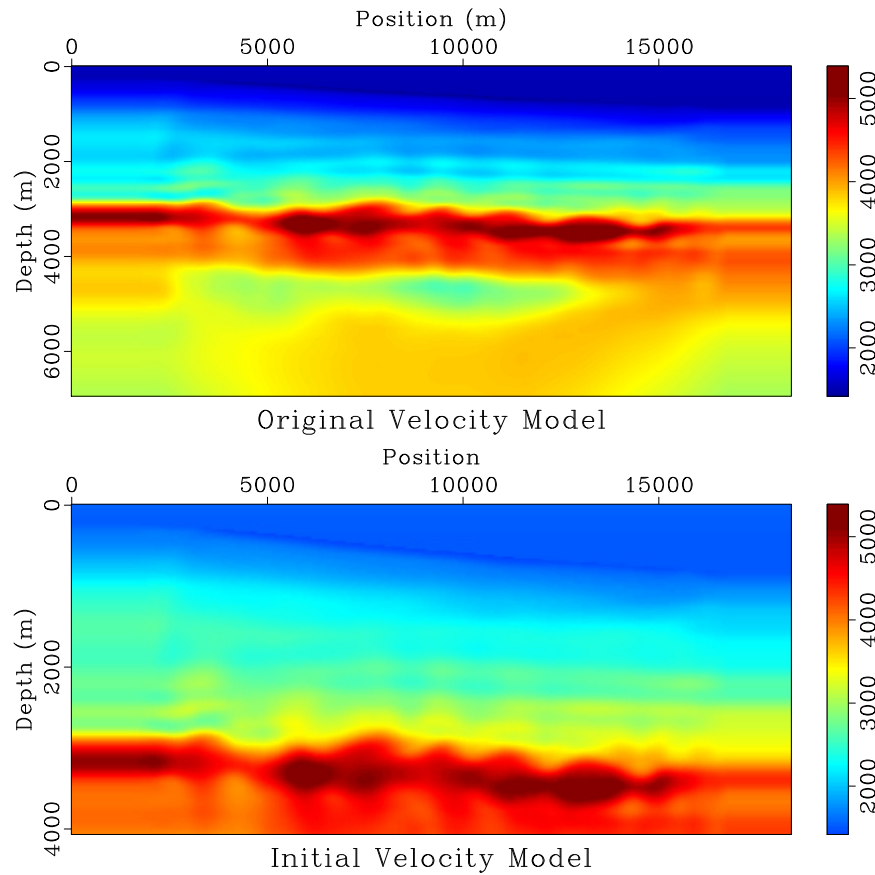
Figure 2.8: Original P wave velocity model provided by Petrobras (top) and the reduced velocity model used in the inversions after ray tracing evaluation (bottom).
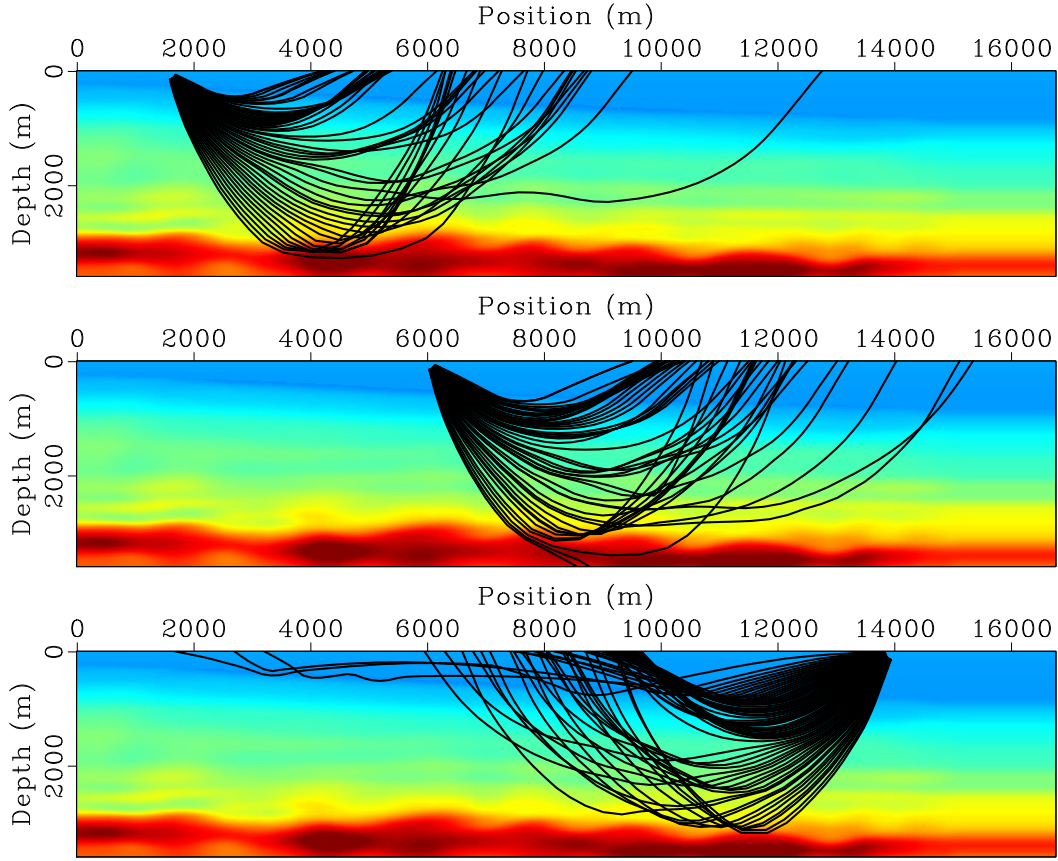
Figure 2.9: Ray tracing modeling showing the average behavior of the diving waves for three different sources positions.

The sensitivity kernel is computed by multiplying the monochromatic wavefields from any source and any receiver. Figure 2.10, Figure 2.11 and Figure 2.12 show several computed sensitivity kernels using the initial velocity model for three different offsets and three different monochromatic frequencies. The idea is to evaluate if the inversions will be able to update the velocity model at a certain depth, in our case, the depth of the reservoir. The sensitivity kernels generally showed that for lower frequencies and independent of offset the wavefield is sensitive through the entire model, where the diving waves update (first Fresnel zone) has a limited depth extent up to approximately 2.0 km and reflections update reach deeper part of the model. The sensitivity extent decreases throughout the model for higher frequencies, although it reaches effectively the depth of the reservoir around 2.5 km. The best updates

for higher frequencies are achieved for intermediate and large offsets. This depth limitation update is closely related with the higher velocity layer below the reservoir which is composed of carbonate and salt deposits. When waves reach the high velocity layer, part travels back as diving waves and the other part passes through the layer with small bending angles and therefore creating shadow sensitivity zones below the high velocity layer.
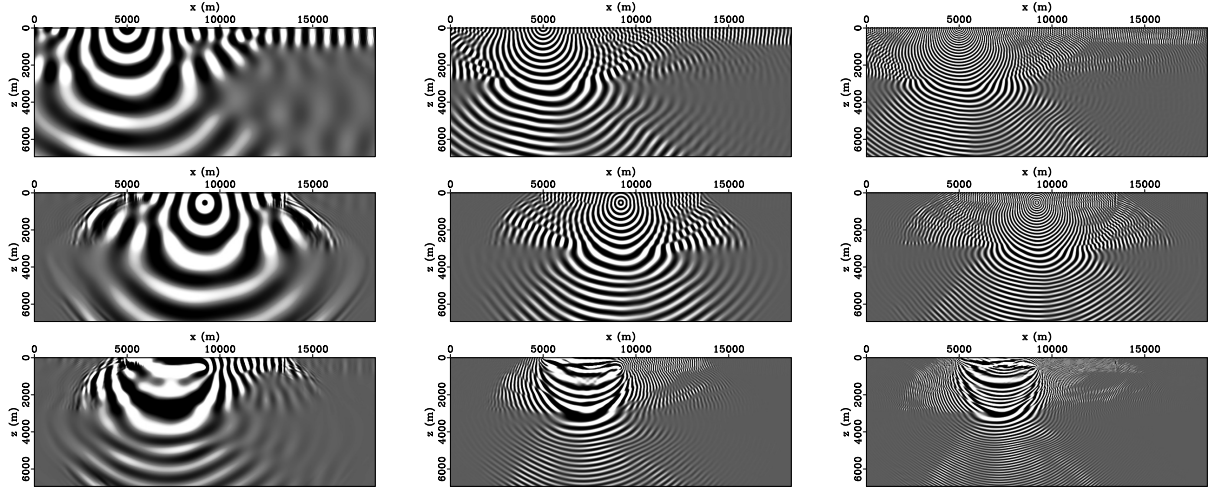
Figure 2.10: Sensitivity kernel for small offset (4.0km) and three different frequencies: 2.0Hz (left), 7.5Hz (middle) and 15Hz (right).
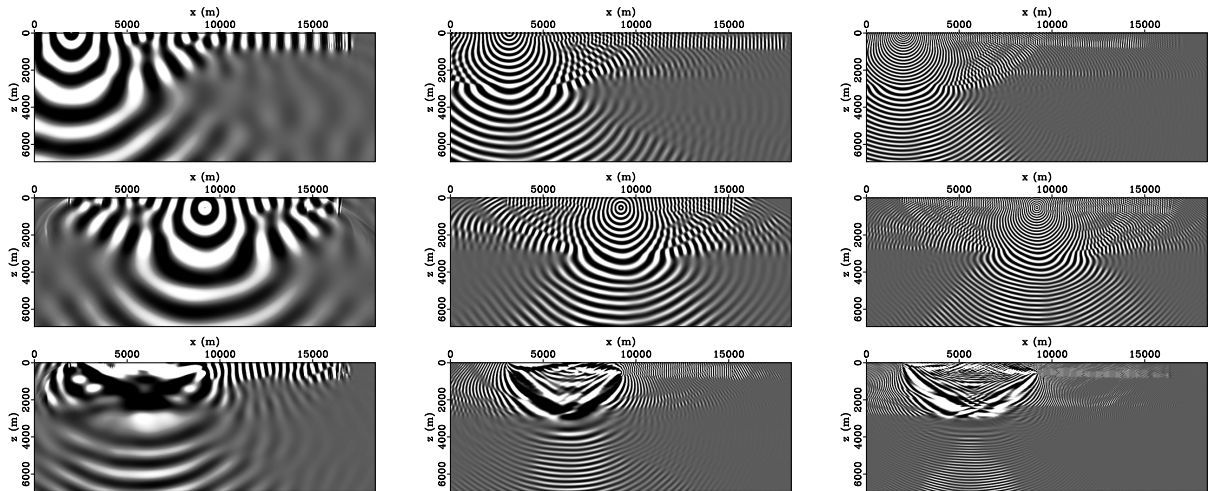
Figure 2.11: Sensitivity kernel for intermediate offset (6.0km) and three different frequencies: 2.0Hz (left), 7.5Hz (middle) and 15Hz (right).
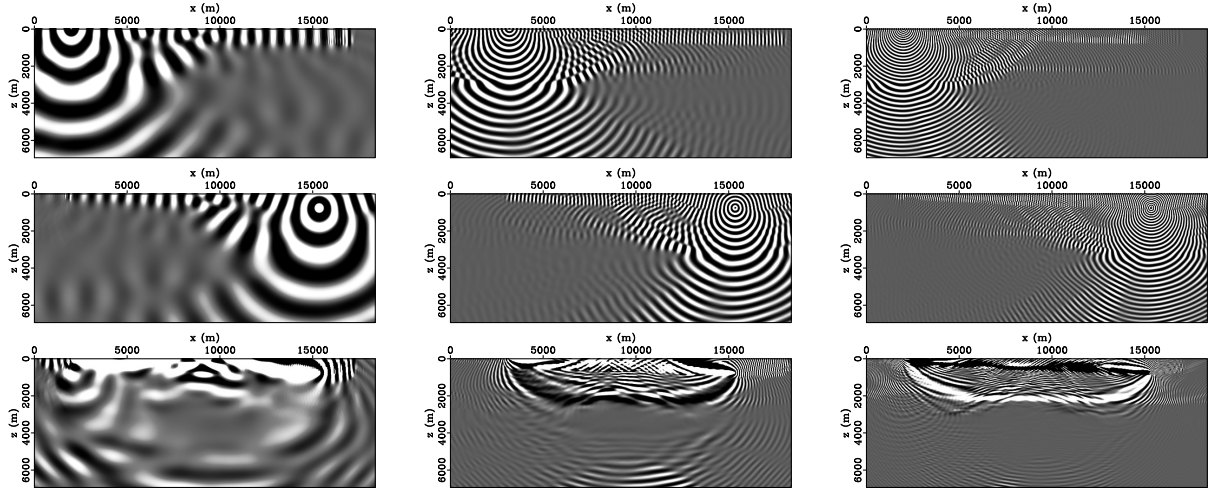
Figure 2.12: Sensitivity kernel for larger offset (12.0km) and three different frequencies: 2.0Hz (left), 7.5Hz (middle) and 15Hz (right).

2.4   Time domain damping (τ) - Data Selection

The time domain damping (τ) is used in the frequency-domain waveform inversion for two different purposes. First, to avoid the time-aliasing (wrap-around in time domain) when the choice of frequency sample interval does not consider the maximum signal time ($t_{max} = 1/\Delta f$). Any signal outside the minimum and maximum time will be shifted in time changing the Fourier summation (Pratt, 2013). However, the main reason to use time domain damping is to select the data that will be included in the inversion process. Figure 2.13 shows the time domain damping being applied to a synthetic signal ($e^{\frac{-t_{max}}{\tau}}$).

The waveform inversion code provides four options to apply the time domain damping in the data and Figure 2.14 shows how each one can be applied in a shot as an example: a) top left, the idea is to start the time damping at the picked first arrivals time; b) top right, the time damping starts at an estimated first arrival time computed by $t = \left(\frac{offset}{v_{min}}\right)$ s; c) bottom left, a linear moveout is applied to the data and the time domain damping starts at some constant initial time, in the image t = 0 s; d) bottom right, time damping is directly applied to the data and starts at a constant time, for example, t = 0 s. The later one is the simplest version and it is the one used in this project. It might not be the best option

23

because it suppresses useful diving waves in the data at larger offsets. In order to check how the time damping works in the data Figure 2.15 shows one shot example without damping and the same shot with different time damping parameter $\tau = 1, 2, 4$ s. When comparing the damped shots with the original one, we see how much of the data is attenuated, in both depth and offset. Therefore, time damping is a useful tool to select the data that will be included in the inversion.
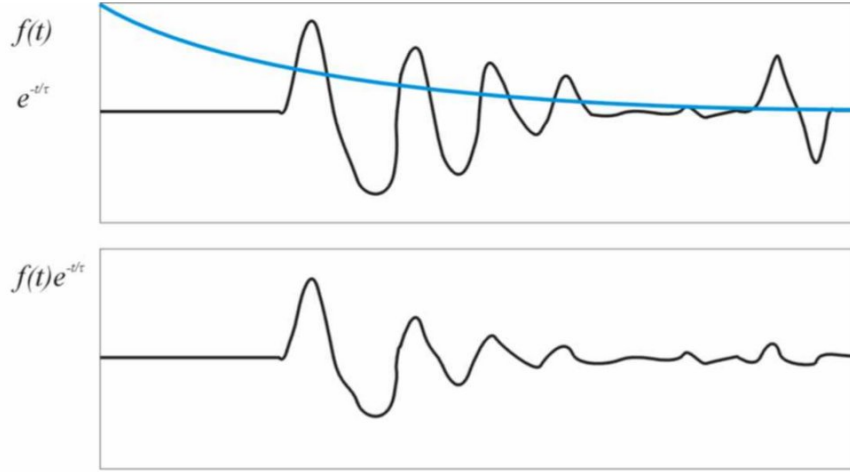
Figure 2.13: Time domain damping applied in a synthetic signal ($e^{\frac{-t_{max}}{\tau}}$), modified from Pratt (2013).

As discussed, the waveform inversions are focusing on diving waves. In order to avoid reflections, a strong time damping can be helpful in attenuating the later arrivals. Likewise, larger offsets are more sensitive to errors in the velocity model, which means that modeled data can be generated with a time delay larger than half cycle from the observed data, in other words, can be cycle skipped. Non-linearity (cycle-skipping) in waveform inversion is discussed in the next section 2.5 about frequency discretization. In addition, after the background velocity model is updated by the first few inversions, reflections may be included in the inversions by relaxing the time domain damping parameter.

It is worth mentioning that the shots presented in Figure 2.14 and Figure 2.15 are not the original ones. Sources and receivers were interchanged by applying reciprocity. The

reciprocity was used here because kinematically works in acoustic assumption and inversions were performed usnig only the phase of the data. In this project, this change reduced the computation time by approximately 1/3.
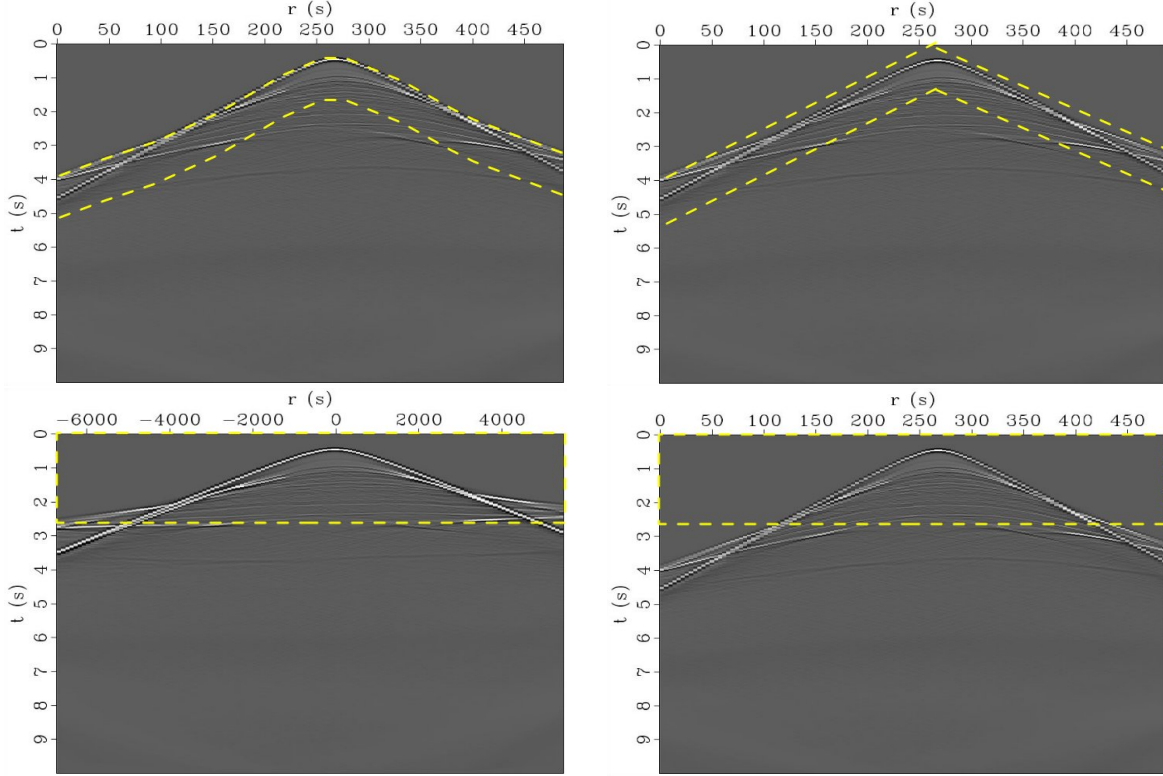
Figure 2.14: Time domain damping strategies: a) top left, the time damping starts at a picked first arrivals time; b) top right, the time damping starts in a estimated first arrival time computed by $t = offset/v_{min}$; c) bottom left, a linear moveout is applied to the data and the time domain damping starts at some constant initial time, in the image t=0s; d) bottom right, time damping is directly applied in the data and starts at a constant time, for example, t=0s.

2.5 Frequency Discretization

Frequency discretization is based on the approach developed by Sirgue and Pratt (2004), where they theoretically proved for 1D model, that a single frequency and a range sources/receivers offsets $[0, x_{max}]$ can recover a range of vertical wavenumbers $[k_{zmin}, k_{zmax}]$. Each source/receiver pair contributes for a single vertical wavenumber. Furthermore, this strategy also showed to be capable in dealing with 2D more complex models, where the structures

are nonhorizontal, the incident and scattering angles are different, therefore a range of non vertical wavenumbers can be recovered.
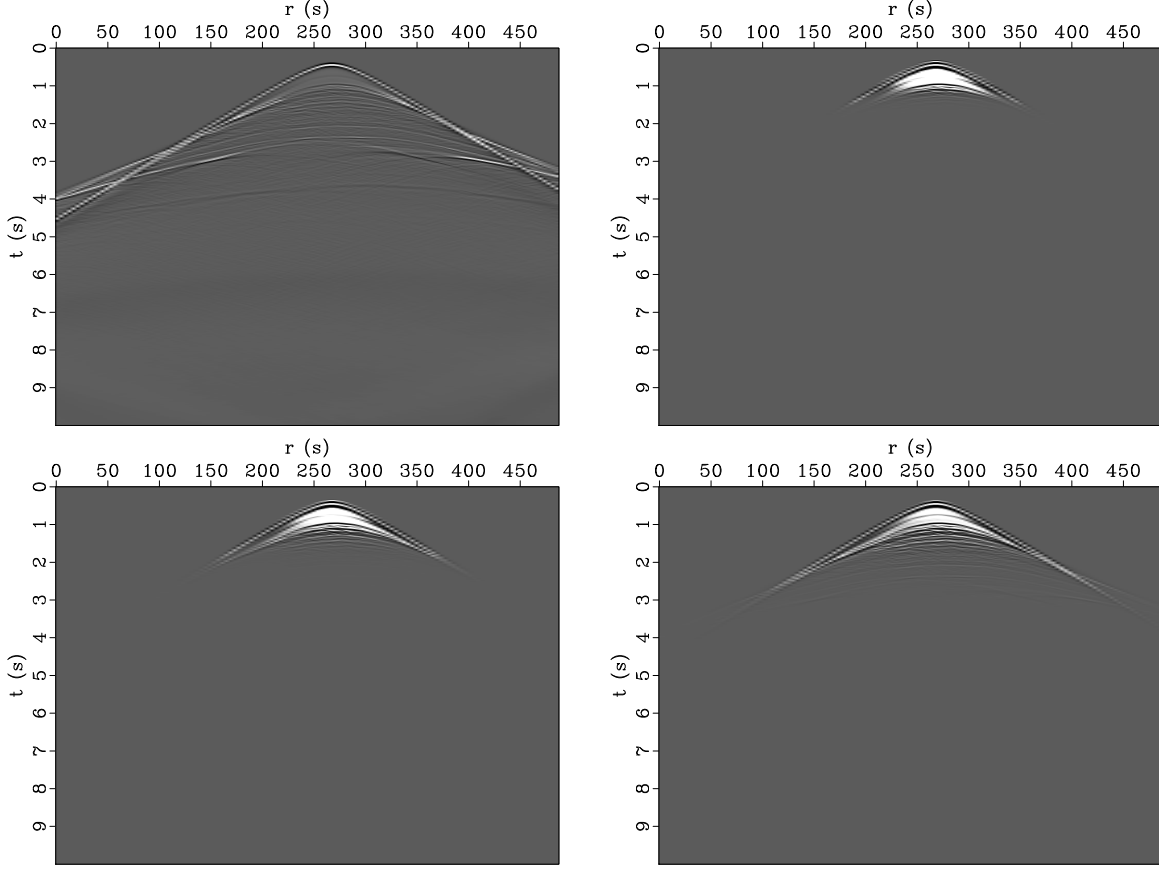
Figure 2.15: Shot example with different time domain damping (τ) parameter: a) top left, without time damping; b) top right, time damping $\tau = 1s$; c) bottom left, time damping $\tau = 2s$; and d) bottom right, time damping $\tau = 4s$

The frequency discretization always provides a much smaller number of frequencies to be inverted when compared with the number of frequencies provided by Sampling Theorem. It is one of the biggest advantages of performing the waveform inversion in the frequency domain. Following the frequency discretization strategy, given by Equations 2.2, where $h_{max} = 3.0$ km is the maximum half offset survey and $z = 3.0$ km is the depth of the target (reservoir), the frequencies to be inverted were computed and are shown in Table 2.2.

$$R_{max} = \frac{h_{max}}{z} \ , \quad \alpha_{min} = \frac{1}{\sqrt{1 + R_{max}^2}} \ , \quad f_{n+1} = \frac{f_n}{\alpha_{min}} \tag{2.2}$$

26

Instead of inverting for 150 frequencies, up to 15 Hz with $\Delta f = 0.1$ Hz given by the sampling theorem, the frequency discretization provided seven frequencies to be inverted ($f = 2.0, 2.8, 4.0, 5.6, 8.0, 11.3$ and 15)Hz. Clearly, the number of frequencies is drastically reduced, and this reduction mostly depends on the maximum offset available on the acquisition design. Since we are dealing with real data, which includes noise, I added 3 or 4 frequencies to each selected frequency which built groups of frequencies that are described in Table 2.2. This group approach helps to suppress the influence of noisy data with redundance in the recovered wavenumber in each group.

Table 2.2: Frequency discretization for Campos Basin OBC dataset.

frequency (Hz)	f_1	f_2	f_3	f_4	f_5
group 1	2.0	2.2	2.4	2.6	-
group 2	2.8	3.1	3.4	3.7	3.9
group 3	4.0	4.4	4.8	5.2	5.5
group 4	5.6	6.1	6.6	7.1	7.7
group 5	8.0	8.7	9.4	10.1	10.8
group 6	11.3	12.3	13.3	14.3	15.0

Figure 2.16 shows the frequency discretization for 1D velocity model of $v = 1.5km/s$ and helps us to understand redundance in the wavenumber recovery, since the groups of frequencies overlap the recovered wavenumber of each other.

In order to compute the frequencies to be inverted one needs to define the lowest reliable frequency in the data. Figure 2.17 shows the real part of the line 3 dataset for four different low frequencies ($f = 1, 2, 3, 4$ Hz) which its SNR is visually recognizable. Each panel represents the entire data for a particular frequency, where receivers are in the x-direction and the sources are in the z-direction. Each source/receiver pair is a complex data with real and imaginary part and in these panels the amplitude of the real part is plotted. The SNR attribute was used to choose the lowest frequency to start the inversions. Comparing the four components of the data the most conservative choice would be 3 Hz frequency compo-
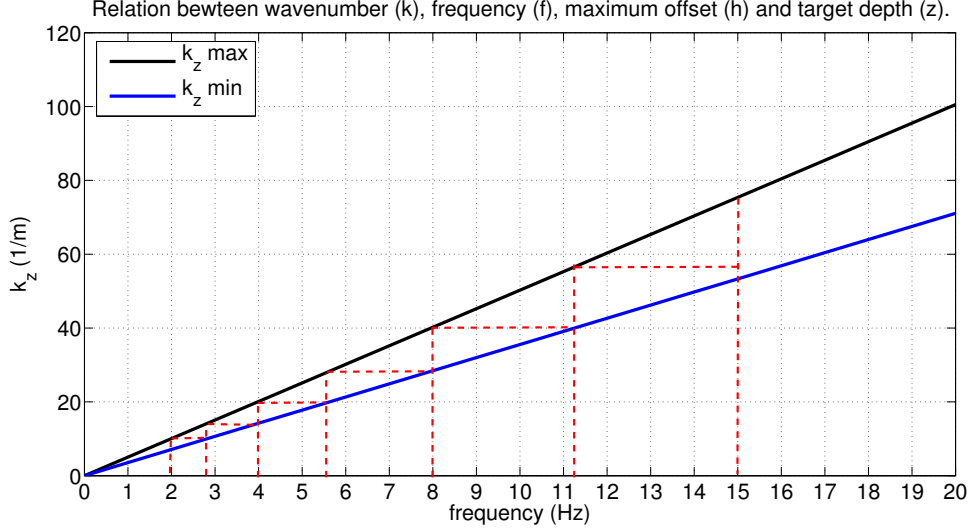
Figure 2.16: Relation between vertical wavenumber (k_z), frequency (f), maximum effective offset (h) and target depth (z) for 1D velocity model ($v = 1.5$ km/s) (Sirgue (2003) and Sirgue and Pratt (2004)).

nent, because it has the best trade-off between SRN and the lowest frequency component. However, 2 Hz component is still presenting a good SNR and a lowest frequency option can better help overcome the non-linearity of the objective function. As mentioned before, the basin of attraction of the objective function and the half cycle of the data increases for low frequencies. Because of this fact, the starting inversion frequency was selected as 2 Hz.

The non-linearity, or cycle skipping problem, is illustrated in the Figure 2.18. It shows two different modeled traces for a single frequency (dashed lines), one with time delay more than half cycle (top) and one with time delay less than half cycle (bottom). WT will match both traces with the observed trace (solid line) minimizing the objective function, although in different directions. The top trace influenced by cycle skipping is being corrected in the opposite direction, which leads to a wrong velocity model.

Another advantage to perform waveform inversion in the frequency domain is the more natural way to apply the multi-scale approach. The multi-scale approach starts the inversion with the lowest frequency of the data, which is less sensitive to cycle-skipping issue, and then sequentially invert for higher frequencies. This type of approach is effective to overcome the

non-linearity of the objective function, avoiding being trapped in a local minima. After each frequency inversion the velocity model is more accurate and for the next higher frequency the modeled data will be within a half cycle from the observed data.
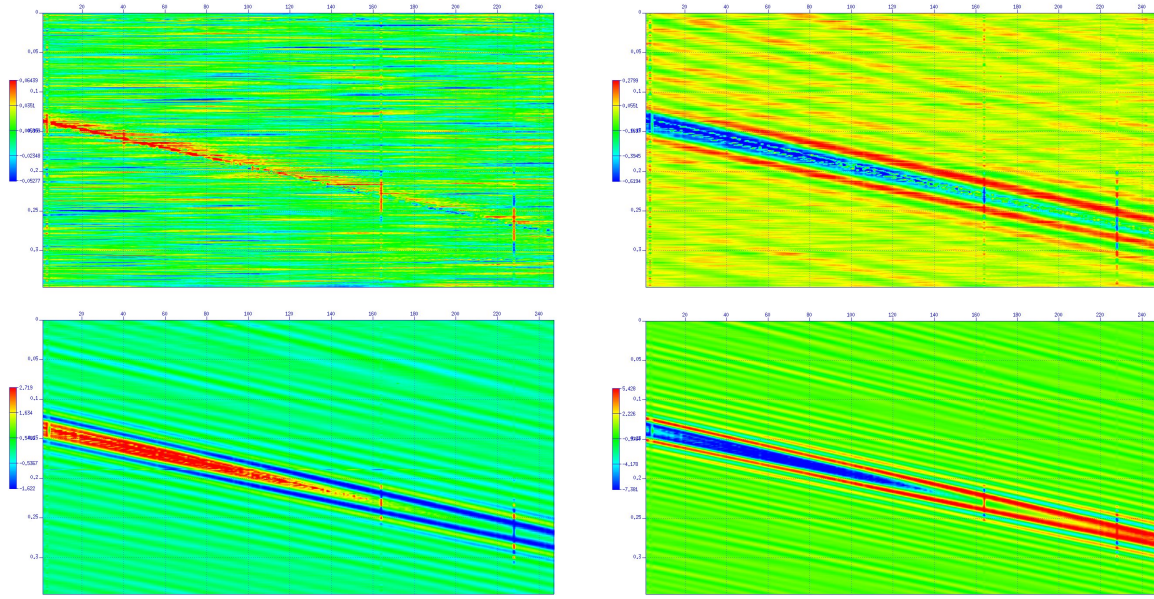
Figure 2.17: Amplitude of the real part of the data for four frequencies: a) top left - f=1Hz; b) top right = f=2Hz; c) bottom left - f=3Hz and d) bottom right - f=4Hz. Each pair source/receiver is a complex number, the plots here show the real part of all pairs sources/receivers in the form (x,z)=(sources x receivers).

Figure 2.19 shows a basic flow chart of waveform inversion for a single frequency, where the velocity model and the source signature, extracted from the data, are used to generate the modeled data which are compared with the observed data for one specific frequency. After several iterations, or after the inversion reached some convergence criteria, the velocity model is updated and the inversion moves to the next higher frequency. Here, the convergence criteria used are based on the analysis of the objective function convergence which defined an optimum number of waveform inversion iterations.
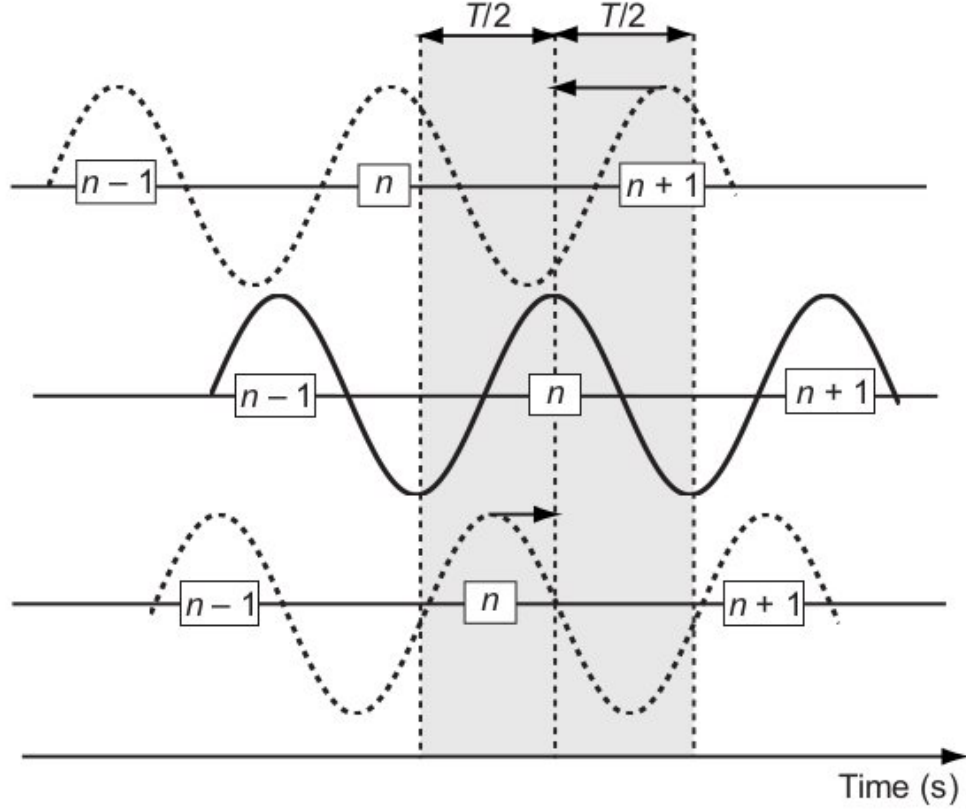
Figure 2.18: Cycle skipping problem illustration. The image shows two different modeled traces (dashed lines), one with time delay mode than half cycle (top) and one with time delay less than half cycle (bottom). WT will match both traces with the observed trace (solid line), although in different directions. The top trace will be cycle skipped being corrected in the opposite direction, which leads to a wrong velocity model (modified from Virieux and Operto (2009)).

2.6 Convergence Analysis of the Objective Function

The first few inversions and the wavenumber filter (pre-conditioning) tests were performed with only 5-10 iterations per group of frequencies. However, to better define an optimum number of iterations several tests were performed looking at the general behavior of the objective function convergence, which is shown in Figure 2.20. It indicates that the convergence is reached between 15 to 25 iterations. The number of iterations for inversion was increased up to 15 to optimize the trade-off between the objective function convergence and the computation time in each iteration. The objective function is reduced by 2% between 15

30

and 25 iterations; however, the computation time is almost 60% longer. Figure 2.21 shows the convergence for each group of frequency during the inversions, all of them converged to a stable minimum value after the 10th iteration.
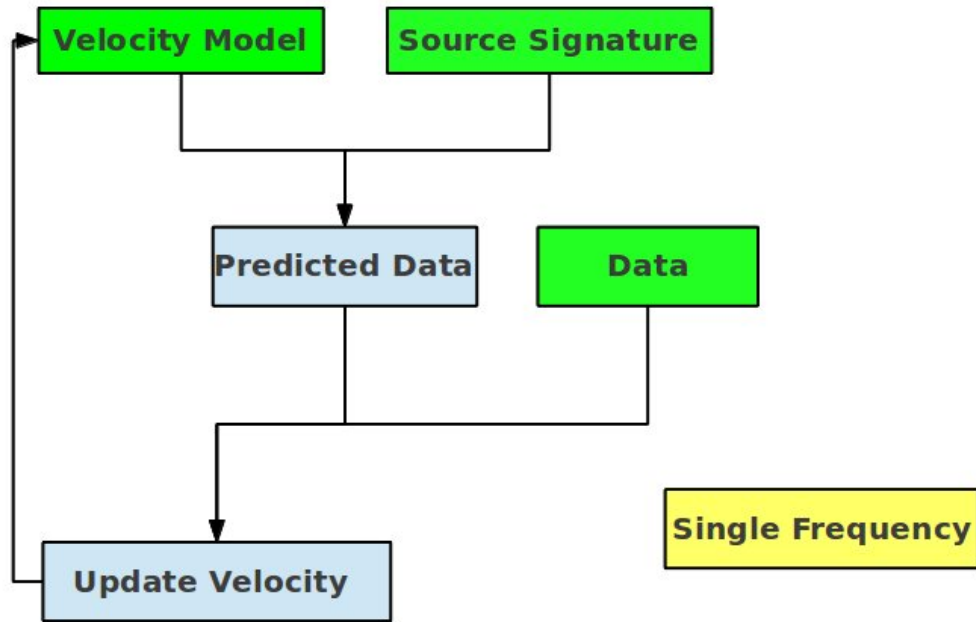
Figure 2.19: Flow chart for WT inversions for a single frequency.
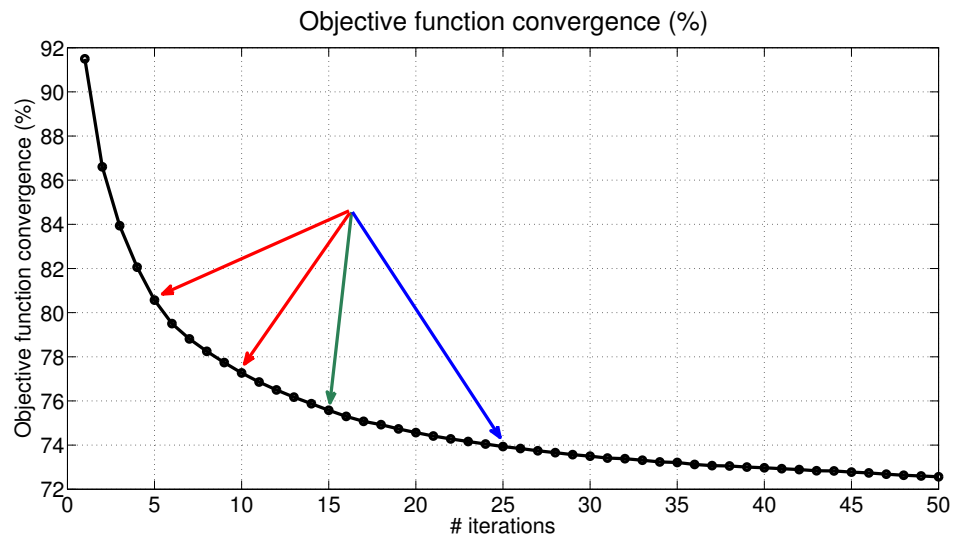
Figure 2.20: General objective function convergence.
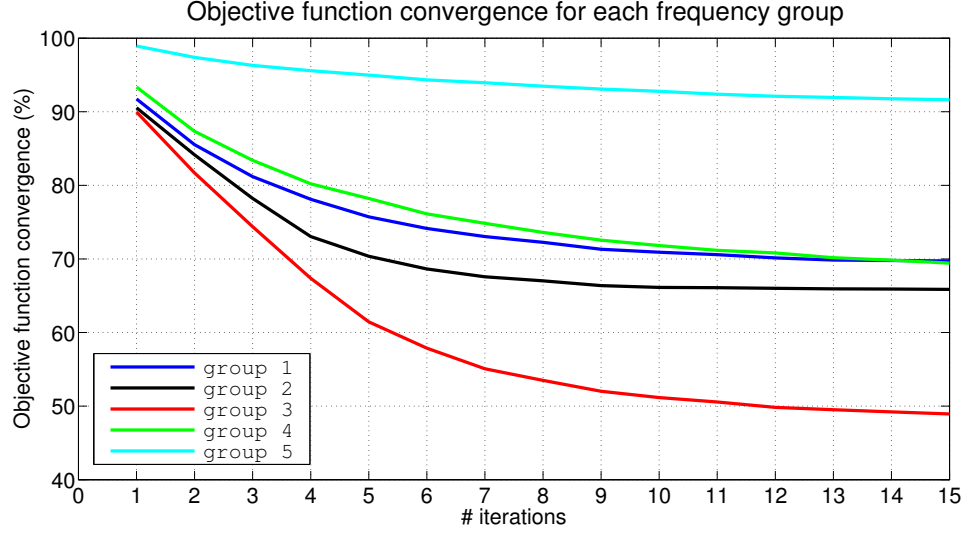
Figure 2.21: Objective function convergence for each group of frequency.

2.7 Preconditioning the Gradient Vector

As described in section 1.2.1, the Newton algorithm solution includes the Hessian matrix ($\mathbf{H}$), which is a type of filter that modifies the gradient direction to improve convergence properties. The Hessian matrix is ignored in our solution and the gradient of the objective function is dominated by high wavenumbers (Sirgue, 2003). It requires some type of preconditioning of the gradient in order to ensure that the solution converges to the global minimum. There are several different types of preconditioning, but here I only use the preconditioning of the gradient by wavenumber filtering.

A 2D low-pass elliptic/circular filter is applied to the gradient in the wavenumber domain to remove the high wavenumber components. The 2D low-pass filter is shown in the Figure 2.22 and depending on the choice of maximum vertical (k_{zmax}) or horizontal (k_{xmax}) wavenumbers the filter will be elliptical or circular. Because the earth is more horizontal layered, it is acceptable to have higher wavenumbers update in the vertical direction, hence the filter will always be elliptical with a larger vertical axis than a horizontal axis ($k_{zmax} > k_{xmax}$). Each frequency group (Table 2.2) has its own optimized wavenumber filter, which, in practice, is obtained by interpreting the gradient after performing an inversion

without a wavenumber filter. The idea is always to avoid higher wavenumbers that are not expected in the gradient for that specific group of frequencies ($k_{max} = f_{max}/v_{min}$).
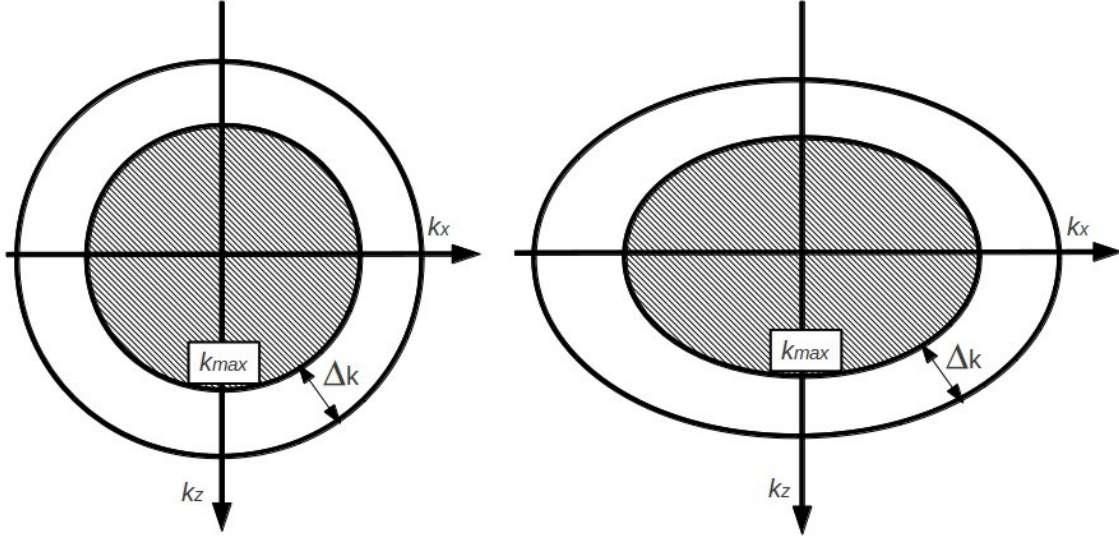
Figure 2.22: Low-pass 2D elliptic/circular filter applied to the gradient vector in the wavenumber domain, preconditioning the gradient vector.

Figure 2.23 shows the gradient for two different groups of frequencies, group 3 and group 5. From top to bottom it was applied two processes to the gradient: a) the first process is a mask that excludes any update in the velocity model above the sea floor, a reasonable assumption that the water layer has a well defined velocity in the model (Figure 2.24); b) the second process is the wavenumber filtering. In general, all gradient images were improved by the described process during the inversions and probably has helped to improve the convergence of the objective function to the global minimum.

2.8 Inversion Results

Throughout the previous sections, I have discussed waveform inversion, its capability to reconstruct the velocity model, the mathematical difficulty involved and the drawbacks imposed by data limitations. The main objective is to obtain a more accurate and higher resolution velocity model.
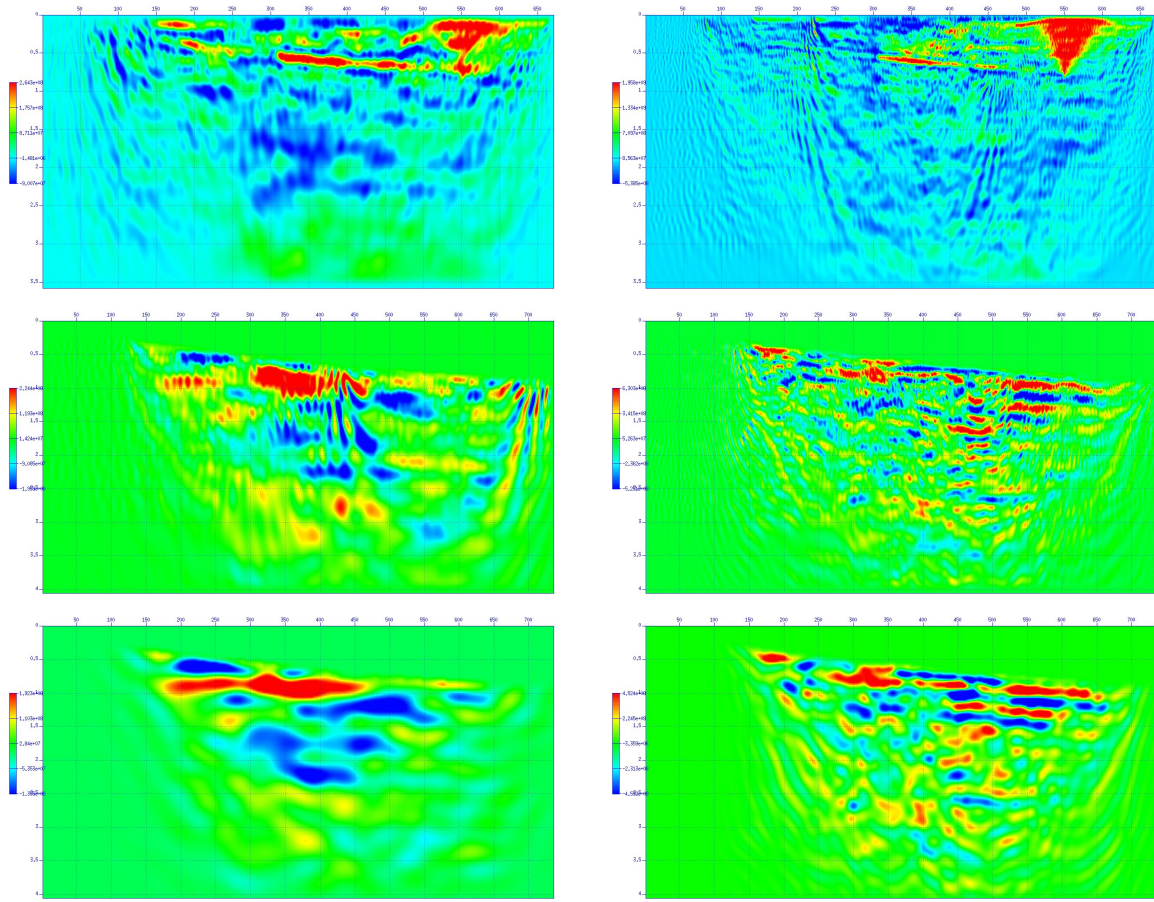
Figure 2.23: Gradient images masked and filtered to improve the convergence of the objective function to the global minimum. Left column shows the result for group 3 and right column for the group 5.
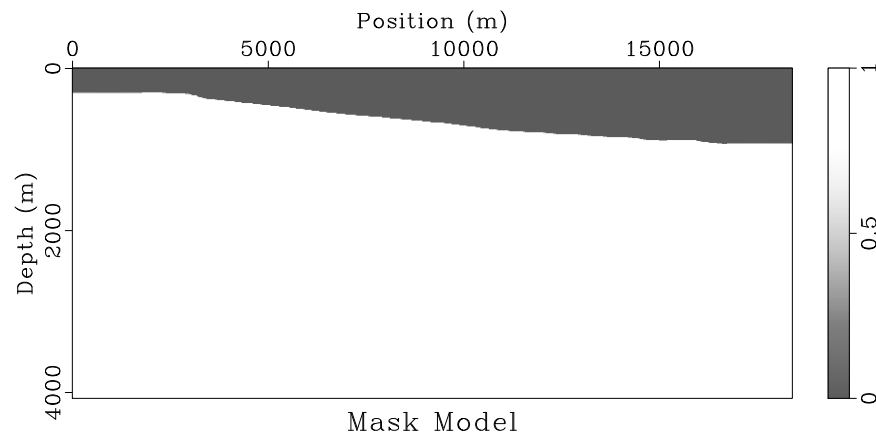
Figure 2.24: Mask to exclude any update in the velocity model inside the water layer.

The results presented in this section describe the updated velocity model for each line. These results were obtained by performing waveform tomography in the frequency domain. The objective function is based only on the phase residuals (option provided by the code), the time domain damping parameter is fixed at 4 s (only one), and the group of frequencies described in Table 2.2 reaches a maximum inverted frequency of 15 Hz. All tests to optimize the inversion were done on line 3, which provides the largest offset among the three lines (line 1, 2 and 3). Figure 2.25 shows the initial velocity model with the 2D geometry of the three lines with sources (blue) and receivers (green). Each line has a cable length of 2.8 km, 2.8 km and 6.2 km, respectively. Because it was not possible to integrate the three lines into a simple one, the main reason to choose line 3 to test and optimize the inversion is its cable length. Therefore, waveform inversion of lines 1 and 2 was performed by directly applying the same parametrization designed for line 3.

Figure 2.26 shows the final waveform inversion results for line 3. The image includes the initial and final velocity models, and also the velocity difference (final - initial), which makes it easier to identify the update in the velocity model. Noticeable updates can be recognized throughout the entire model. Higher wavenumbers were locally introduced by the inversion in the shallow part of the model close to the sea floor. In addition, there is a strong update in the deepest part of the model, overall decreasing the velocity, where we have the high velocity layers composed of carbonate/salt. Between 500 m to 2500 m the update mostly increased the velocities with an horizontal orientation that follows the main geological horizons of the area (Figure 2.32). The velocity difference emphasizes the update in the final velocity model.

Figure 2.27 and Figure 2.28 show the final results for lines 1 and 2, they follow the same general trend of the update obtained for line 3. Quality control (QC), presented in the next section, was performed in order to check the waveform inversion results, such as migrated seismic image, common image gathers (CIG) and data phase difference, which allows to evaluate the inversion process and the accuracy of the velocity model.
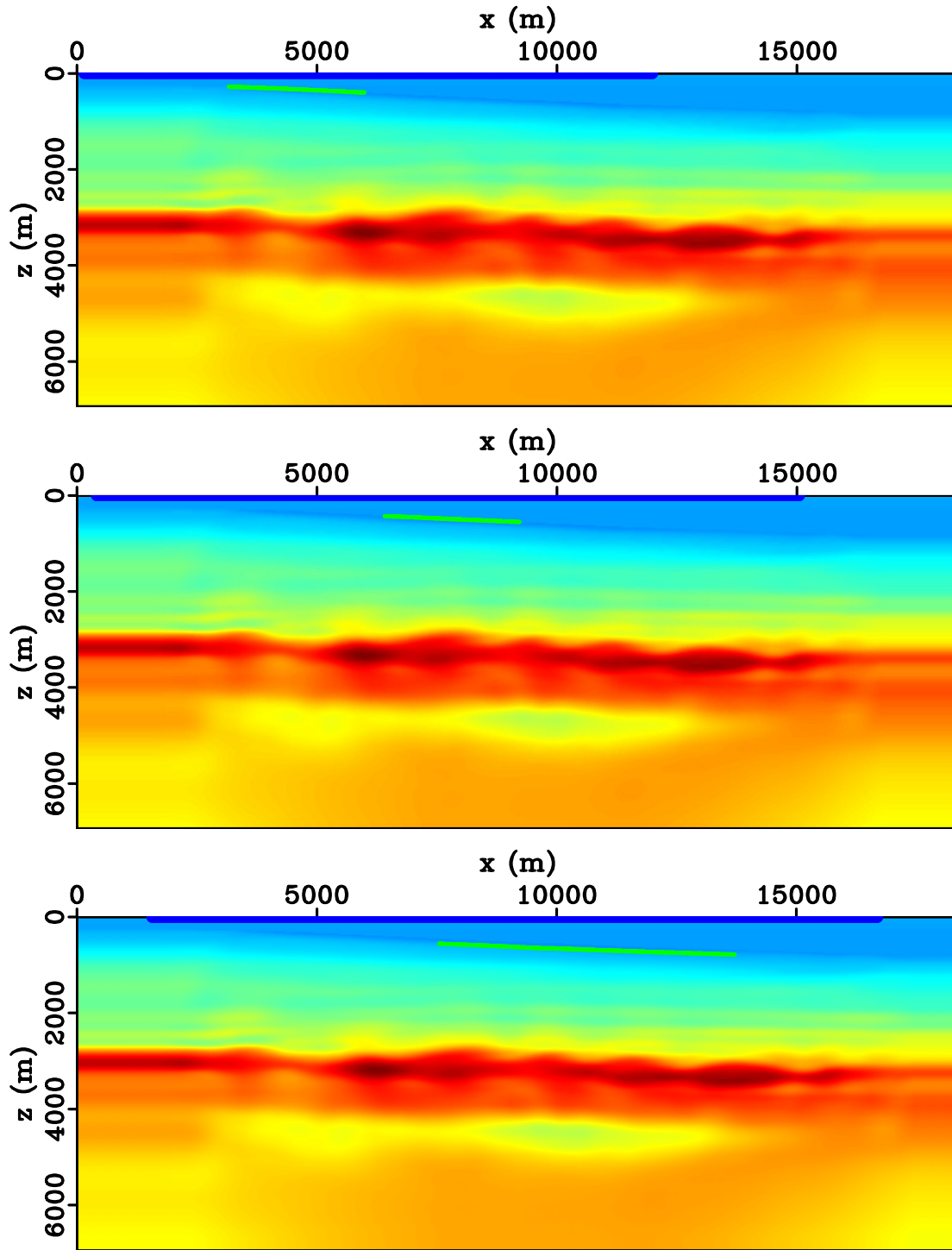
Figure 2.25: 2D geometry configuration with sources (blue) and receivers (green) of the three lines, line 1 (top), line 2 (middle) and line 3 (bottom) and the initial velocity model overlaid. Line 1, 2 and 3 cable length are approximately 2.8km, 2.8km and 6.2km, respectively.

It is interesting to comprehend how waveform inversion updates the velocity model using the multi-scale approach, when the inversion starts with low frequencies components and gradually inverts for higher frequencies. By Figure 2.29 and Figure 2.30 it is easy to identify the update of the velocity model, after the inversion for each group of frequencies. Both images show from group 1 (top-left) to group 6 (bottom-right) that new information is introduced in the velocity model after each inversion. First, the process corrects the background velocity model with the low wavenumbers and gradually introduces information from higher wavenumber in the velocity model. The waveform inversion applied to this real dataset with this parametrization and strategy brought some weakly resolution to the final velocity model especially in the shallow part, but the final result does not show the same complexity of the real model. Discussion about the resolution issue is found later in this document.

2.9 Quality Control (QC)

The current inversion results have shown an improvement in the resolution and in the accuracy of the updated velocity model, at least for line 3 where the parameters for the inversion were optimized. The accuracy of the final velocity model was verified by conventional migrated images and common image gathers (CIGs) which can locally evaluate the velocity.

2.9.1 Seismic Images and CIGs

Figure 2.31 shows seismic images migrated with the initial and final velocity model, respectively. Both images were migrated using the pre-processed OBC dataset with RTM migration algorithm (25 Hz peak frequency). Basically, the images show the same stacking quality, with good continuity and focus of main horizons in the shallow part of the line above approximately 2.0 km. However, the final seismic image was improved in the deeper part of the section below 2.2 km depth which includes the reservoir zone of interest. The overall decrease of the velocity at that depth enhanced the horizons focus and continuity.
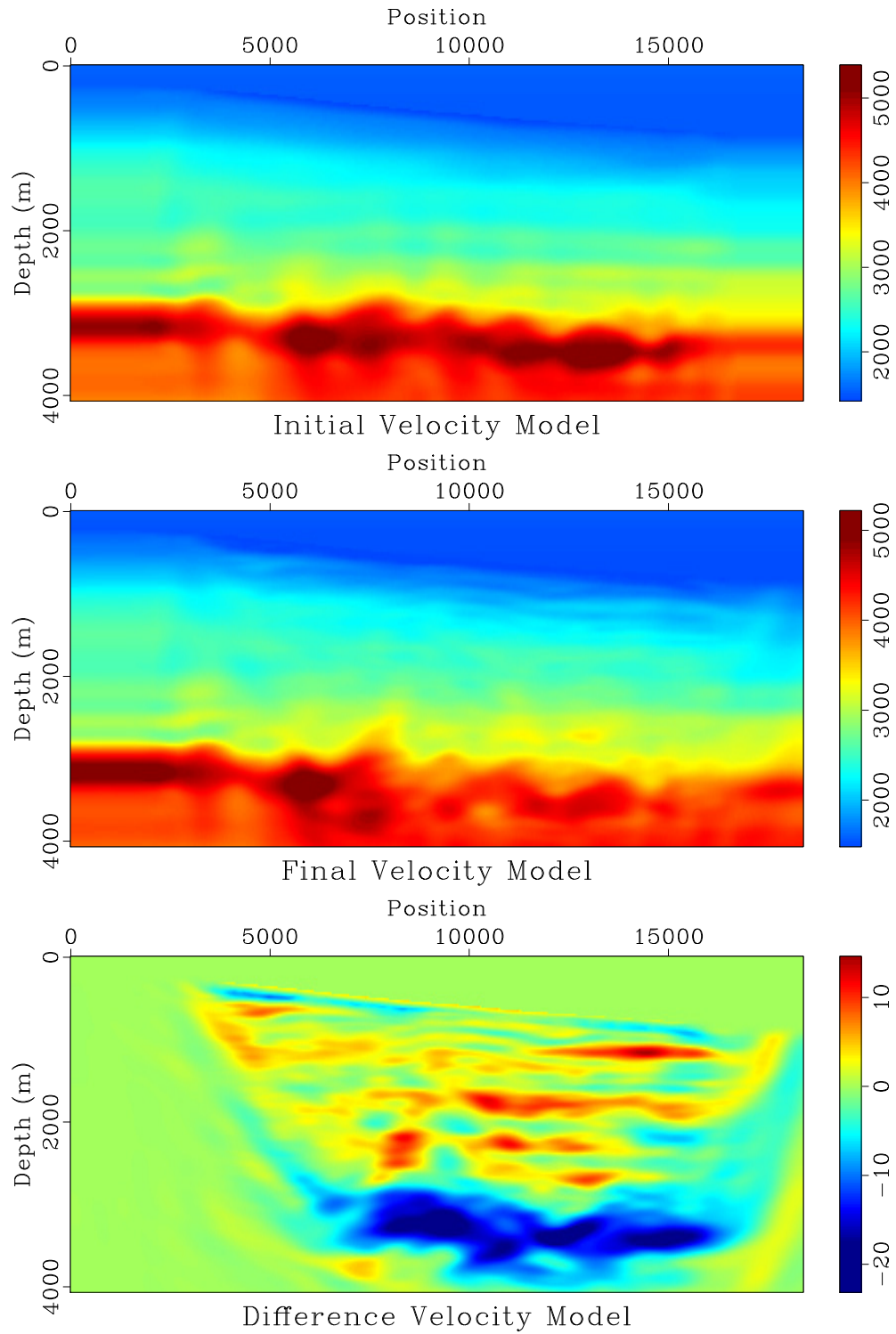
Figure 2.26: Intial velocity model (top), final velocity model (middle) and the percentage difference (bottom) showing the update after the waveform inversion for Line 3.
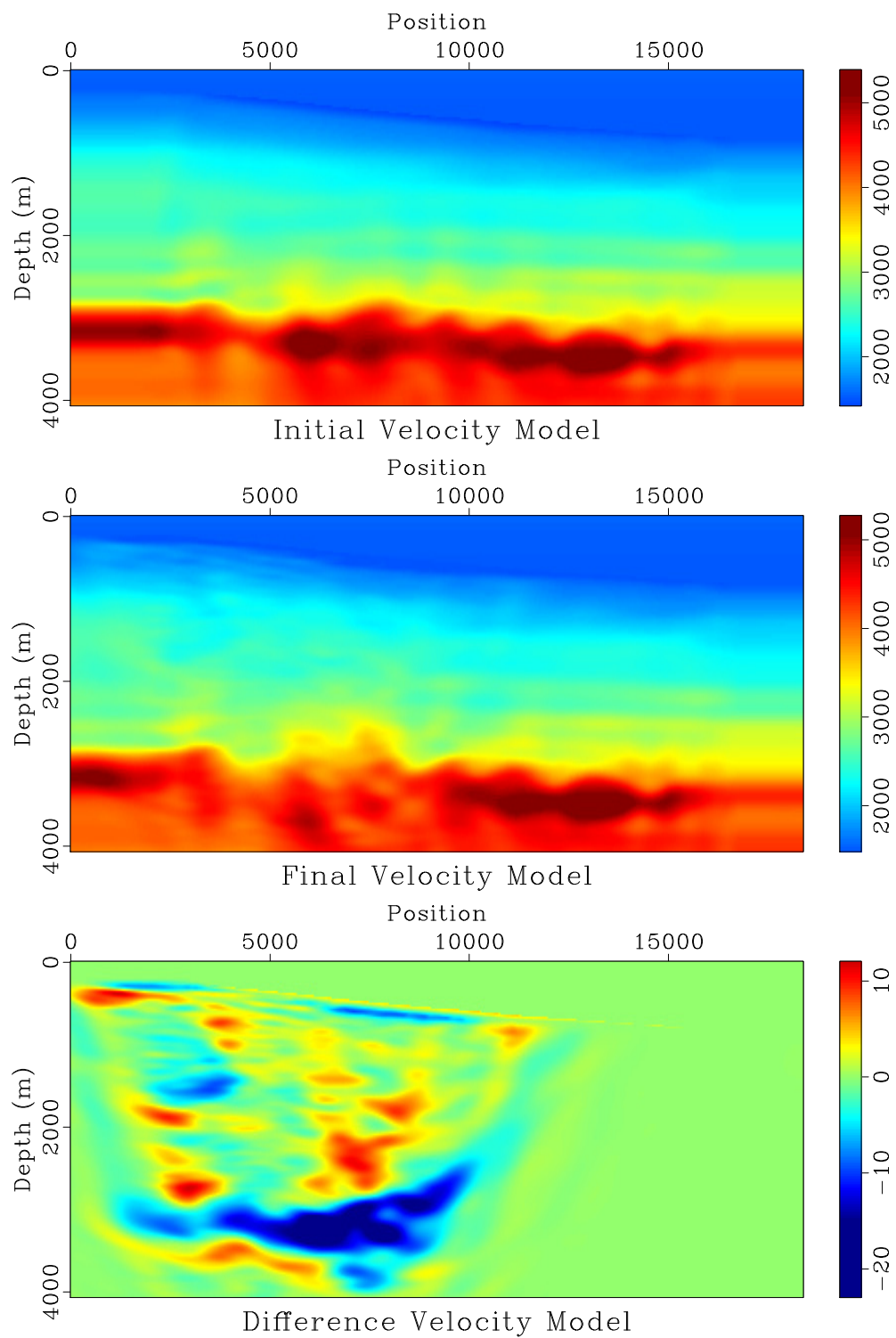
Figure 2.27: Intial velocity model (top), final velocity model (middle) and the percentage difference (bottom) showing the update after the waveform inversion for Line 1.
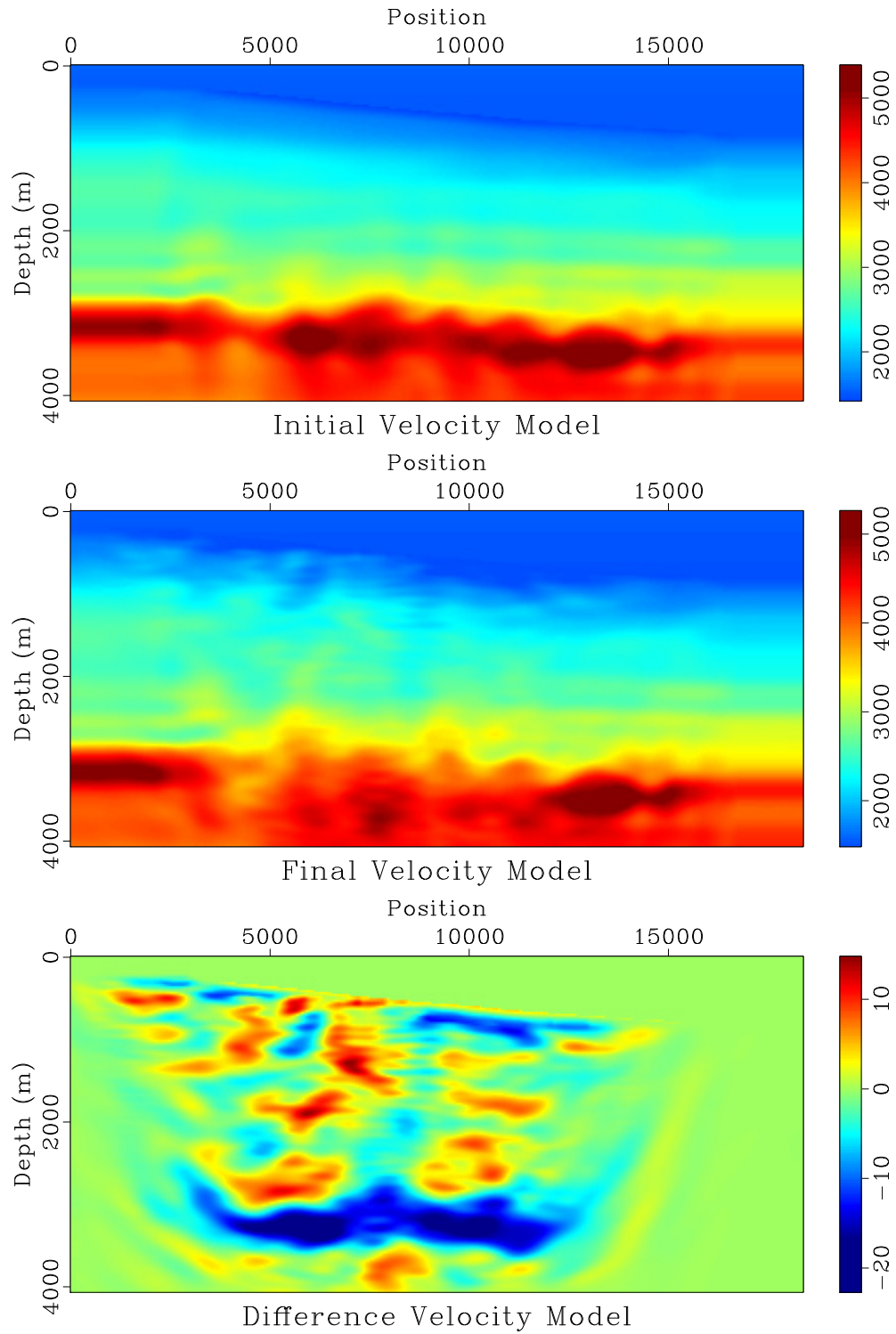
Figure 2.28: Intial velocity model (top), final velocity model (middle) and the percentage difference (bottom) showing the update after the waveform inversion for Line 2.
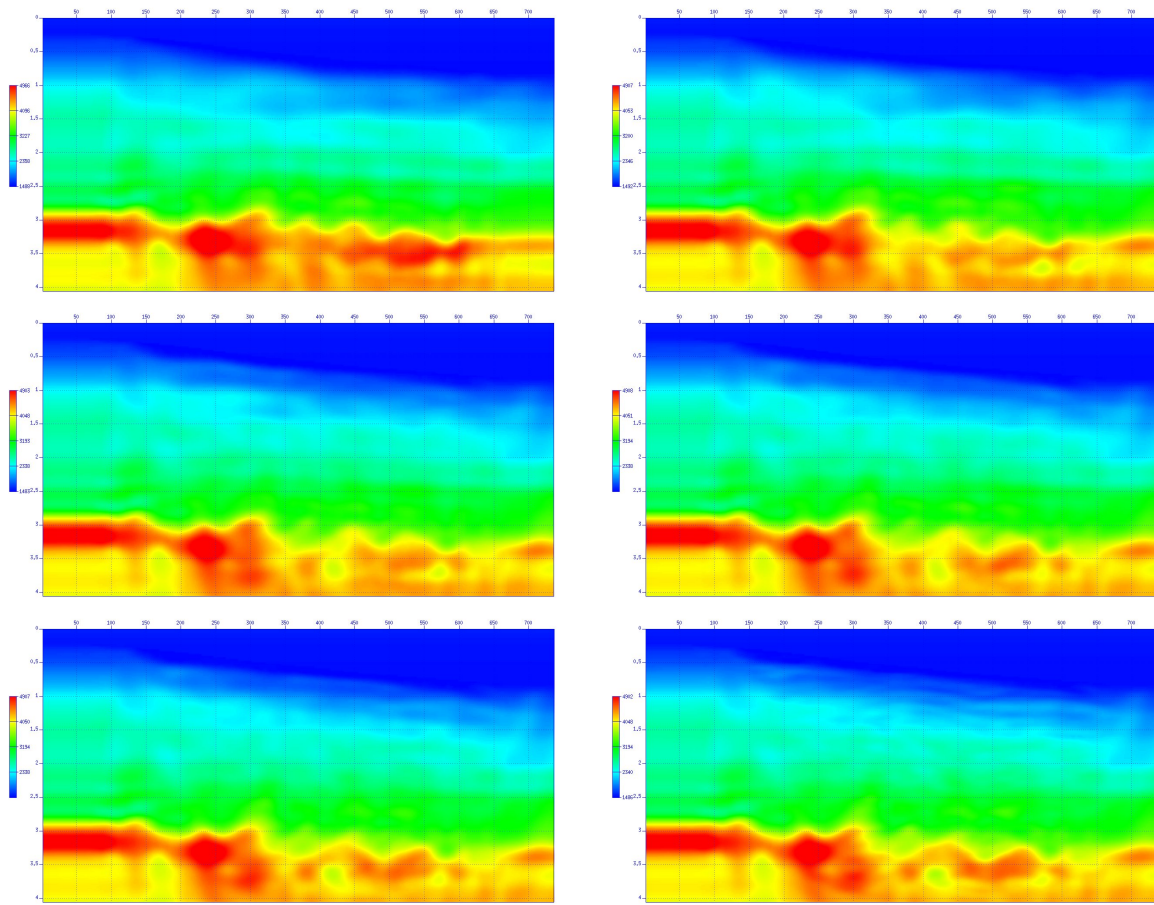
Figure 2.29: Velocity model updates after inversion of each group of frequencies (Line 3). From group 1 (top-left) to group 6 (bottom-right) it is recognizable that new information after each inversion is introduced in the velocity model.
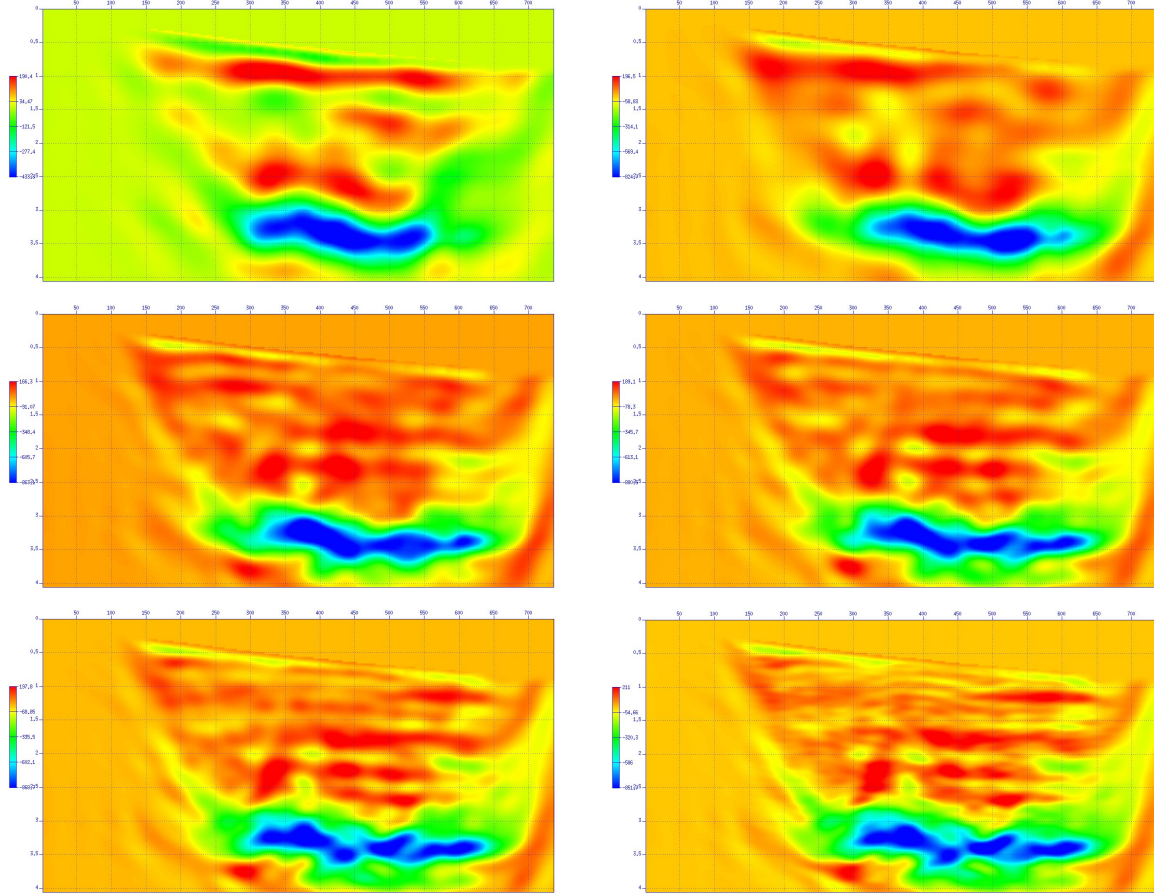
Figure 2.30: Velocity difference after inversion of each group of frequencies (Line 3). From group 1 (top-left) to group 6 (bottom-right) the update started with low wavenumbers, correcting the background velocity model, and gradually introduced information of higher wavenumber in the velocity model.

Figure 2.31: Seismic migrated images for line 3, with original velocity model (top) and final velocity model (bottom).
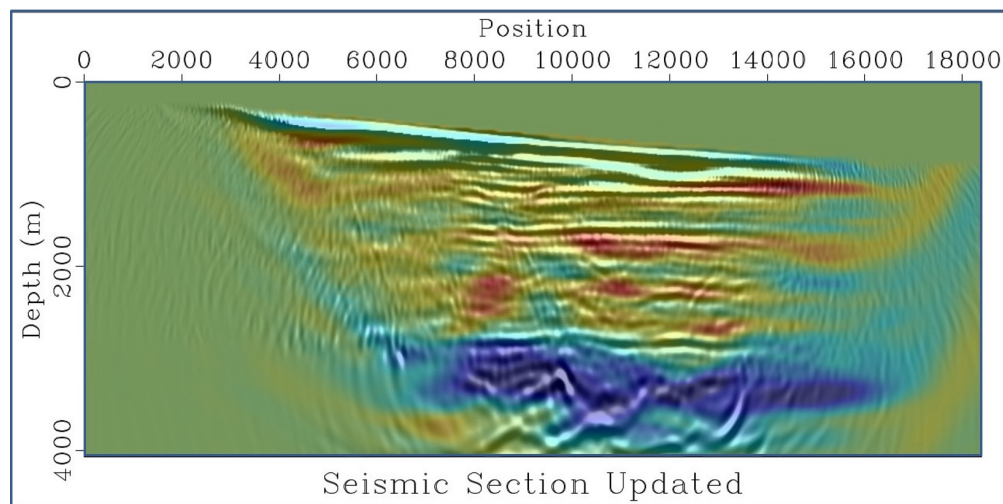
Figure 2.32: Migrated image of line 3 overlaid with the final velocity difference. Image is migrated using OBC field data without pre-processing and RTM algorithm with Mirror imaging technique (Grion et al., 2007).

Figure 2.32 shows the final seismic image and the velocity difference overlaid, where the larger velocity updates are related with the main horizons of the section. In addition, the velocity update shows the decrease of the resolution with depth, mostly limited by the survey design (poor illumination), the diving waves approach and the maximum inverted frequency (15 Hz).

The improvements identified in the line 3 migrated image are confirmed by the CIGs. Figure 2.33 shows the CIGs computed for both velocity models, initial (top) and final (bottom), at sparse locations (8.0, 8.5, 9.0, 9.5, 10.0, 10.5, 11.0, 11.5, 12.0 and 12.5) km in the seismic section. The CIGs show information about the accuracy of the velocity and about angle illumination. The comparison between initial and final CIGs reveals that the final CIGs are cleaner. In the shallow part, above 2.0 km, the CIGs are similar, although in the deeper part there are two main recognizable events at approximately 2.7 km and 3.5 km, where the updated velocity flattened the events. It indicates that velocity was corrected by the inversion, bringing greater accuracy to the velocity model. This accuracy is reflected in the seismic image through the focus and continuity of the horizons.

The largest updated obtained in the deeper part of the model, which brought a huge improvement in the seismic image, can be questionable. The ray tracing analisys show that only few rays traveled through the deeper part of the model, although the monochromatic wavefields in the Figure 2.10, Figure 2.11 and Figure 2.12 show a larger interaction at that depth. The analysis and the strategy rely that the diving waves are the most important source of information to this update, however, the selection of the data used in the inversion (time damping - $\tau = 4$ s) might not be completely efficient to avoid reflections. The inversion could have used reflections to update the deeper part of the model which can also be checked by the sensitivity kernel analisys (Figure 2.10, Figure 2.11 and Figure 2.12).

Corroborated by the original Petrobras imaging processing that have included the VTI symmetry, and assuming that the initial provided velocity model does not take it into account, the initial computed CIGs (Figure 2.33) show an seismic event at approximately 2.7

km depth with an anisotropic signature, called hockey stick. The seismic event is overcorrected, because of the lower vertical initial velocity compared with the correct velocity. In the final computed CIGs (Figure 2.33) the same seismic event appears more flattened, although it seems a bit undercorrected. Apparently the inversion was more influenced by the horizontal velocity, because it is focused in diving waves, which is greater than the correct velocity obtained by VTI imaging processing.

As mentioned, the waveform inversion for lines 1 and 2 were performed using directly the same parametrization of line 3. First, it was thought that this configuration would provide as good a result as the one obtained from line 3. However, as can be seen in Figure 2.25, lines 1 and 2 have shorter cable length, around 2.8 km, which provides an offset range much smaller than that of line 3 and the frequency discretization strategy would provide different frequencies to be inverted. Furthermore, part of the sources are located in the extended part of the velocity model, which is not reliable, because it was copied and extended from the last velocity profile of the original velocity model.

Despite the fact that the line 1 velocity model was updated by the inversion, the seismic migrated images and the CIGs don't show much change between the initial and final velocity model. Both, Figure 2.34 and Figure 2.36, show localized improvements, but also show deterioration of some seismic events. Inversion results for line 2 show the updated velocity model destroyed the deeper seismic events. The seismic migrated image lost focus and continuity, which also can be seen in the CIGs, where the events bend instead being flattened. Only the shallow part of both lines are preserved.

2.9.2 Comparison of Observed and Modeled Data

The inversion results can also be checked by comparing shots from the observed and the modeled data, which are generated using the initial and final velocity models. Figure 2.38 shows this comparison, where it is possible to recognize if the final modeled shot is more similar to the observed shot.
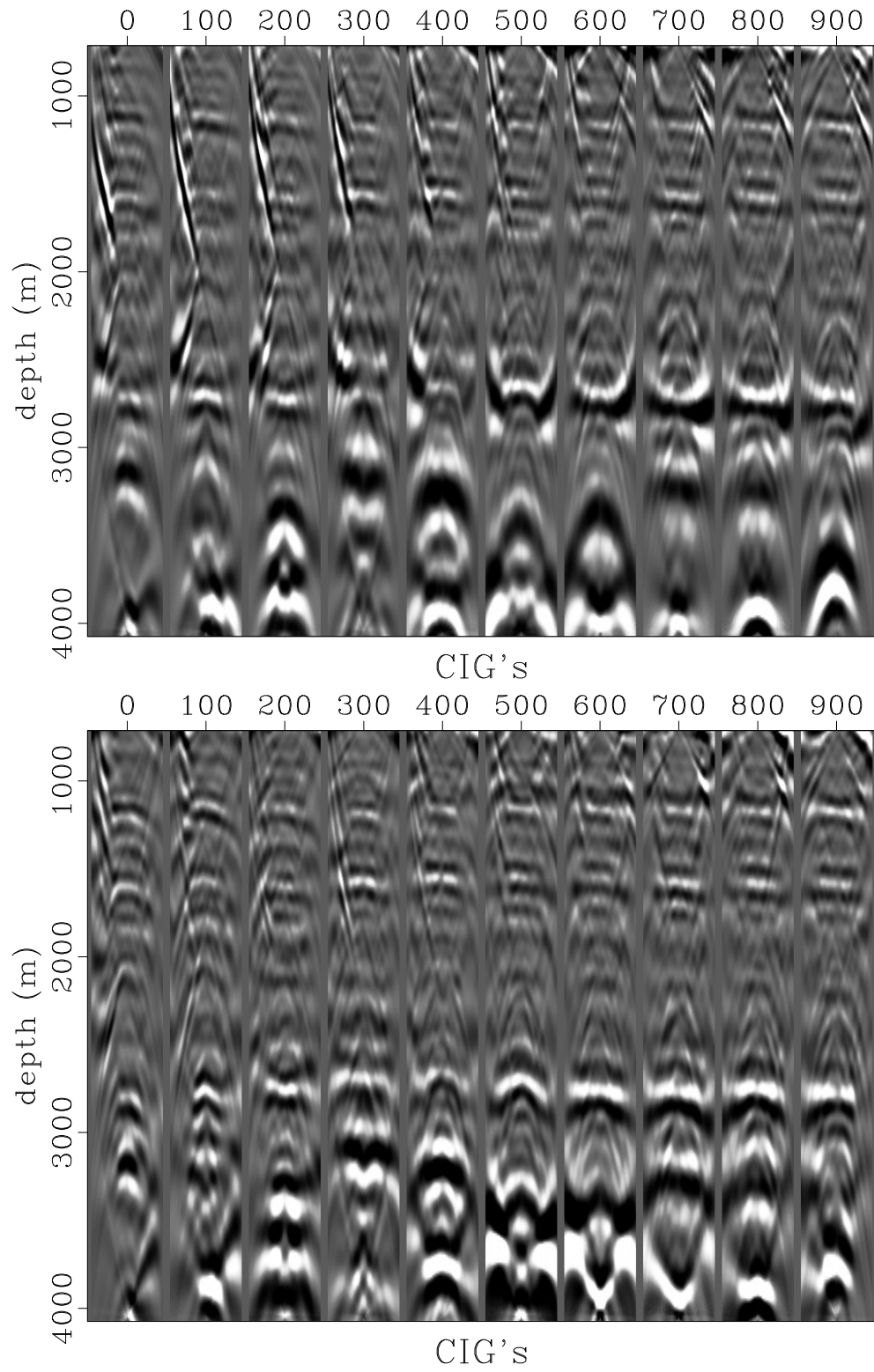
Figure 2.33: CIGs of line 3 computed from wavefields of original (top) and final (bottom) velocity models at fixed positions (8.0, 8.5, 9.0, 9.5, 10.0, 10.5, 11.0, 11.5, 12.0 and 12.5)km.
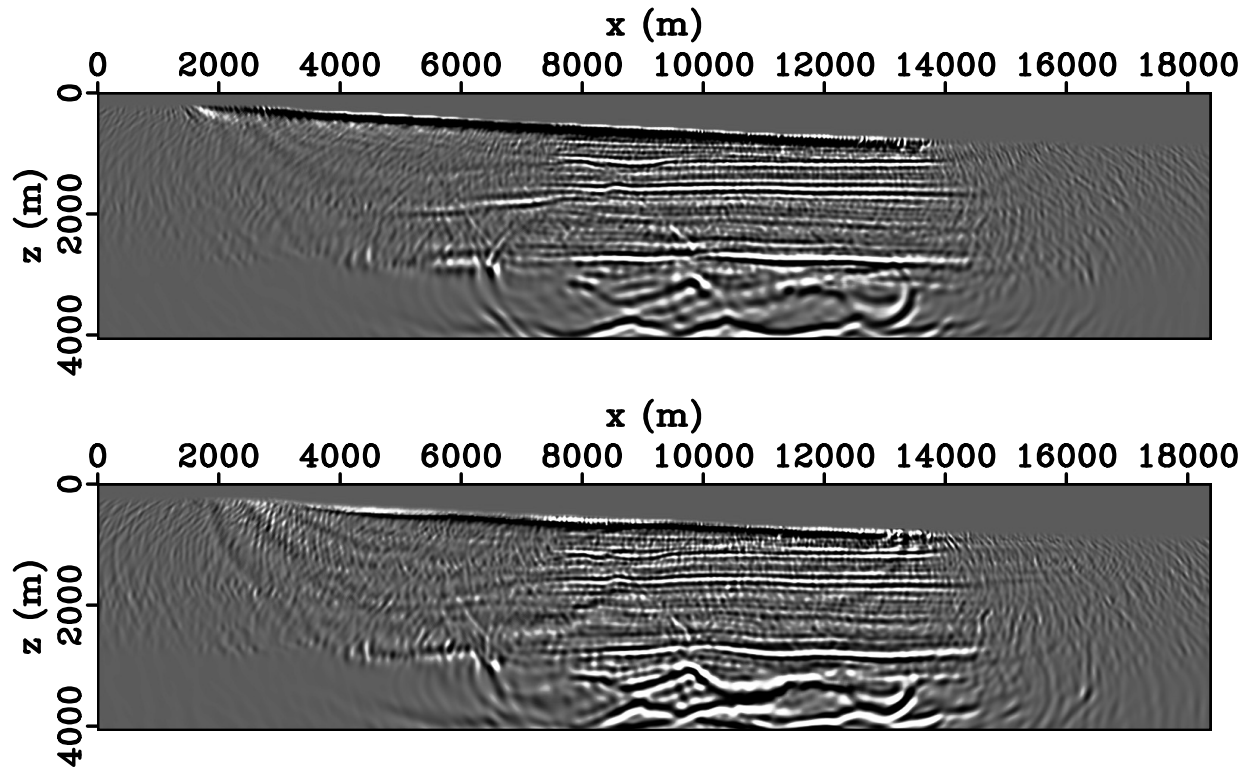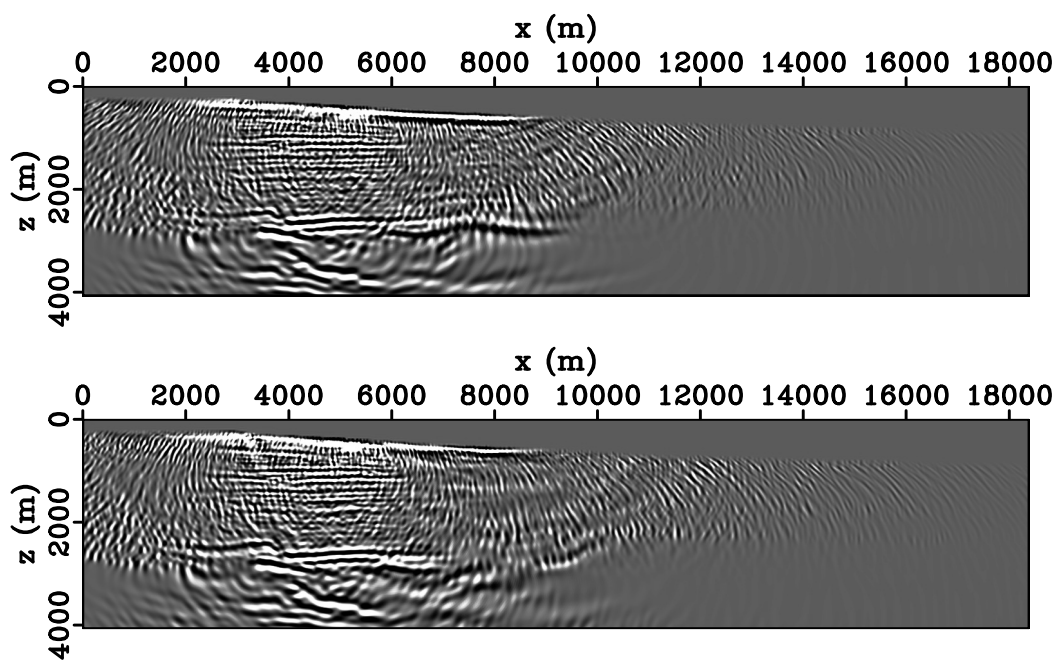
Figure 2.34: Seismic migrated images for line 1, with original velocity model (top) and final velocity model (bottom).
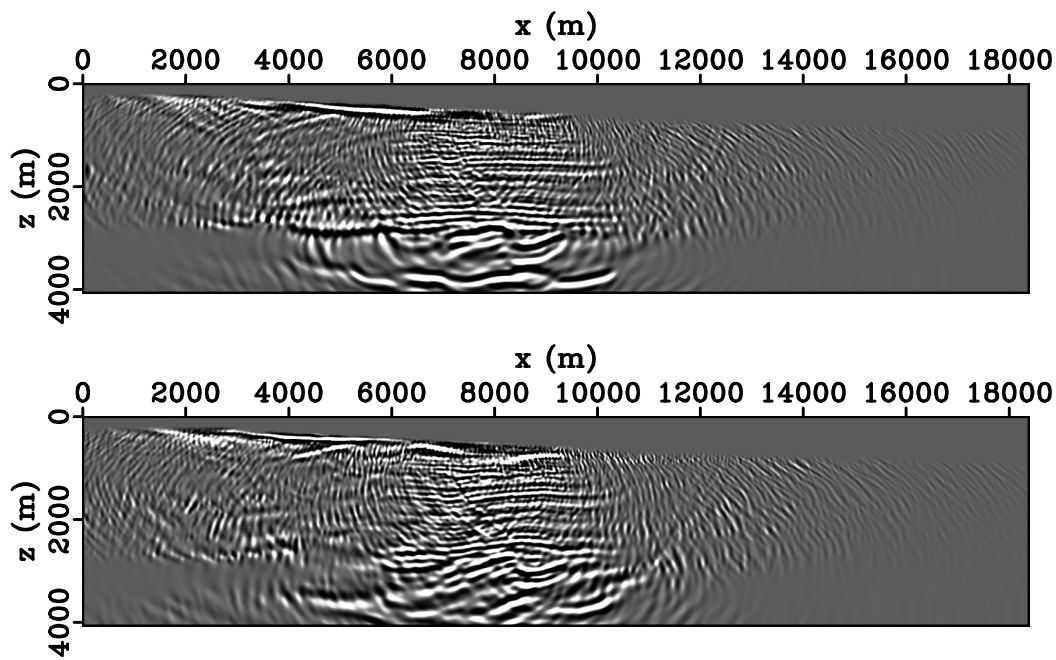
Figure 2.35: Seismic migrated images for line 2, with original velocity model (top) and final velocity model (bottom).
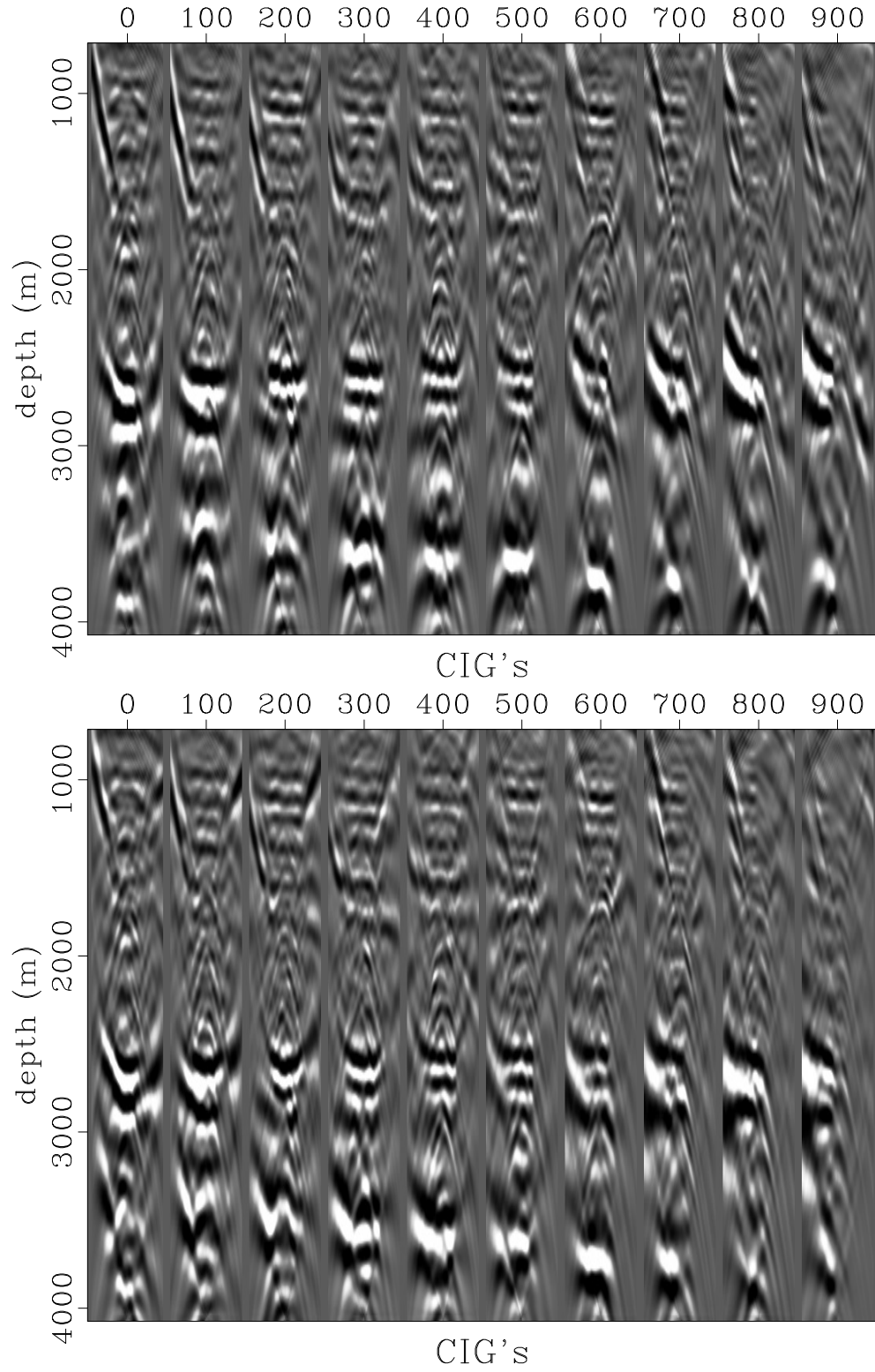
Figure 2.36: CIGs of line 1 computed from wavefields of original (top) and final (bottom) velocity models at fixed positions (4.0, 4.5, 5.0, 5.5, 6.0, 6.5, 7.0, 7.5, 8.0 and 8.5)km.
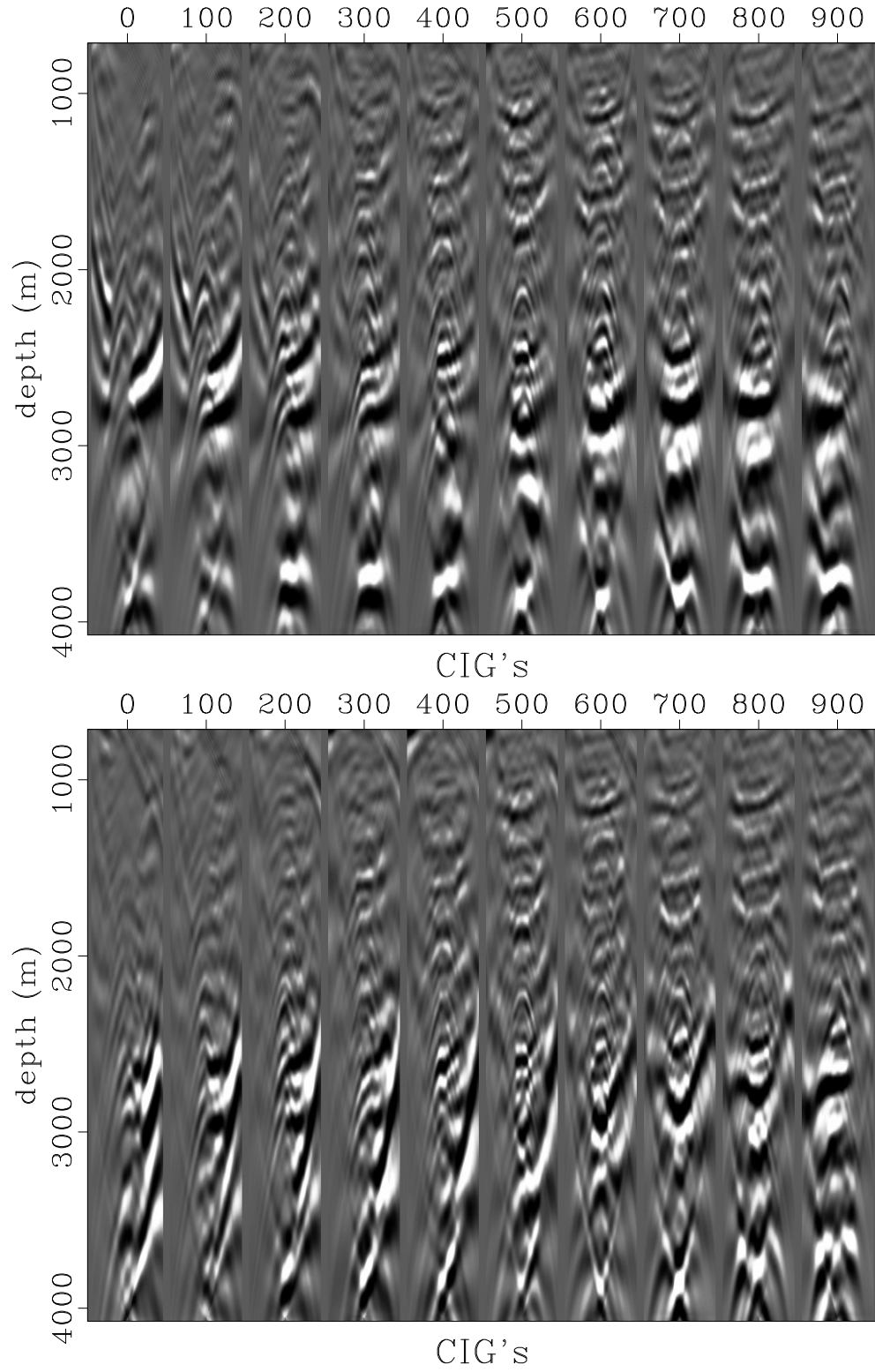
Figure 2.37: CIGs of line 2 computed from wavefields of original (top) and final (bottom) velocity models at fixed positions (6.0, 6.5, 7.0, 7.5, 8.0, 8.5, 9.0, 9.5, 10.0 and 10.5)km.

By the image, we recognize that the first breaks are well matched and there are some reflections brought by the inversion, when comparing with the initial modeled shot. These reflections have a really small amplitude and the final modeled shot is still far from to represent the same complexity shown by the observed data. The inversion was able to bring some resolution especially in the shallow part. The resolution of the final velocity model will be discussed further.
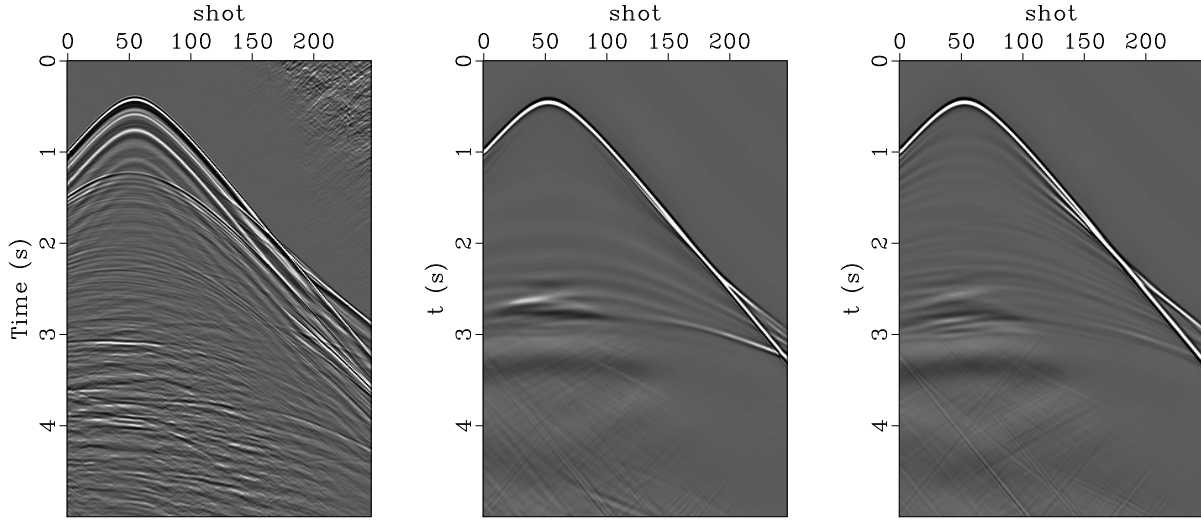
Figure 2.38: Comparison of observed shot, initial modeled shot and final modeled shot.

2.9.3 Phase Residuals Comparison

During the inversion process, since the phase residuals are used to improve the velocity model, it is a good procedure to verify if the phase residuals are decreasing after the inversion of each group of frequencies. Figure 2.39 shows phase residual panels for two different frequencies, f=2.6Hz (top) and f=3.9Hz (bottom), where on the left column are the phase residuals computed in the first iteration and on the right in the last iteration. When comparing both panels for each frequency it is possible to identify that overall the differences decrease and the larger improvements occur at near offset.
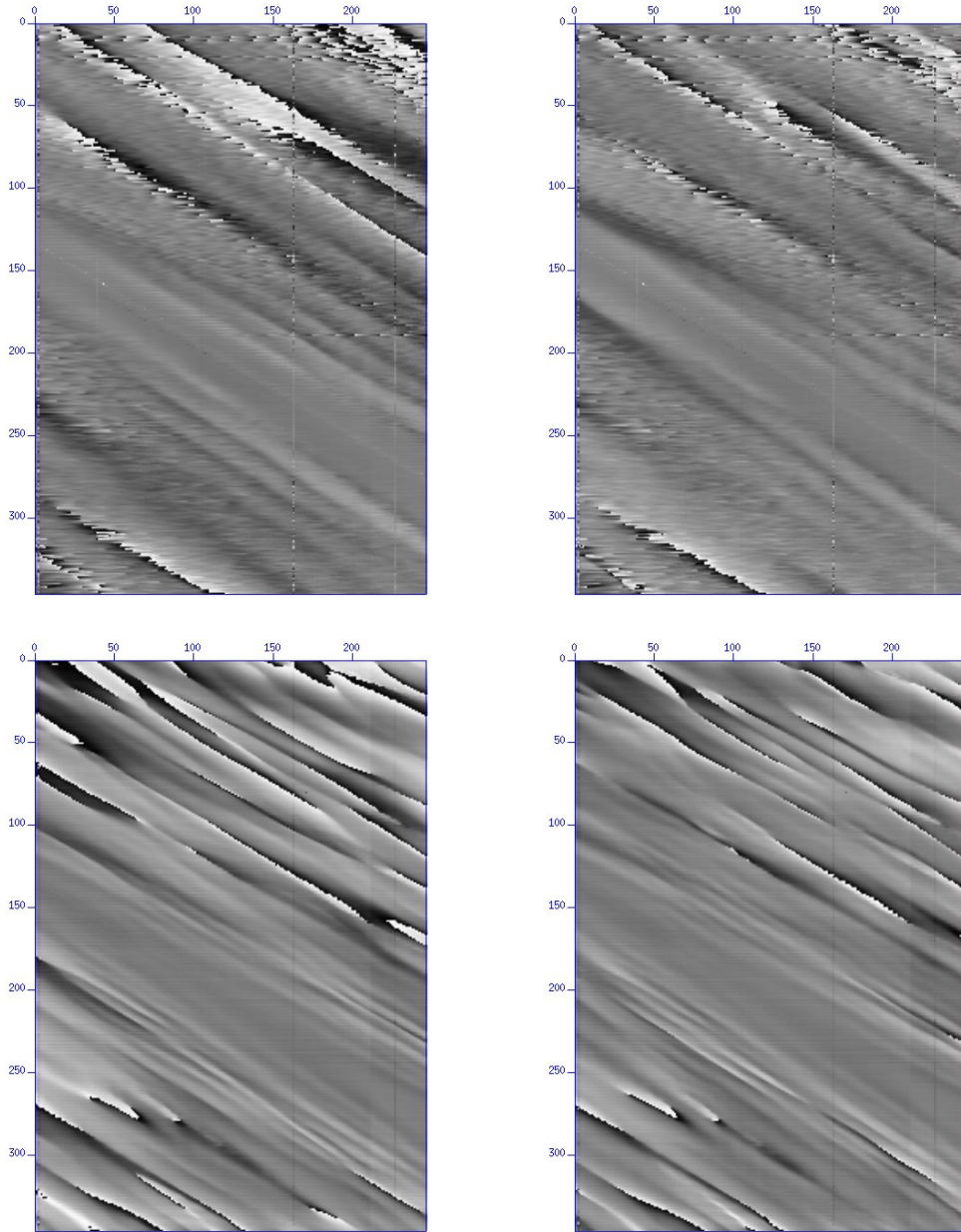
Figure 2.39: Phase residuals for f=2.6Hz (top) and f=3.9hz (bottom). Panels on the left are the phase difference computed in the first iteration and on the right the last iteration.

2.9.4   Well Logs Velocity Profile Comparison

Figure 2.3 shows that close to the 2D line are several well logs, some of them are vertical and closer to the studied line. Three of them were chose in order to compare locally its

velocity profile with the initial and final velocity models. Figure 2.40, Figure 2.41 and Figure 2.42 show each of these well log profiles, which were filtered in order to be comparable with the lower frequency content of the velocity models. As can be seen, the well logs provide information only in a restricted depth range of interest, which is zoomed in to better examine the details. All images show the same behavior, where the initial and final velocity model follows the well log trend, although with much lower frequency content. When comparing the initial and final velocity model, we recognize the trend showed by the velocity difference, where at the intermediate depth (above 2.0km) the velocity has increased and at larger depth velocity decreases. Once more, we realized that the inversion process has not brought high resolution to the final velocity model.
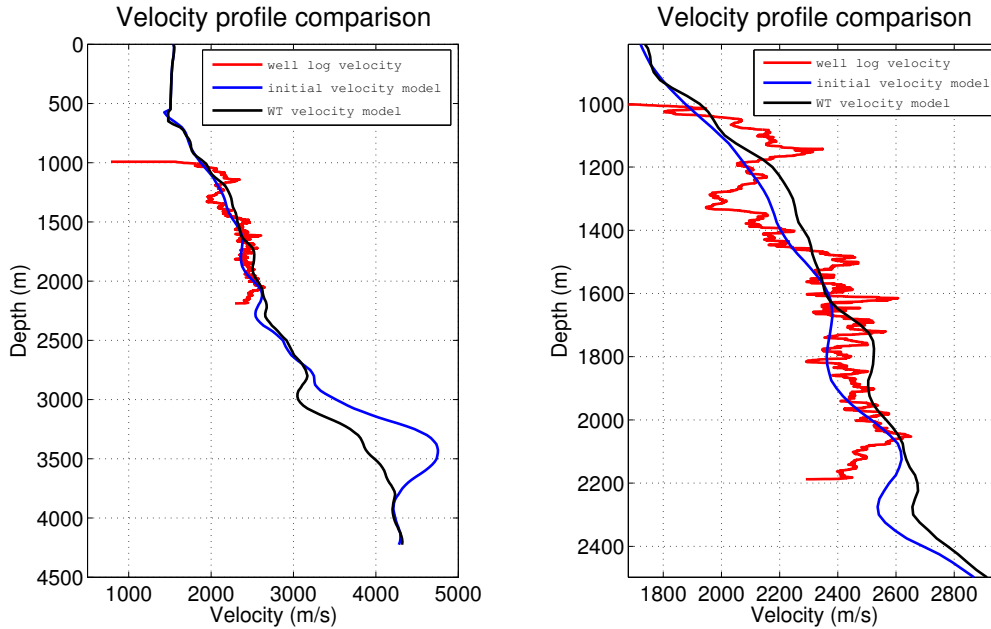
Figure 2.40: Velocity profiles from well log 1 (red), initial (blue) and final (black) velocity model. Well log 1 is 130m far from the line. The right panel is a zoom in around well profile.
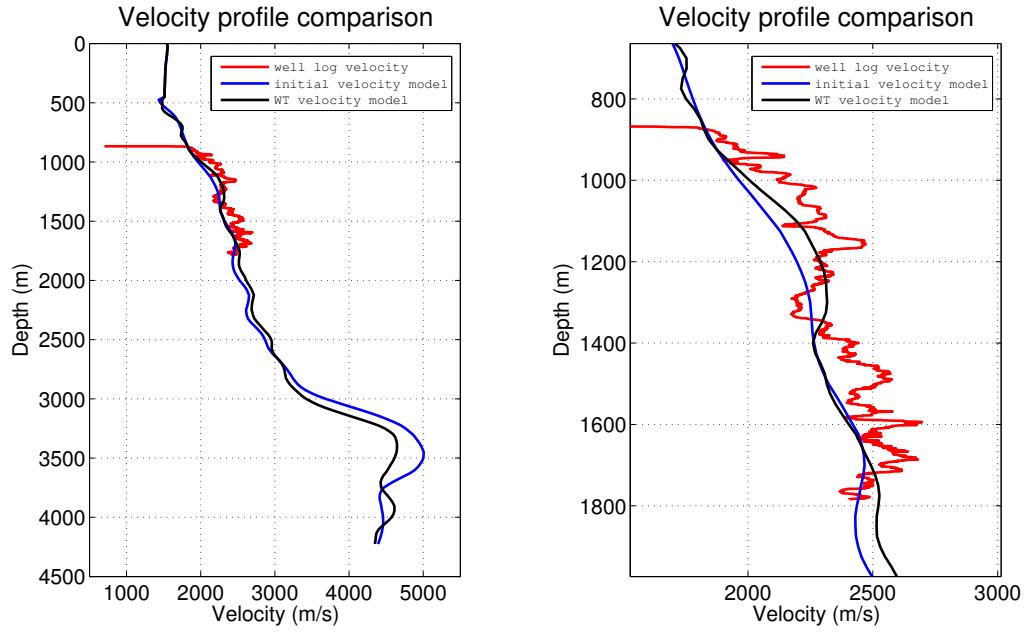
Figure 2.41: Velocity profiles from well log 2 (red), initial (blue) and final (black) velocity model. Well log 2 is 300m far from the line. The right panel is a zoom in around well profile.
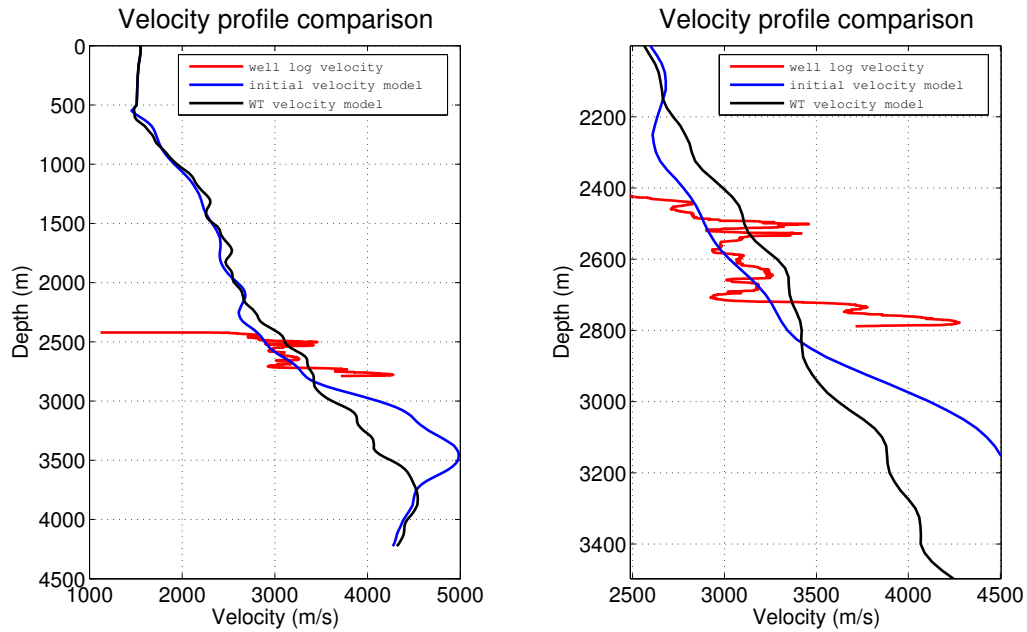
Figure 2.42: Velocity profiles from well log 3 (red), initial (blue) and final (black) velocity model. Well log 3 is 1000m far from the line. The right panel is a zoom in around well profile.

2.9.5 Source Signature QC

The source signature extraction is performed with the initial velocity model, and after each group of frequencies inversion. Figure 2.43 shows the source signature map (all shots) on the left and the average source signature used for inversion on the right. The source signature is computed after each group of frequencies is inverted, because it is updated by the velocity model changes. A good QC is to check if the source map shows consistency throughout all the shots, as can be seen in Figure 2.43. In addition, according to the top image, the initial velocity model is accurate enough to be used in the initial inversions. Both images, the initial and final source signature map, are consistent and does not show significant difference, except the amplitude of the average source signature increases in the final model. Usually, when the initial velocity model is not good enough, we can realize its improvement by the consistency of the source signature map.

2.9.6 Wavenumber Analysis

The scattering wavenumber ($\mathbf{k}$) can be expressed as a function of frequency (f) and the scattering angle (θ) as shown in Equation 2.3. Here, we evaluate the wavenumber content in the final velocity model and compare it with the maximum theoretical wavenumber for $\theta=0^o$ and maximum frequency, which means normal incident reflections (Virieux and Operto, 2009). Figure 2.44 shows the computed vertical wavenumbers for three different velocity profiles (linear: from 1.5 km/s to 5.0 km/s (red dashed); initial velocity model (blue); and final velocity model (black)) and two frequencies (f_{min}=2 Hz and f_{max}=15 Hz). The plot is separated in two boundaries defined by the frequency, the lower bound is related with 2 Hz and the upper bound with 15 Hz, where each curve describe the maximum wavenumber at that depth and for that velocity. The red rectangle in the lower bound represents the wavenumber amplitude spectrum of the final velocity model (Figure 2.45 (left)), which shows that waveform inversion was not able to bring higher resolution to the final velocity model. High resolution would move the wavenumber amplitude spectrum (red rectangle) towards
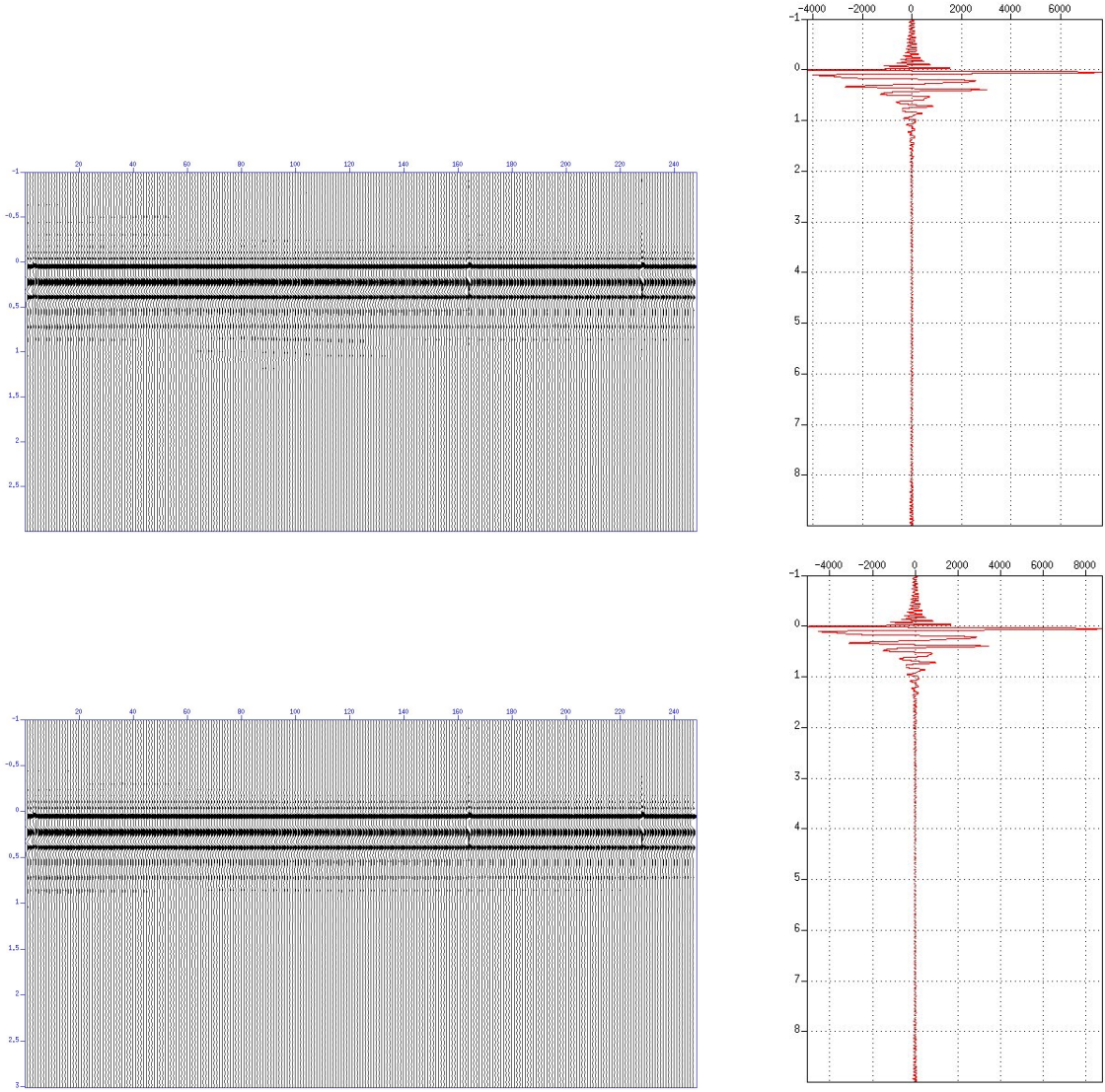
Figure 2.43: Source signature map (left) and the average source signature (right) computed from the initial velocity model (top) and the final velocity model (bottom).

the upper bound, which would be theoretically possible for 15Hz. Figure 2.45 also shows the wavenumber amplitude spectrum for the velocity difference, which has a really small amplitude spectrum when compared with the background spectrum.

$$\mathbf{k} = \frac{2f}{c_o} \cos\left(\frac{\theta}{2}\right) \mathbf{n} \tag{2.3}$$
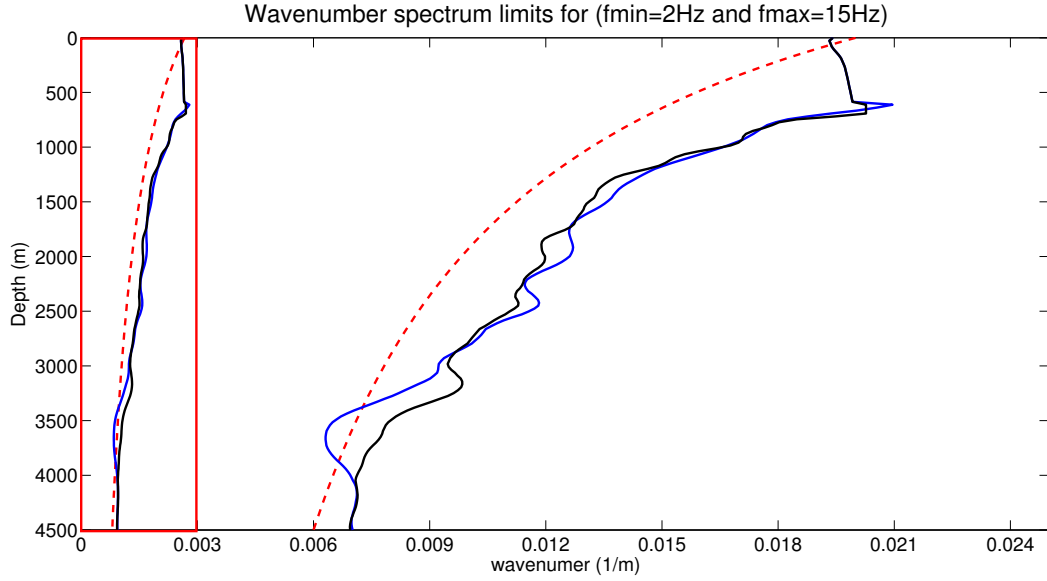
Figure 2.44: Maximum vertical wavenumber for f_{min}=2Hz and f_{max}=15Hz for three different velocity profiles: linear velocity model (dashed red); initial velocity model profile (blue) and final velocity model profile (black).
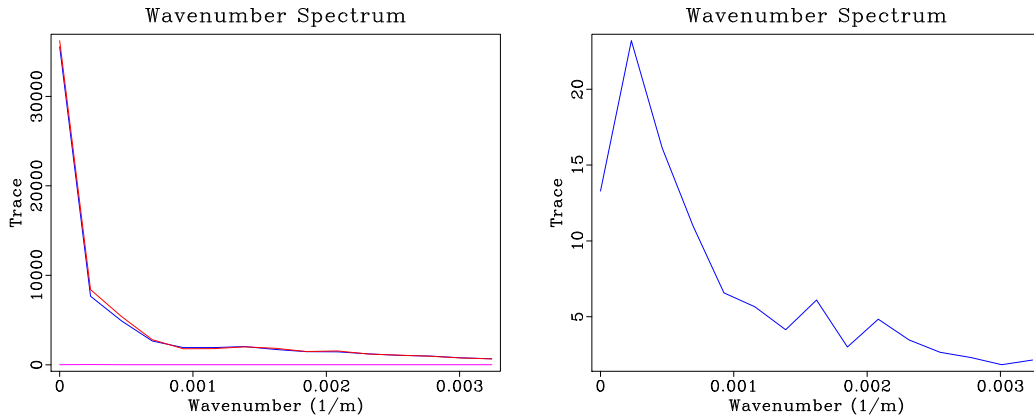
Figure 2.45: Wavenumber amplitude spectrum of the initial and final velocity model and the velocity difference (left) and only for velocity difference (right).

2.10   Conclusions and Analysis

The waveform inversion results obtained for the OBC Campos dataset (line 3) have shown improvements in the final velocity model. The final migrated image and the CIGs show that the final velocity model is more accurate, when the inversion corrected the background

velocity generating more continuous and focused horizons at the depth of interest (reservoir depth). The new velocity model may be used in acoustic/elastic attributes inversion where it is crucial to incorporate a more reliable velocity information which will better constrain the results. Wavenumber content analysis was showed that the initial and final velocity model wavenumber contents are almost the same, although it is recognizable that some resolution enhancement appears especially in the shallow part of the model (Figure 2.26).

Much can be speculated about the causes of this failure, perhaps the strategy used to perform the waveform inversion was wrong. We could have used time domain damping relaxing strategy to help select the data that is included in the inversion. First, starting the inversion with a stronger time damping to fix the background velocity, and slowly relaxing the time damping parameter allowing the reflections to be included in the inversion to bring the expected resolution.

It is also possible to use the previously mentioned approach (time damping relaxing strategy), although including the amplitude of the data in the objective function in the later inversions. This type of amplitude/phase objective function works perfectly in synthetic data, however, requires an amplitude match procedure between observed data and modeled data. Only tests can prove whether or not these changes will produce the expected high resolution velocity model.

The inversion results for lines 1 and 2 are inferior when compared with line 3 results, as discussed before, several possible problems could have impacted the final results.

CHAPTER 3

EVALUATION OF AN OPTIMUM MINIMUM OFFSET

Sensitivity of diving waves is an important parameter to help the inversion to update the background velocity model. Large offsets record diving waves that have deep penetration and it should be used when the imaging target is deep. Waveform inversion usually requires a minimum offset that has to be 4-6 times that of the target depth. The data used in Chapter 2 has a cable length 6 km (line 3) resulting in an offset range of 3.0 km to 12.1 km, which is not able to adequately illuminate the deeper portions of the subsurface (poor illumination). The objective of this section is to estimate an optimum minimum offset, in the 2D sense, for a future survey where waveform inversion can successfully reconstruct a high resolution velocity model at the reservoir depth.

To determine this minimum offset parameters, synthetic OBC seismic data are generated using a synthetic velocity model of the Campos Basin. The acquisition design used to generate the synthetic data has a larger number of receivers (OBC cable length) and sources which provide much larger offsets and deeper illumination when compared with the field data. Waveform inversion was performed with two different strategies and two different initial velocity models, first to check the recovered resolution in the model and later, to evaluate the impact of each strategy and the use of a different initial velocity model in the final results.

3.1 Synthetic Model - velocity and data

In order to create a reliable velocity model of the Campos Basin field, the synthetic velocity model was built based on three inputs of this area:

- the initial velocity model used in all previous inversions (Figure 2.8),

- on the well log 1 (Figure 2.40), which has velocity information in a limited depth range, and

- seven interpreted horizons from a migrated seismic image (Figure 2.31) to guide the lateral extrapolation.

The final synthetic velocity model is shown in Figure 3.1, and it is similar to the real velocity model of the subsurface, at least until the top of the high velocity layer (carbonate/salt), just below the reservoir.
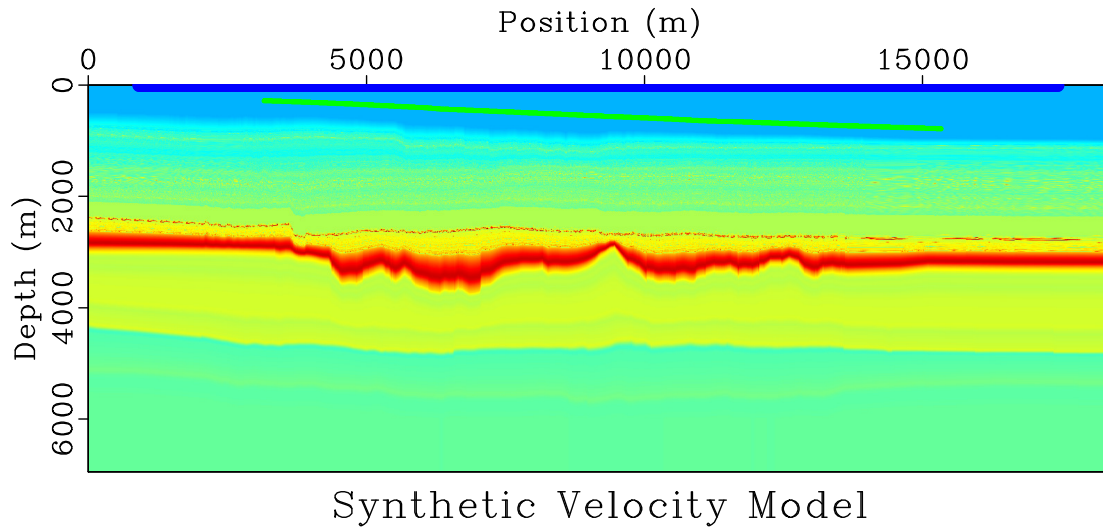
Figure 3.1: Synthetic velocity model used to generate the synthetic OBC seismic data.

Figure 3.1 also shows the source (blue) and the receiver (green) positions. The source and receiver intervals were kept the same as the field data acquisition (43.75 m and 25 m, respectively). The number of sources and receivers are given in Table 3.1 in addition to the coordinates of the first source and receiver. The acquisition was designed to span the entire 2D velocity model, however, the waveform inversion code requires 20 cells distance from both edges to avoid edge effects.

Table 3.1: Number of sources/receivers and the first coordinate of sources and receivers for the synthetic line.

	# sources	# receivers	first source coordinate (m)	first receiver coordinate (m)
line	380	488	901	3163

The data were generated under the acoustic isotropic assumption using the *sfawefd* function (Madagascar open-source package), which is a time domain finite difference modeling, with the source wavelet peak frequency of 12 Hz. Figure 3.2 shows the source wavelet in time domain and the amplitude spectrum of the data, which contains sufficient amplitude at 15 Hz, the maximum inverted frequency in the inversions. Figure 3.3 shows an example of shots generated by the acoustic forward modeling. These data are input into the waveform inversion process.
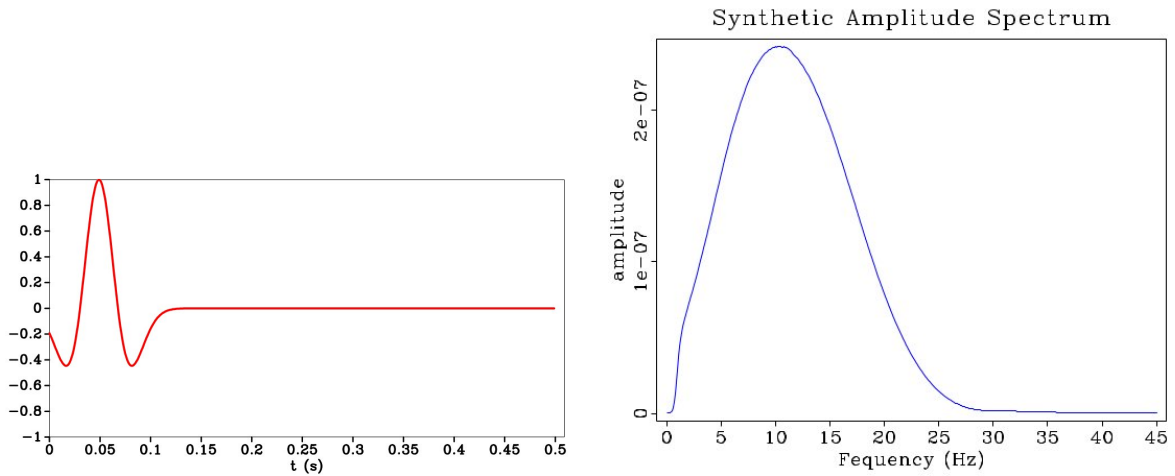
Figure 3.2: Source wavelet used to generate the synthetic data for inversion and the amplitude spectrum of the synthetic data.
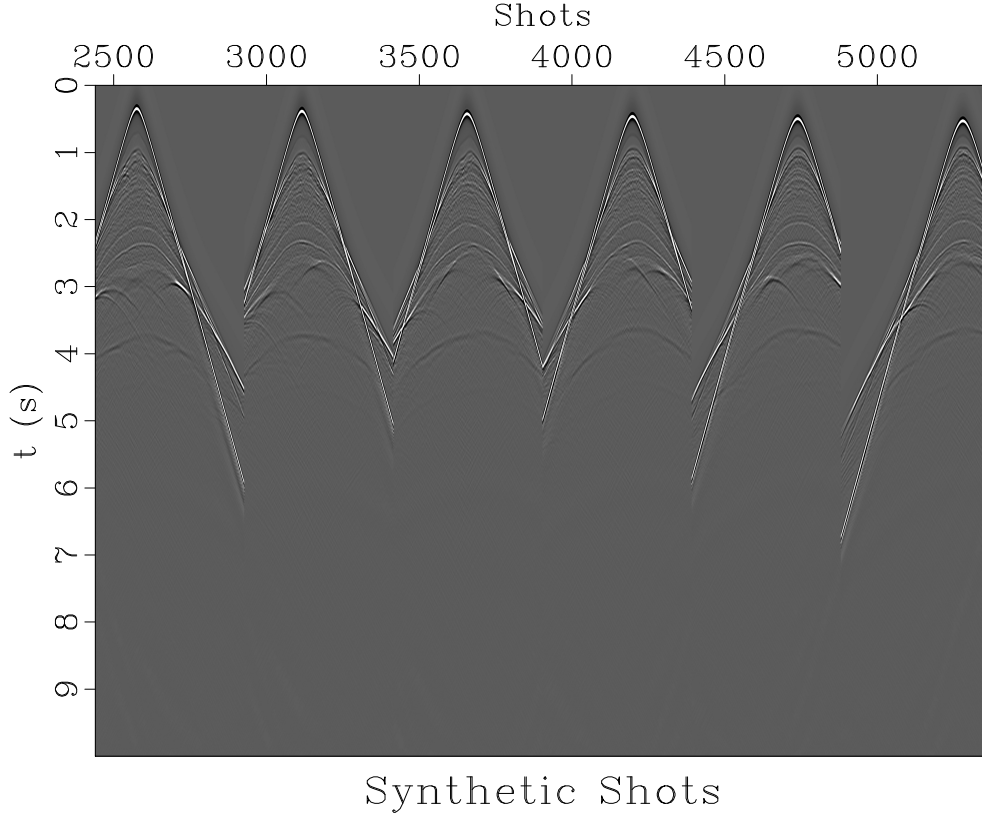
Figure 3.3: Shots examples of the synthetic data.

3.2 Waveform Tomography Strategies

Two different strategies were used in the Campos Basin synthetic data to perform wave-form tomography by varying two parameters – the time domain damping and the type of objective function. As described in Chapter 2, time damping is a useful tool to select the data to be included in the inversions. Both strategies used three levels of time domain damping (τ = 1, 2 and 4 s) and they will be called strategy 1 and strategy 2. First, starting the inversion with a stronger time damping $\tau = 1$ s helps fix the background velocity, and later relaxing the time damping parameter to $\tau = 2$ s and $\tau = 4$ s, will include reflections in order to bring resolution. The choice of the type of objective function is the main difference between these strategies. In the later inversions, where time damping is $\tau = 4$ s, strategy 1 uses a combined objective function based on amplitude and phase residuals. The inclusion of the

61

amplitude residuals in this inversion would not be a problem, since the synthetic data does not include amplitude variations. The selected frequencies to be inverted are the same as the ones used in the field data, based on the frequency discretization strategy. However, only one frequency (selected frequency) is required to be inverted, without needing to build groups of frequencies in order to suppress any noise influence. The two strategies are described in Table 3.2 and Table 3.3.

This section also includes an inversion test to verify the impact of two different initial velocity models in the final result. Figure 3.4 shows three velocity models – the reduced true velocity model with maximum depth of 4.08 km (top), the initial velocity model 1, which is a smoothed version of the true velocity model (middle), and the initial velocity model 2, which is the initial velocity model provided by Petrobras and obtained by MVA (bottom). There are subtle differences between both initial velocity models, but the one obtained by MVA is more detailed (compare the initial modeled shots in Figure 3.8 and Figure 3.9) and its deeper part is not as resolved as the smoothed version. The velocity models for the synthetic inversion has the same physical and grid size as the one used in the field data inversion.

Using two strategies (strategy 1 and strategy 2) and two initial velocity models (initial velocity model 1 and initial velocity model 2) three different waveform inversions were performed on the synthetic data, which are described in Table 3.4.

Table 3.2: Waveform inversion strategy 1: objective function; time domain damping; frequecies.

objective function	time domain damping	f_1	f_2	f_3	f_4	f_5	f_6	f_7
phase	$\tau = 1s$	2.0	2.6	3.8	-	-	-	-
phase	$\tau = 2s$	2.0	2.6	3.8	5.4	7.8	11.0	15.0
amplitude/phase	$\tau = 4s$	2.0	2.6	3.8	5.4	7.8	11.0	15.0

Table 3.3: Waveform inversion strategy 2: objective function; time domain damping; freque-cies.

objective function	time domain damping	f_1	f_2	f_3	f_4	f_5	f_6	f_7
phase	$\tau = 1s$	2.0	2.6	3.8	-	-	-	-
phase	$\tau = 2s$	2.0	2.6	3.8	5.4	7.8	11.0	15.0
phase	$\tau = 4s$	2.0	2.6	3.8	5.4	7.8	11.0	15.0

Table 3.4: Description of the three different waveform inversions performed in the synthetic data.

name	strategy 1	strategy 2	initial model 1	initial model 2
inversion 1	X	-	X	-
inversion 2	X	-	-	X
inversion 3	-	X	-	X

3.3 Inversion Results

The three waveform inversion results are shown in Figure 3.5, Figure 3.6, and Figure 3.7, respectively. All inversions have shown some improvements when compared with each initial velocity model, however, the best result was obtained through inversion 1. The final velocity model and the velocity difference (Figure 3.5) show that the updated velocity model has a higher resolution than the initial velocity, particularly in the shallower portions. The resolution is improved throughout the entire model and reaches the depth of the reservoir, our main objective. Also, the inversion has recovered almost perfectly the higher velocity layer located at approximately 3.0 km depth.

Figure 3.6 shows the results for inversion 2. Again, the final velocity model and the velocity difference show that the inversion brought higher resolution update to the entire model. The top and the thickness of the high velocity layer are well defined, although the velocity below the high velocity layer is still larger than the true velocity, because of the initial velocity model trend. The inversion 1 and inversion 2 results are comparable up to the depth of interest, which includes the high velocity layer.

In contrast, the results for inversion 3 are not satisfactory and do not provide the same resolutions as do inversions 1 and 2. The overall update is within the same wavenumber content of the background velocity model, and is quite similar to the field data results presented in chapter 2. There is no resolution enhancement in the shallow part and the entire model looks noisy, because of the relaxed wavenumber filter applied to the gradient in order to recover higher resolution through the inversions. One possible explanation is the fact that the objective function is based on phase residuals only, however, it is shown that this type of approach can yield high resolution results (Bednar et al., 2007). This fact may explain the limitation of the field data results (chapter 2) and suggest the use of amplitude residuals in the objective function, although in field data some type of matching amplitude process between observed and modeled data needs to be applied. For example, Pratt (2013) computes correction factors by comparing the amplitude of the modeled data obtained with the initial velocity model with the amplitude of the observed data.

3.4   Quality Control (QC)

The final inversion results have shown an improvement in the resolution of the updated velocity model, especially for inversions 1 and 2. These results can also be checked by comparing the similarity of the modeled data generated by the final and initial velocity models, and the "observed" data generated for the true model. Since we are dealing with synthetic models, the velocity profiles can be directly checked with the true velocity model.

3.4.1   Comparison of Observed and Modeled Data

Figure 3.8, Figure 3.9, and Figure 3.10 show the modeled shot (final and initial model) and the observed shot, for the three inversions, respectively, at a fixed position (x,z)=(9518,5)m. First, note that the initial velocity model 2 is more detailed than velocity model 1, comparing both initial modeled shot, the MVA velocity model is able to generate some reflections in the modeled shot.
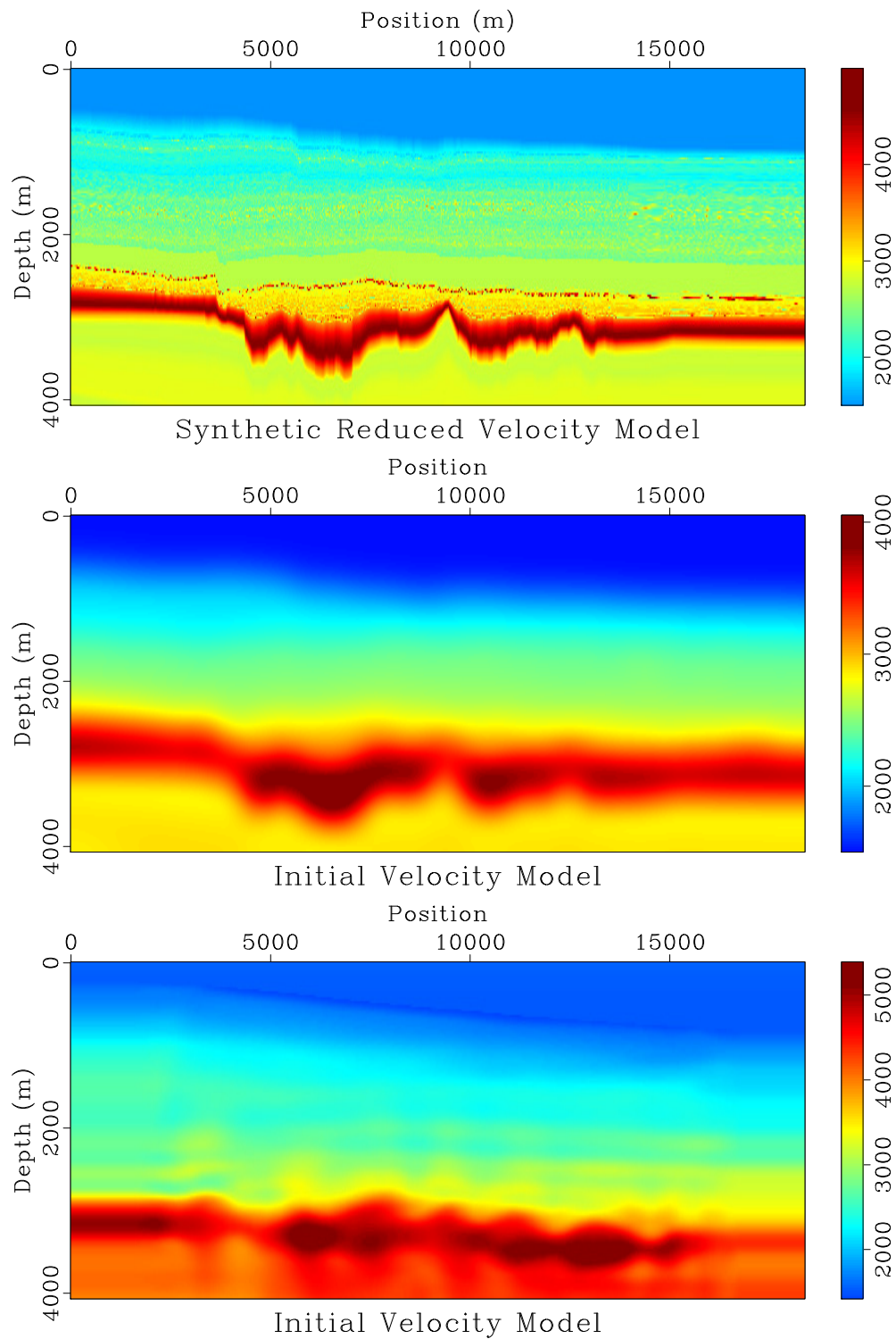
Figure 3.4: Reduced "true" velocity model (top), the initial velocity model 1 which is a smoothed version of the true velocity model (middle); and the initial velocity model 2, which is the initial velocity model provided by Petrobras and obtained by MVA (bottom).
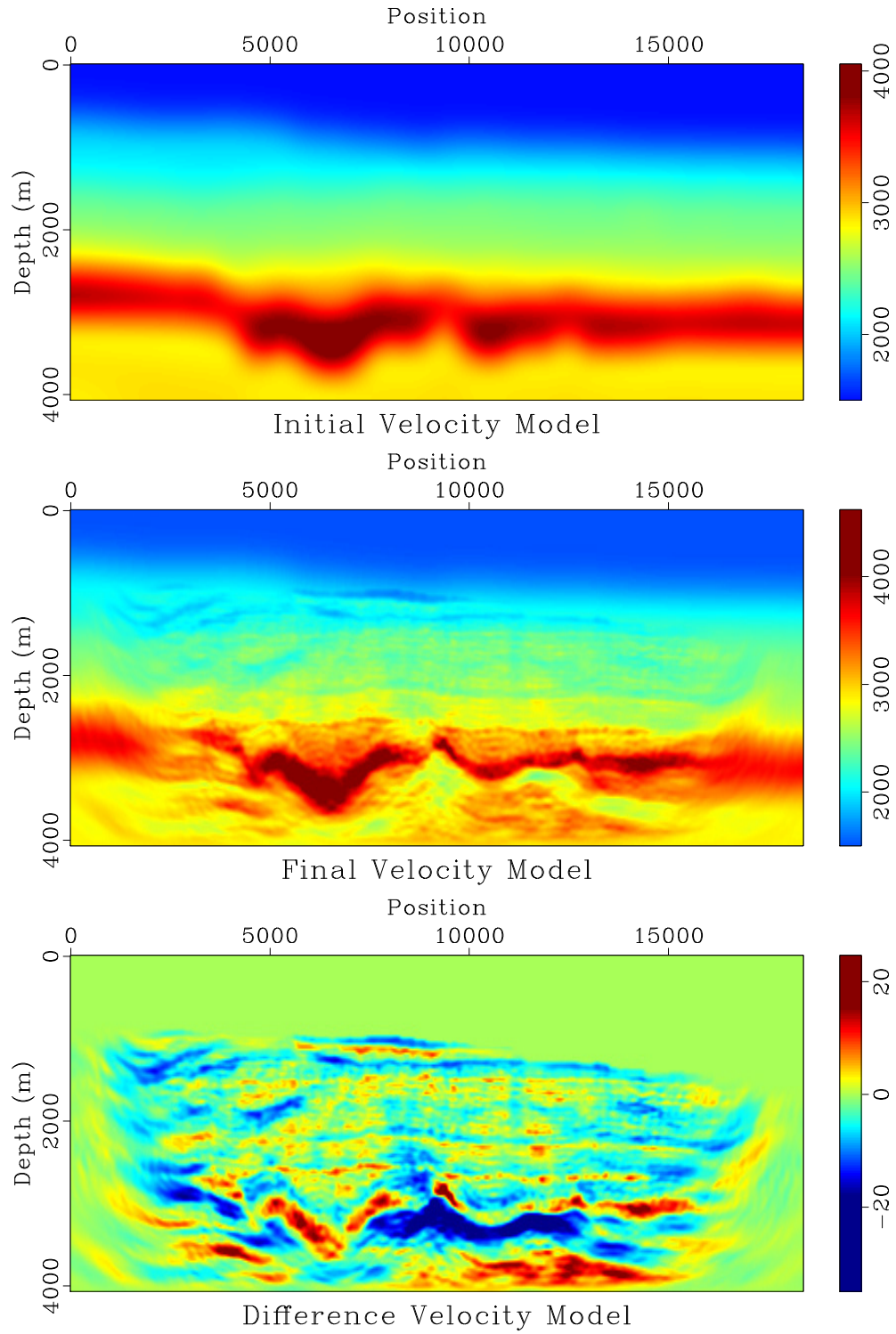
Figure 3.5: Initial velocity model, final velocity model, and the percentage difference showing the update after the waveform inversion for the synthetic line. The results were obtained following the strategy 1 (Table 3.2) and using the initial velocity model 1 (smoothed version).
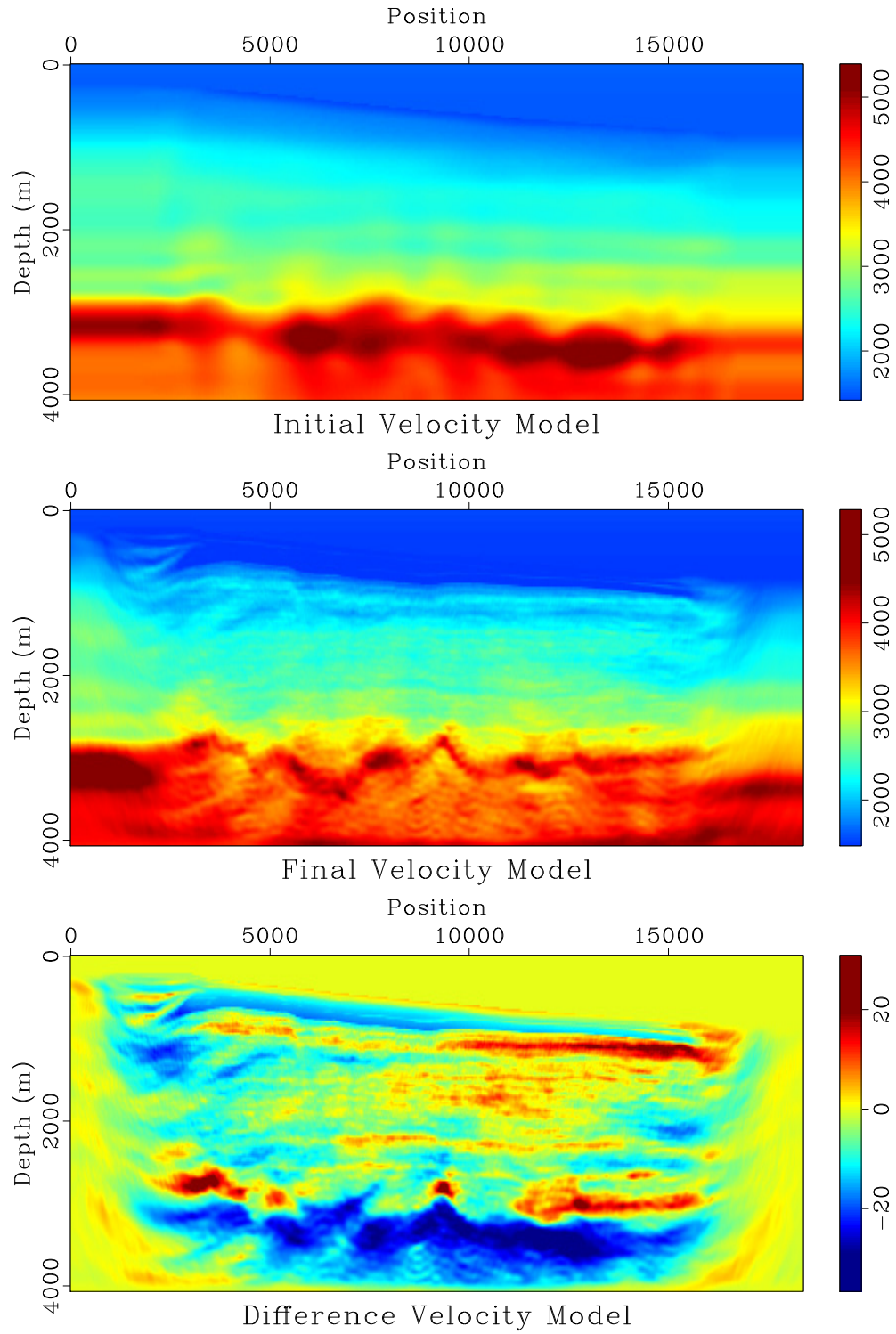
Figure 3.6: Initial velocity model, final velocity model, and the percentage difference showing the update after the waveform inversion for the synthetic line. The results were obtained following the strategy 1 (Table 3.2) and using the initial velocity model 2 (MVA version).
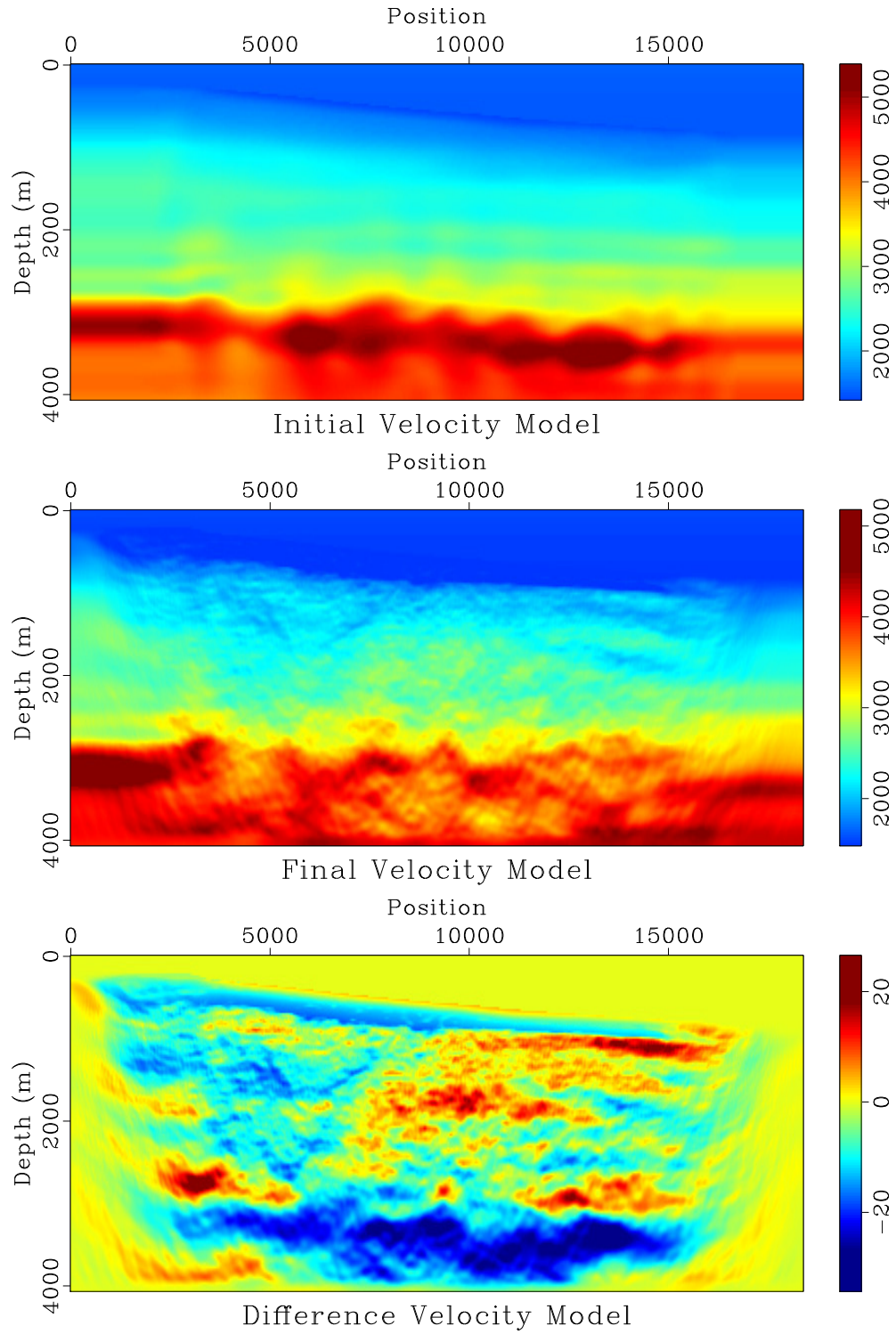
Figure 3.7: Initial velocity model, final velocity model, and the percentage difference showing the update after the waveform inversion for the synthetic line. The results were obtained following the strategy 2 (Table 3.3) and using the initial velocity model 2 (MVA version).
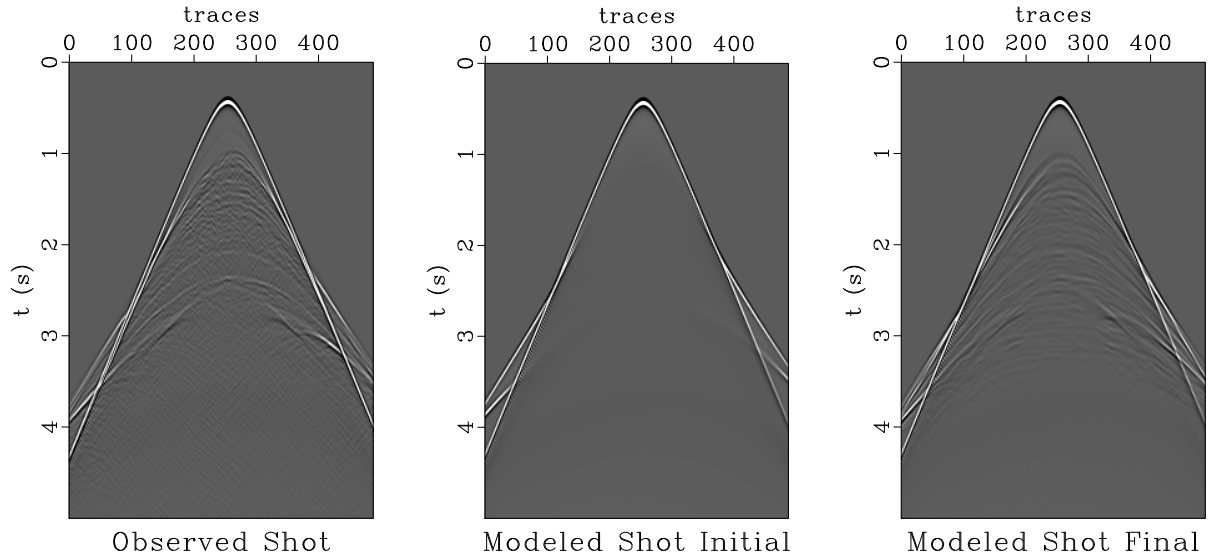
Figure 3.8: Comparison of observed shot, initial modeled shot, and final modeled shot for inversion 1.
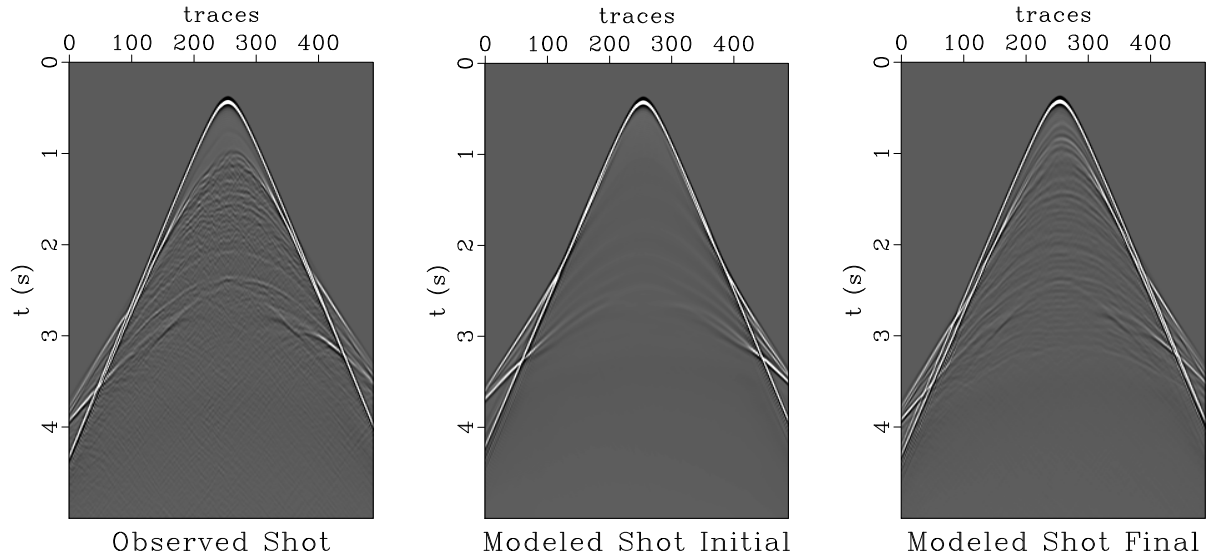
Figure 3.9: Comparison of observed shot, initial modeled shot, and final modeled shot for inversion 2.

The shot comparison also shows that inversions 1 and 2 have provided an accurate and resonably high resolution final velocity model, with the final modeled shot being similar to the observed shot. There are a significant amount of reflections, brought in by the inversion, that

can be recognized at the right time and position in both shots (Figure 3.8 and Figure 3.9).

Figure 3.10 shows the modeled shots for inversion 3. The final modeled shot shows some reflections events, although they do not seem coherent and consistent, most likely because of the "noisy" velocity model.
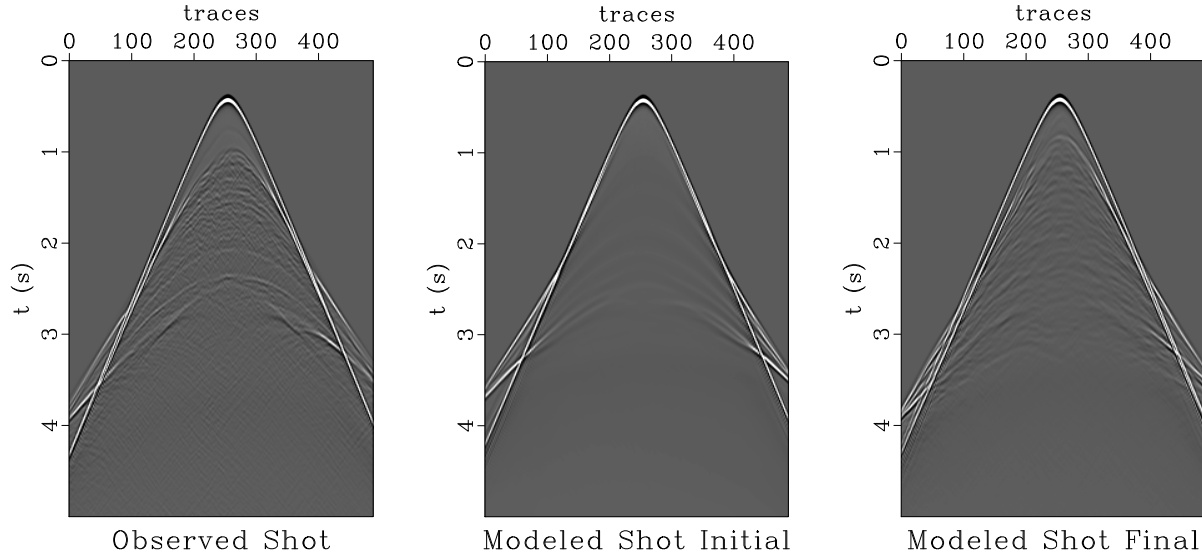
Figure 3.10: Comparison of observed shot, initial modeled shot, and final modeled shot for inversion 3.

3.4.2   Velocity Profile Comparison

In the synthetic study, the final velocity model from each inversion can be directly checked with the true velocity model. The 2D visual comparison was already previously performed. In order to verify the accuracy and the resolution of each inversion in more detail, the velocity profile at three different positions of the model was extracted and plotted together. Figure 3.11, Figure 3.12, and Figure 3.13 show the comparison of these velocity profiles for each inversion. Each plot shows the true (red), initial (blue), and final (black) velocity profiles.

Figure 3.11 shows the results for inversion 1. The resolution is clearly enhanced in the final velocity when compared with the initial velocity profile. The inversion tried to completely recover the resolution and it did a great job, however, the final inversion profile do not

70

match the true profile perfectly, the amplitude match fails most of the times, but provides a much better, and more accurate representation of the earth than the initial velocity. The complexity of the true model in terms of resolution should be considered, where the minimum layer thickness is 25m. The theoretical limit imposed by vertical incidence ($\theta=0$), maximum frequency (15Hz) and velocity (Figure 2.44) suggests that the range of the inversion resolution is approximately 50-100m, which became a challenge to recover with this parametrization.

The inversion profiles for inversion 2 follow the previous analysis (Figure 3.12). The results for inversion 1 and 2 are quite similar, except below the high velocity layer where inversion 2 could not recover the velocity. Inversion 3 results (Figure 3.13), as previously noticed, did not bring the same expected high resolution and the wavenumber content is similar to the initial velocity model. Figure 3.14 shows the comparison between the inversion results and it confirms that inversions 1 and 2 provide similar results and inversion 3 was not satisfactory.

3.4.3   Wavenumber Analysis

Following the same type of analysis developed in Chapter 2, Figure 3.15 shows the wavenumber amplitude spectrum of the true, the initial, and the final velocity model (left). The amplitude of the higher wavenumbers introduced by the waveform inversion are low and hidden below the dominant low wavenumber content, but the wavenumber amplitude spectrum of the velocity difference (final - initial) (Figure 3.15 (right)) reveals the range of the wavenumber that has been updated, reaching at least $k = 0.01(1/m)$.

3.5   Analysis and Conclusions

The final results for inversions 1 and 2 have shown improvement in the resolution of the final velocity model. Resolution is improved throughout the entire model (especially at shallow depths) and reached the depth of the reservoir, our main target. The results were checked by directly comparing the initial, final, and true velocity models, which have shown that waveform inversion can recover thin layers and main events, for example, the precise

definition of the high velocity layer at 3.0 km. Velocity profiles confirmed the improvement in the resolution, however, the true and final velocity profiles do not match perfectly, probably due to the complexity of the true velocity model. The amplitude match of the observed and modeled data fails completely. Shot comparison showed the similarity between the observed data and the final modeled data, where reflections are recognized and closely resemble the true shot.

Figure 3.11: Velocity profile comparison for three positions of inversion 1: a) 7750m (left); b)9735m (middle); c)11500m (right).

Figure 3.12: Velocity profile comparison for three positions of inversion 2: a) 7750m (left); b)9735m (middle); c)11500m (right).
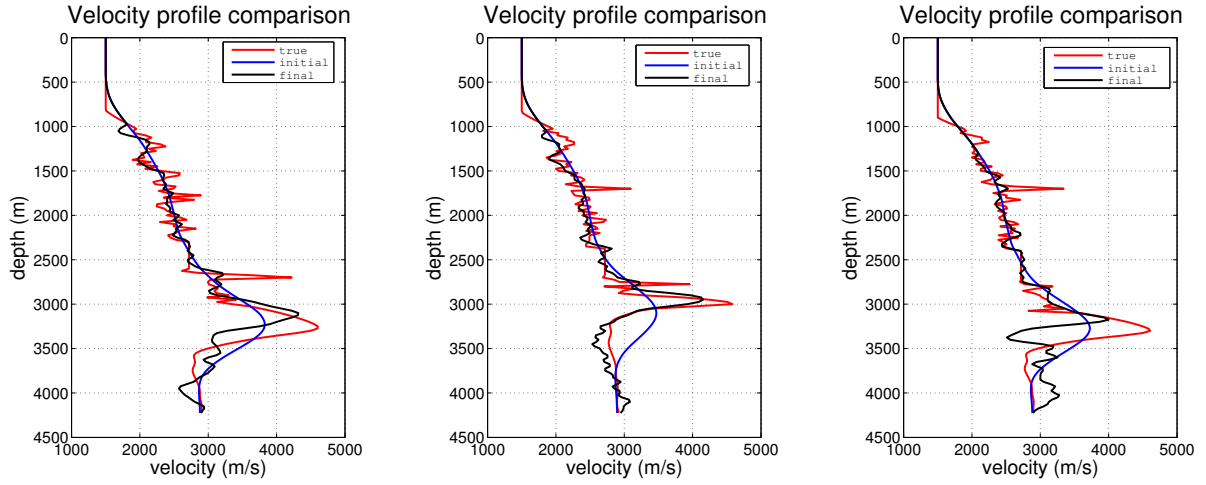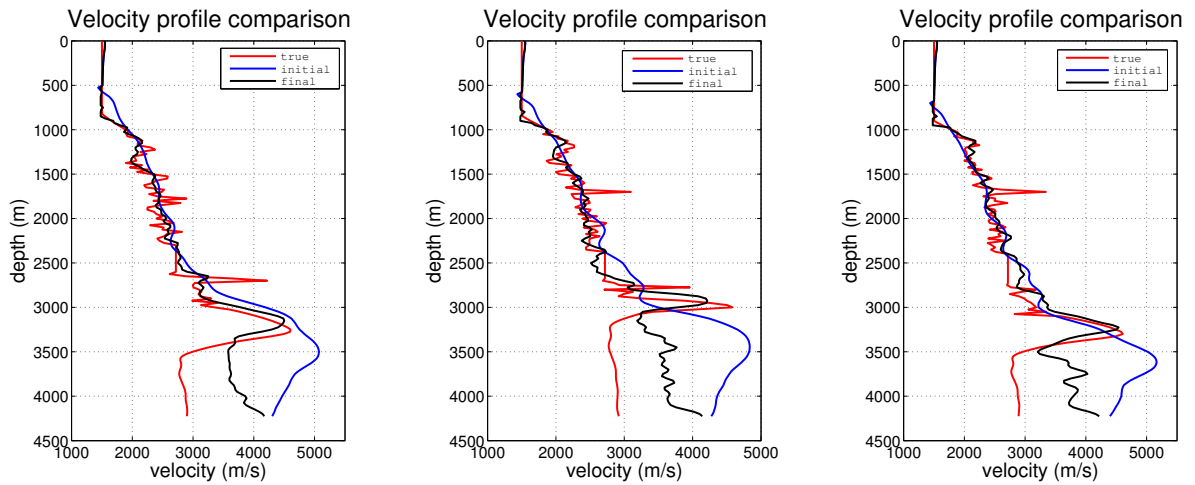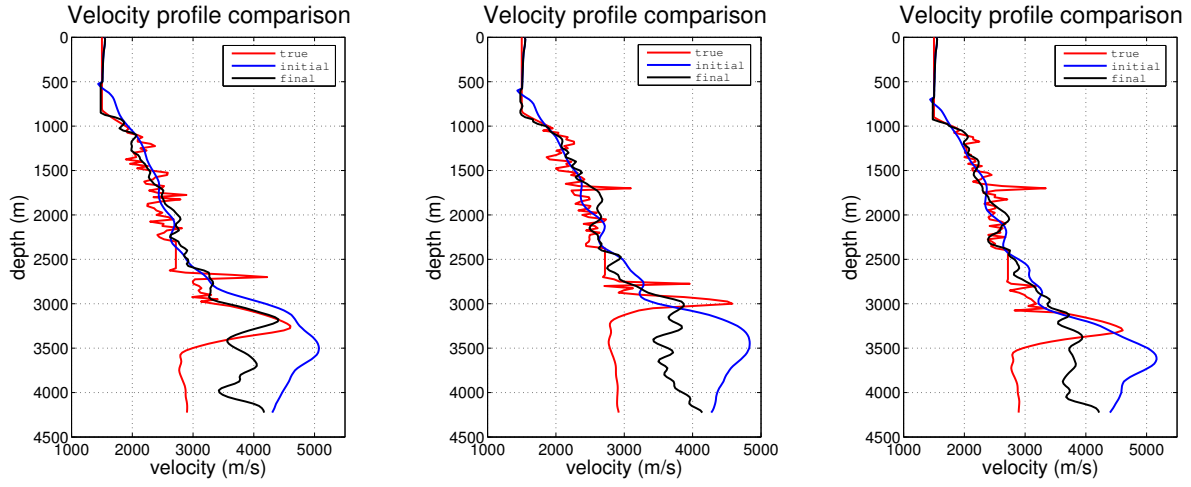
Figure 3.13: Velocity profile comparison for three positions of inversion 3: a) 7750m (left); b)9735m (middle); c)11500m (right).
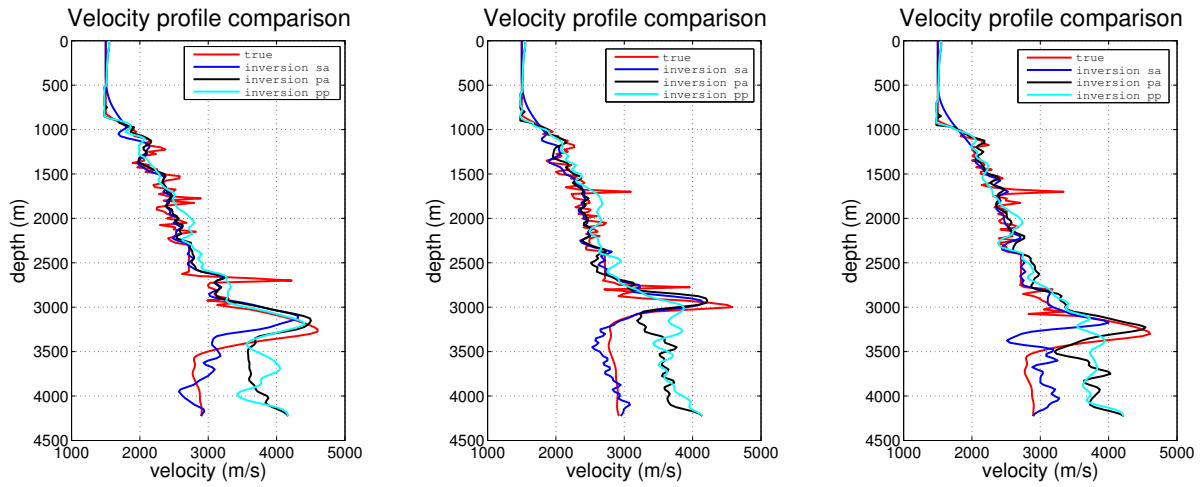
Figure 3.14: Velocity profile comparison between the three inversions for three positions: a) 7750m (left); b)9735m (middle); c)11500m (right).

73
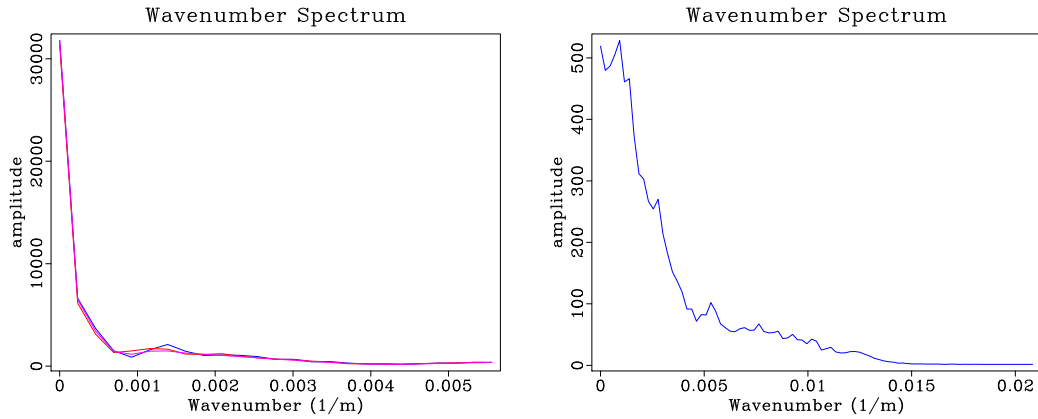
Figure 3.15: Wavenumber amplitude spectrum of the true, the initial, and the final velocity model for inversion 1; only for velocity difference (final - initial) (right).

Results from inversion 1 and 2 showed that the different initial velocity models did not have a large impact on the final results. Both results are quite similar as verified by velocity profile comparison and the initial velocity models are probably accurate enough to start the inversions. However, the impact of the different inversion strategies is significant. Results for inversion 3 have shown that the inversion strategy of using the objective function based on phase residuals only was not as effective in bringing high resolution to the velocity model as the strategy that included in the later inversions an objective function that used both amplitude and phase residuals. This fact can explain the limited resolution results for the field data inversion. The objective function that includes amplitude data is more robust and the diving waves update prevailed over the reflections in the inversion process. In the phase only objective function both information are balanced and the inversion might be trapped in a local minimum.

The final results could have been improved in resolution by performing further inversions in two different ways: a) inverting without time damping the data; b) inverting for frequencies higher than 15 Hz.

Expanding the minimum offset is important to help better measure the diving waves that travel through at the deeper part of the model allowing to recover small wavenumbers which

depends on the minimum frequency of the data. However, the resolution is enhanced by the inclusion of the reflections in the inversion combined with the amplitude/phase residual objective function approach.

The importance of acquiring seismic data with larger maximum offset for the waveform inversion success is already proven. The results presented here did not provide an optimum minimum offset for a new survey in the Campos Basin area, but the synthetic evaluation shows that it is theoretically possible to obtain high resolution velocity model using a cable length of 12.1 km. The report "An Overview of Marine Seismic Operations" (Report448, 2011) states that a typical ocean bottom cable length is on the order of 5-6km, which precludes a new OBC survey with a larger cable length.

CHAPTER 4

CONCLUSIONS

The main goal of this thesis is to improve the reservoir characterization of the Campos Basin field. The choice to work with waveform tomography is based on the robustness of the technique in generating high resolution model parameters. The 2D acoustic isotropic assumption was made to use the available software provided by Prof. Gerhard Pratt, which performs waveform tomography in the frequency domain. In addition, any 3D approach would need more computational effort and time to perform the inversion.

In the first part of my study, waveform inversion was applied to the OBC Campos Basin field. The goal was to bring accuracy and enhance resolution of the final P-wave velocity model. The final results have shown improvements mostly in updating the background velocity model, which produced migrated images with more continuous and focused horizons at the depth of interest (reservoir depth). The accuracy is also checked by common image gathers (CIGs) with deep events being more flat.

Although resolution was enhanced especially in the shallow part of the model, waveform inversion was not successful at bringing higher resolution to the final velocity model. Wavenumber content analysis showed that the initial and final velocity model wavenumber content is almost the same. One of the thesis goals is to produce an enhanced seismic image because it can lead to a new geological interpretation of the reservoir, thereby improving the reservoir characterization. Also, the updated velocity model may be used in acoustic/elastic attributes inversion where it is crucial to incorporate a more reliable velocity information which will better constrain the results.

The limited resolution in the final results seems to be related to the parametrization and the strategy used in the inversion. In order to improve the results, we could have used time damping relaxing approach which slowly incorporates more data into the inversions,

i.e. reflections. In addition, we should have included in the later inversions a more robust objective function which combines the amplitude and phase residuals. This type of approach usually works well on synthetic data but requires an amplitude match procedure between observed and modeled data when applied to field data.

In the second part of my study waveform inversion was performed on a synthetic data set generated using a reliable "true" velocity model of Campos Basin field and on a new 2D OBC geometry survey with a larger number of sources and receivers. Larger cable length provides a larger maximum offset that helps record the diving waves which have traveled through the deeper part of the model. The final results have shown that the resolution is improved throughout the entire model and reached the depth of the reservoir. Resolution enhancement is brought by the combination of larger offsets, that properly measured the diving waves, the inclusion of the reflections in the inversion, and using the amplitude/phase residuals objective function approach. The results show that waveform inversion could recover thin layers and accurately define the high velocity layer at 3.0 km depth. Velocity profiles confirmed the improvement in the resolution, however, the true and final velocity profiles do not match perfectly and the amplitude match fails completely, likely due to the complexity of the true velocity model in terms of resolution, much higher than the maximum inverted frequency (15 Hz) can recover. The final results might be improved by applying further inversions, for example, inverting for data without damping that includes all information, and also for frequencies higher than 15 Hz. Higher frequencies can provide higher resolution in the velocity model, but there is a limit imposed by the scattering wavenumber equation (Equation 2.3) that has to be checked before performing the inversion.

My synthetic data were generated using a 12 km cable length. However, the available cable typically is a 5-6 km long (Report448, 2011), which precludes a new OBC survey with a larger cable length.

4.1 Future Work

In order to improve the resolution of the field data result, I first recommend for future work the following changes in the waveform inversion strategy. The recommnedations are based on the tests, results, and analysis of the application of waveform tomography to the Campos Basin field data and later to the synthetic data.

- first break picking time

- time domain damping relaxing (1s, 2s, 4s, and no damping)

- amplitude/phase objective function

The data included in the inversion will be better controlled by combining the first break picking time, as shown in Figure 2.14, and the time damping relaxing approach. Both will help the inversion to slowly include data in the inversion, focusing the first few inversions more properly on the diving waves to establish the low wavenumbers in the velocity model and later including the reflections to increase resolution. In addition, the application of a combined amplitude/phase objective function showed to be robust for the synthetic data, although some amplitude match procedure needs to be applied between observed and modeled data.

A more advanced approach would include VTI symmetry in the inversion, for example, using a 2D acoustic anisotropic wave equation. The initial model parameters (vertical velocity V_{P0}, δ, and ϵ) would be provided by velocity analysis carried out by Petrobras.

REFERENCES CITED

Alkhalifah, T. A. (2014), *Full Waveform Inversion in an Anisotropic World - Where are the parameters hiding?*, EAGE Publications.

Aster, R. C., B. Borchers, and C. H. Thurder (2013), *Parameter Estimation and Inverse Problems*, Academic Press.

Bednar, J. B., C. Shin, and S. Pyun (2007), Comparison of waveform inversion, part 2: phase approach, *Geophysical Prospecting, 55*, 465–475.

Grion, S., R. Exley, M. Manin, X.-G. Miao, A. Pica, Y. Wang, P.-Y. Granger, and S. Ronen (2007), Mirror imaging of obs data, *First Break, 25*, 37–42.

Lailly, P. (1983), The seismic inverse problem as a sequence of before stack migrations, in *Conference on Inverse Scattering, Theory and Application, Society for Industrial and Applied Mathematics, Expanded Abstracts, 206220.*

Martins, L. M. R. (2013), From obc seismic to porosity volume: A pre-stack analysis of a turbidite reservoir, deepwater campos basin, brazil, Master's thesis, Colorado School of Mines.

Pratt, R. G. (1999), Seismic waveform inversion in the frequency domain, part 1: Theory and verification in a physical scale model, *Geophysics, 64*, 888–901.

Pratt, R. G. (2013), Waveform tomography - an introduction to theory and practice, 2013.

Pratt, R. G., and M. H. Worthington (1990), Inverse theory applied to multi-source cross-hole tomography, part 1: Acoustic wave-equation method, *Geophysical P, 38*, 287–310.

Pyun, S., C. Shin, and J. B. Bednar (2007), Comparison of waveform inversion, part 3: amplitude approach, *Geophysical Prospecting, 55*, 477–485.

Ratcliffe, A., C. Win, V. Vinje, G. Conroy, M. Warner, A. Umpleby, I. Stekl, T. Nangoo, and A. Bertrand (2011), Full waveform inversion: a north sea obc case study, in *SEG San Antonio 2011 Annual Meeting.*

Report448 (2011), An overview of marine seismic operations, *Tech. rep.*, International Association of Geophysical Contractors.

Ribeiro, N. (2011), Joint inversion of multicomponent seismic data for reservoir characterization of an offshore campos basin field, brazil, Master's thesis, Colorado School of Mines.

Shin, C., S. Pyun, and J. B. Bednar (2007), Comparison of waveform inversion, part 1: conventional wavefield vs logarithmic wavefield, *Geophysical Prospecting*, *55*, 449–464.

Sirgue, L. (2003), Waveform inversion in the frequency domain for large offset seismic data, Ph.D. thesis, lUniversit Paris XI.

Sirgue, L., and R. G. Pratt (2004), Efficient waveform inversion and imaging: A strategy for selecting temporal frequencies, *Geophysics*, *69*, 231–248.

Tarantola, A. (1984), Inversion of seismic reflection data in the acoustic approximation, *GEOPHYSICS*, *49*, 1259–1266.

Tarantola, A. (2005), *Inverse Problem Theory and Methods for Model Parameter Estimation*, Society for Industrial and Applied Mathematics.

Virieux, J., and S. Operto (2009), An overview of full-waveform inversion in exploration geophysics, *Geophysics*, *74*, WCC1–WCC26.

Woodward, M. J. (1992), Wave-equation tomography, *GEOPHYSICS*, *57*, 15–26.